

DESIGN AND EVALUATION OF A GUI FOR SIGNAL AND DATA ANALYSIS OF
MOBILE FUNCTIONAL NEAR-INFRARED SPECTROSCOPY SYSTEMS

A Thesis by

Mousa Moradi

Master of Science, Shahid Beheshti University, Tehran, Iran, 2014

Bachelor of Science, Kermanshah Institute of Technology, Kermanshah, Iran, 2012

Submitted to the Department of Biomedical Engineering
and the faculty of the Graduate School of
Wichita State University
in partial fulfillment of
the requirements for the degree of
Master of Science

July 2020

© Copyright 2020 by Mousa Moradi

All Rights Reserved

DESIGN AND EVALUATION OF A GUI FOR SIGNAL AND DATA ANALYSIS OF
MOBILE FUNCTIONAL NEAR-INFRARED SPECTROSCOPY SYSTEMS

The following faculty members have examined the final copy of this thesis for form and content, and recommend that it be accepted in partial fulfillment of the requirements for the degree of Master of Science with a major in Biomedical Engineering.

Jaydip Desai, Committee Chair

Kim Cluff, Committee Member

Ajita Rattani, Committee Member

ACKNOWLEDGEMENTS

I would like to thank my supervisor Dr. Jaydip Desai, for his guidance, motivation and providing me with this exciting project and for his help with its development and continuation. I enjoyed working on the project and it has been a meaningful part of my time at WSU.

I would like to thank Dr. Mary Lee Esty, Brain Wellness and Biofeedback Center at Maryland, who introduced me to the field of neurofeedback therapy.

I would like to thank the members of Neuro-Robotics Lab for providing me with a fun work environment and for their help and participation in experiments.

I would like to thank Mr. Nathan Smith, Project Innovation Hub Manager. John Bardo Center, for his technical advices for PCB productions.

Finally, I would like to thank my parents for their love and encouragement, without whom I would never have enjoyed so many opportunities.

ABSTRACT

Functional near-infrared spectroscopy (fNIRS) is an emerging neuro-imaging modality that can indicate cortical functionality with good temporal resolution (0.5-1 sec). Unlike fMRI, up to now, there is no standard method and a whole package that can perform signal processing and data analysis for fNIRS dataset. This thesis is focused on developing a Graphical User Interface (GUI) model in MATLAB that can perform both signal and data analysis for data collected by mobile fNIRS devices either in offline or online mode. It can remove motion artifacts using detrending methods and performs Band Pass Filtering using the low-and high-pass cutoff frequencies of 0.6 and 0.01 Hz, respectively and check the quality of signal in term of Signal to Noise Ratio (SNR). The filtered fNIRS signals were then sent to a General Linear Model (GLM) to estimate the linear model parameters. T-statistical values have been calculated and unrelated values have been further removed prior to obtaining results in terms of evoked related potentials, 2D and 3D head projections. In this thesis, signal processing and data analysis have assessed in the proposed GUI through the data of four participants [three males, age of 22, 24, 28 and, one female, age of 19] collected from two different fNIRS systems. Results for both systems verified when signal is de-trended using Discrete Cosine Transform (DCT) and it is filtered using a BPF order 4, cutoff frequencies of 0.01 to 0.6 Hz) the SNR value of 6.99 dB from ARTINIS system was achieved. Brain mapping results are shown with both hand motor imagery, the subjects consumed more hemoglobin in their both hemispheres. To localize each optode position, more accurately and complicated methods like 3D digitizer can be replaced with 10-20 standard system. With advantages such as hazard-free application, motion artifact robustness and the possibility to miniaturize hardware, fNIRS may enable new applications in the BCI context, in clinical tools and diagnosis and further contribute to new insights in brain research and neuroscience.

TABLE OF CONTENTS

Chapter	Page
1. INTRODUCTION.....	1
1.1 Motivation and Objective	1
1.2 Novelty of the Current Project	3
2. LITERATURE REVIEW	4
2.1 Overview of Signal Processing and Data Analysis	4
2.2 Available fNIRS Toolbox and Software	9
2.3 fNIRS Instrumentation and Signal	15
2.4 Experiments and Paradigms	18
2.4.1 Test Design Strategies	21
2.5 Noise Removal	25
2.5.1 Instrumental Noise	26
2.5.2 Motion Artifact	27
2.5.3 Physiological Noise	30
3. MATERIAL AND METHODS	33
3.1 System Requirement	33
3.2 GUI Structure	34
3.3 Data Acquisition	35
3.4 Data Conversion	37
3.5 Signal Processing.....	38
3.5.1 Detrending	38
3.5.1.1 Linear Detrend	39
3.5.1.2 DCT Detrend	39
3.5.1.3 DWT Detrend	40
3.5.2 Filtering	42
3.5.2.1 BPF	42
3.5.2.2 Moving Average	43
3.5.2.3 Savitzky-Golay	44
3.5.3 Signal Quality	45
3.6 Data Analysis	45
3.6.1 Experiment Procedure and Paradigm	45
3.6.2 General Linear Model	46
3.6.3 Statistical Test	48
3.7 MATLAB SIMULINK	49

TABLE OF CONTENTS (continued)

Chapter	Page
4. RESULTS	52
4.1 Signal Processing and Detrending.....	52
4.1.1 Time-Domain	52
4.1.2 Frequency-Domain	56
4.2 Data Analysis and Estimation	59
4.3 Evoked Related Potential	69
4.4 Brain Mapping Results	73
5. DISCUSSION AND FUTURE WORK	78
6. CONCLUSION	80
REFERENCES	81
APPENDIX.....	89

LIST OF TABLES

Table	Page
1. fNIRS Toolboxes and App Developments in the Literature	14
2. Main Specifications and Parameters Measured by Different Types of fNIRS Systems	17
3. Important Factors in Deciding the Number of Channels	23
4. Wavelet-Based Functions in MATLAB	40
5. Results of Detrending and Signal Processing for All Subjects in This Study	55
6. ANOVA Test Results for All Subjects	61
7. Statistical Results of 8 Channels for Subjects # 1 &2	66
8. Statistical Results of 8 Channels for Subjects # 3 &4	67

LIST OF FIGURES

Figure	Page
1. Spatiotemporal resolution of common neuroimaging devices	2
2. HR signal in a typical fNIRS system	2
3. A scattering medium with an incident and transmitted light ray	5
4. Schematics describing the NIRS-SPM framework in Ye’s work	8
5. NIRS-SPM GUI developed by Bio Imaging Signal Processing (BISP) lab at KAIST in Korea	11
6. nirsLAB main window for signal processing and visualizing	12
7. NIRSTORM window fNIRS data analysis fNIRS data analysis	13
8. Principle of fNIRS signal acquisition	17
9. Optical window of NIR light for different tissue’s part	17
10. Typical fNIRS signals	18
11. A trial for the Finger tapping experiment in Kuboyama’s study	19
12. Finger tapping and hand grasping experiment	20
13. Example of congruent and incongruent conditions used in Yanagisaw’s study	21
14. Mounting on the 10/20 electrode positioning system	21
15. Boxcar function for a typical task	22
16. Modified general block design for fNIRS based on fMRI methodology	22
17. fNIRS probe setup used in each experiment	23
18. Using fMRI to find optode locations	24
19. Optode locations using 3D digitizer	24

LIST OF FIGURES (continued)

Figure	Page
20. Commonly used open source toolboxes for channel registration	25
21. Spikes and baseline shift	27
22. Performance of wavelet transform on removing motion artifact	29
23. Typical Noises and artifacts in fNIRS signal	30
24. Performance of S-G filter on fNIRS signal	31
25. The flowchart for the proposed GUI	34
26. The steps used for signal processing and data analysis in the proposed GUI	35
27. Optode configuration based on 10/20 system	36
28. SIMULINK model by g.Nautilus for hybrid data acquisition from fNIRS and EEG	36
29. Data conversion interface	37
30. Block diagram for LD detrending method	39
31. Detrending methods on the typical fNIRS data	41
32. BPF characteristic	43
33. Moving average filter design	44
34. Default parameters for S-G filtering based on the literature in the designed GUI	44
35. Experiment procedure and paradigm	46
36. Reconstructing G matrix in GLM model for hemodynamic response	47
37. Applying GLM model on a typical data	48
38. Online mode processing in the proposed GUI	50
39. SIMULINK model for the signal processing and data analysis based on the experiment design in this thesis	50

LIST OF FIGURES (continued)

Figure	Page
40. Linear detrending results for subject #1.....	53
41. DCT detrending results for subject #1	54
42. FFT results for subject #1	56
43. FFT results for subject #2	57
44. FFT results for subject #3	58
45. FFT results for subject #4	58
46. Filter design response	59
47. Data Analysis and Estimation of subject #1	60
48. Calculated values after GLM estimation on data collected from subject #1	65
49. Histogram of p-values for all subjects	69
50. ERP responses of each channel for subject #1	70
51. ERP responses of each channel for subject #2	71
52. ERP responses of each channel for subject #3	72
53. ERP responses of each channel for subject #4	72
54. 2D brain mapping results per channel for subject #1	73
55. 2D brain mapping results per channel for subject #2	74
56. 2D brain mapping results per channel for subject #3	75
57. 2D brain mapping results per channel for subject #4	75
58. 3D brain mapping for Subject #1 and Subject #2	76
59. 3D brain mapping for Subject #3 and Subject #4	77

LIST OF ABBREVIATIONS

fNIRS	Functional Near-Infrared Spectroscopy
CBF	Cerebral Blood Flow
FNIRI	Functional Near-Infrared Imaging
PET	Positron Emission Tomography
FMRI	Functional Magnetic Resonance Imaging
EEG	Electroencephalography
BCI	Brain Computer Interface
HR	Hemodynamic Response
HbO	Oxy-Hemoglobin
HbR	Deoxy-Hemoglobin
THb	Total Hemoglobin
GUI	Graphical User Interface
DCT	Discrete Cosine Transform
DWT	Discrete Wavelet Transform
SPM	Statistical Parametric Mapping
MBLL	Modified Beer-Lambert Law
SNR	Signal to Noise Ratio
DPF	Differential Pathlength Factor
RLS	Recursive Least Square
GLM	General Linear Model
RTMS	Repetitive Transcranial Magnetic Stimulation
HOMER	Hemodynamic Optic Metabolic Evoked Response

LIST OF ABBREVIATIONS (continued)

BISP	Bio Imaging Signal Processing
FOLD	fNIRS Optodes Location Decider
MDL	Minimum Description Length
ICNNA	Imperial College Near-Infrared Spectroscopy Neuroimaging Analysis
CW	Continuous Wave
FD	Frequency Domain
TR	Time Resolve
CMRO2	Local Cerebral Metabolic Rate of Oxygenation
RCBF	Regional Cerebral Blood Flow
CBV	Cerebral Blood Volume
STD	Standard Deviation
ME	Maximum Effort
HRF	Hemodynamic Response Function
ROI	Region of Interest
PMT	Photo-Multiplier Tube
PCA	Principle Component Analysis
FFT	Fast Fourier Transform
CBSI	Correlation-Based Signal Improvement
S-G	Savitzky-Golay
BPF	Band-Pass Filter
OD	Optical Density
CAR	Common Average Reference

LIST OF SYMBOLS

λ	Wavelength
μ	Absorption Coefficient
L	Distance
B	Geometrical Parameter
A	Age
ε	Extinction Coefficient
$\bar{\mu}^2$	Mean Square Voltage Variance
K_B	Boltzmann's Constant
T	Temperature
R	Resistor
Δf	Spectral Bandwidth
δ_{kl}	Kronecker Delta
dB	Decibel
β	Regression Coefficient
ϵ	Error
Γ	Gamma Function

CHAPTER 1

INTRODUCTION

1.1 Motivation and Objective

Functional near-infrared spectroscopy (fNIRS) was first introduced in 1977 by Jöbsis [1] as an optical imaging technique that can measure the cerebral blood flow (CBF) in a non-invasive and continuous-based system using near-infrared (NIR) light. Neurovascular coupling tends to find changes in neural activity in conjunction to CBF [2]. This coupling of brain cell function to the vascular system is the basis for several functional neuroimaging systems relevant to human studies [2]. From the 2000s until today, the next major step was optimizing and developing algorithms for brain activity mapping from topographic information which known as functional near-infrared imaging (FNIRI). There are three important parameters to choose a proper neuroimaging modality for brain studies: 1) Temporal resolution (how fast data acquisition system is), 2) Spatial resolution (how well the system can distinguish nearby cells/pixels) and Mobility (the ability of system to be freely moving). Among brain imaging modalities, positron emission tomography (PET) and functional magnetic resonance imaging (fMRI) known to have a perfect spatial resolution (~5 mm) and they still have been considering as a gold standard for brain investigations [3, 4, 5]. Despite of having a good spatial resolution, fMRI and PET systems suffer from huge size and non-portability. Also, they do not seem to collect data from the brain as fast as other similar modalities used for brain imaging (temporal resolution (~ 30 sec) [5]). Figure 1 shows a comparison among the mostly used brain imaging techniques by researchers. As shown in Figure 1, among all neuroimaging systems, only electroencephalography (EEG) and fNIRS can be used as a long-term monitoring and brain computer interface (BCI) applications because these devices are portable, light weight, and easily configured for human subject testing [5]. In optical brain imaging and

neuroimaging studies, fNIRS technique can be used to enhance human understanding of brain functions, by generating images of the structure and function of the nervous system, the method is extensively used to support diagnostic, monitoring and treatment of brain [6, 7]. fNIRS recordings are hemodynamic signals that come from the latent neural sources that are spatially and temporally mixed across the brain [9]. The hemodynamic response (HR) for a typical fNIRS system has shown in Figure 2. HR signal is discriminated to oxy-hemoglobin (HbO), deoxy-hemoglobin (HbR) and total hemoglobin (tHb).

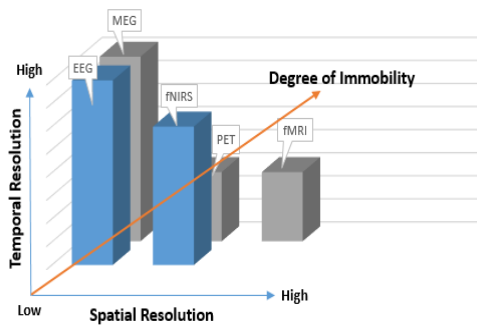


Figure 1. Spatiotemporal resolution of common neuroimaging devices.

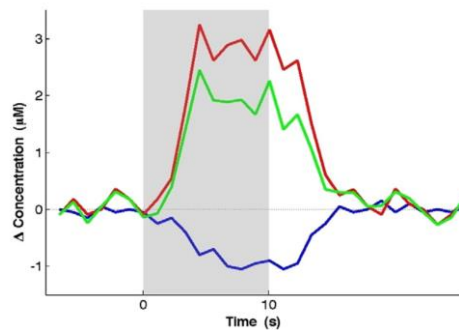


Figure 2. HR signal in a typical fNIRS system. Oxy-hemoglobin (Red), deoxy-hemoglobin (Green) and total hemoglobin (Blue) [9].

In comparison with fMRI, currently, no standardized and widely accepted signal processing method for fNIRS exists and no fNIRS guidelines articles have been published yet [10]. This thesis aimed to develop a graphical user interface (GUI) to show how different signal processing and data analysis approaches (including and excluding approaches that partially correct for the possible signal contamination) affect the results of a typical functional neuroimaging study performed with fNIRS. Besides this, the proposed GUI can check SNR as a quality control of fNIRS data and to decide whether to calibrate optodes on the scalp to get a better signal.

1.2 Novelty of the Current Project

Based on the literature on signal processing and data analysis which has been reviewed in this thesis, the purpose of this project was to design and develop a MATLAB-based toolbox which is open source and comprehensive package by taking advantages of available open source app (Discussed in section 2.2) and utilize new methods for noise cancelation, artifact removal and 2D mapping. Some of novelties provided by the proposed GUI:

1. To the best of our knowledge, there is no toolbox or software to show SNR of fNIRS signal as a quality control measurement in both offline and online mode.
2. Although there are many works that used Discrete Cosine Transform (DCT) for motion artifact removal in EEG studies, at the time of this thesis, there is no toolbox/app that applied DCT on fNIRS signal.
3. The proposed GUI not only provides DCT for noise and artifact removal but also gives the option to use other methods discussed in section 2.5 to remove physiological noises as well.
4. Despite of other available toolbox/app (section 2.2) which takes lots of time to compute estimated signals and project them on the head shape (Due to head complexity and too many meshes), the proposed GUI takes less computational time to show 2D and 3D mapping of the brain.

CHAPTER 2

LITERATURE REVIEW

2.1 Overview of Signal Processing and Data Analysis

Research in the field of fNIRS has been performed for more than 20 years. Nevertheless, consensus on signal processing and data analysis methods is still lacking [10]. The main issue related to previously published papers on fNIRS signal and data analysis was that they have been unable to show the possible combination of HR changes associated to neurovascular coupling (i.e., scalp blood flow and systemic blood flow). This might be occurred since these researchers used to perform the signal processing and data analysis methods and to apply those pre-defined measurements provided by companies without a deep understanding of the utilized steps. In 2008, Ye et al. [11] introduced the first statistical parametric mapping (SPM) toolbox in order to quantify fNIRS data in terms of HbO, HbR and tHb. Ye reported that SPM in addition to provide a good resolution, it makes calculation of activation maps for measuring oxy, deoxy, and total hemoglobin possible. Figure 4 has shown the methodology for Ye's SPM toolbox. A. Farras et al. in 2009 [12] used adaptive GLM model along with a multi-channel NIRS system to obtain a real time imaging of human brain. One of the main drawbacks of. Farras's work was wrong assumption in designing Kalman filter which it resulted in data overfitting. In 2010, Hu et al. [13] optimized Kalman filter and GLM model to develop a new NIRS analyzing algorithm. In each step, GLM coefficients were updated by Kalman outputs and finally these coefficients were used to perform t-statistical test. Hu's work has indicated the proposed method can positively eschew the noise fluctuations in the experiment design and it is able to track task-related potentials. A schematic of Hue's method is summarized below. 1) Modified beer lambert law (MBLL) is utilized (Equations 1-7) to calculate either/both HbO or/and HbR [14, 15, and 16], 2) Designing a linear model for experiment design

step which fits concentration changes. This steps can control the signal level versus noise and improve Signal to Noise Ratio (SNR) value.3) Estimating of the linear model's parameters using Kalman filter 4) T-statistical test is performed on a selected time frame to decide if the data is corresponded as brain signal or not.

$$I_{in}(\lambda) = I_o(\lambda)e^{-\Delta\mu_a(\lambda)*L*DPF} + G(\lambda) \quad (1)$$

Or

$$OD = \ln \frac{I_{in}(\lambda)}{I_o(\lambda)} \quad (2)$$

Or

$$OD = \Delta\mu_a(\lambda).L.DPF(\lambda) + G(\lambda) \quad (3)$$

Where $I_{in}(\lambda)$ and $I_o(\lambda)$ are the incident and the detected light intensity, respectively, μ_a is the absorption coefficient, L the distance (cm) between light entry and light exit point, $G(\lambda)$ is the geometrical parameter for the light's scattering properties and the DPF is Differential pathlength factor that is contingent upon the age of subject and the anatomy of the skull and it shows how far the infrared light can go through brain tissues. Figure 3 shows the MBLL's parameters in a medium. Equation 4 shows the DPF as a function of age A and wavelength λ [4].

$$DPF(A, \lambda) = 223.3 + 0.05624A^{0.8493} - 5.723 \times 10^{-7} \lambda^3 + 0.001245 \lambda^2 - 0.9025 \lambda \quad (4)$$

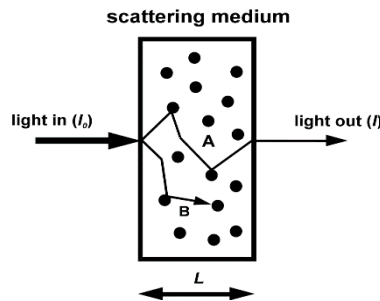


Figure 3. A scattering medium with an incident and transmitted light ray. The chromophore is symbolized by black dots. Light ray A is scattered, and therefore travels a distance which equals the pathlength correction factor times the physical pathlength L. Light ray B is absorbed completely after being scattered.

Equations 1-4 can be modified as below:

$$\Delta C = \begin{pmatrix} \Delta C_{HbO} \\ \Delta C_{HbR} \end{pmatrix} = \begin{pmatrix} \varepsilon_{\lambda 1, HbO} & \varepsilon_{\lambda 1, HbR} \\ \varepsilon_{\lambda 2, HbO} & \varepsilon_{\lambda 2, HbR} \end{pmatrix}^{-1} \begin{pmatrix} \log \frac{I_{\lambda 1}(t_1)}{I_{\lambda 1}(t_2)} \\ \frac{DPF_{\lambda 1} L}{\log \frac{I_{\lambda 2}(t_1)}{I_{\lambda 2}(t_2)}} \\ \frac{DPF_{\lambda 2} L}{\log \frac{I_{\lambda 2}(t_1)}{I_{\lambda 2}(t_2)}} \end{pmatrix} \quad (5)$$

Where $\varepsilon_{\lambda 1/\lambda 2, Hb/HbO}$ is the extinction coefficient of the chromophore ($\text{mM}^{-1} \cdot \text{cm}^{-1}$), under the corresponding wavelength, $I_{\lambda 1/\lambda 2}(t_1/t_2)$ is the light intensity at times t_1 and t_2 , and DPF is the ratio of the actual path length of the optical photon to the illuminator detector distance. Solving the above equations for concentrations of chromophores [Hb] and [HbO] results in equations 6 and 7 [15]:

$$[HbO] = \frac{A^{\lambda 2} \varepsilon_{HbR}^{\lambda 1} - A^{\lambda 1} \varepsilon_{HbR}^{\lambda 2}}{(\varepsilon_{HbR}^{\lambda 1} \varepsilon_{HbO}^{\lambda 2} - \varepsilon_{HbR}^{\lambda 2} \varepsilon_{HbO}^{\lambda 1}) \cdot L} \quad (6)$$

$$[HbR] = \frac{A^{\lambda 1} \varepsilon_{HbO}^{\lambda 2} - A^{\lambda 2} \varepsilon_{HbR}^{\lambda 1}}{(\varepsilon_{HbR}^{\lambda 1} \varepsilon_{HbO}^{\lambda 2} - \varepsilon_{HbR}^{\lambda 2} \varepsilon_{HbO}^{\lambda 1}) \cdot L} \quad (7)$$

Where L stands for the minimum distance between the incoming light from the transmitter (source) and the attenuated light detected by the receiver and A refers to optical density.

Glotzbach et al. (2011) [17] used GLM estimator, Gaussian function and Boxcar function (to adjust HRF) and Zhang et al. (2011, 2012) [18, 19] proposed the use of recursive least- squares (RLS) algorithms to extract event-related concentrations and to decrease noise distortions from fNIRS data. In Zhang's work, the Monte Carlo code used for validation of the multi-layer head model in

3D with weighed photon migration. In 2016, Baker et al. [20], used an optimized version of GLM model to evaluate task related-cortical activation utilizing fNIRS hyperscanning. Baker's analyzing method has summarized in 5 main steps. 1) Wavelet transform is used for motion correction process and removal artifacts originated by movements, 2) Band-pass filtering with low and high cutoff frequencies 0.5 and 0.01 respectively has performed on the raw data, 3) MBLL has applied on the raw optical density data to extract hemoglobin concentration (in Baker's study only HbO is used for analysis), 4) To do test cooperation and inter block-rest period beta values were estimated, The similarities between cortical activation and task performance has achieved by calculating the covariance between fNIRS signal and real-time behavior [20]. In 2017, Wijekumar et al. [21], introduced a new approach for reconstruct voxel-space within the brain from fNIRS channel-space. This study has validated by a Visual Working Memory (VWM) task has generated the required voxels to compare fNIRS voxel-related to fMRI images. The more voxels represented in VWM network, the more similar fNIRS and fMRI results could be. This finding has further developed to validate fNIRS results. In the same year (2017), Pinti et al. [22] came up with the first-time proposed methodology to automatically identify metabolic events for fNIRS data analysis using the GLM model least square fitting method. In 2018, Morais et al. [23] have proposed an approach that automatically decides the location of fNIRS optodes from a set of predefined positions with the aim of maximizing the anatomical specificity to brain regions of interest. SPM is used for event estimation in the brain and the toolbox fNIRS Optodes Location Decider (FOLD) in MATLAB 2017a. The use of multi-modal systems to map human brain was increased in 2019 using fNIRS, EEG, MRI, and MEG. Yuan et al. [24], utilized fNIRS and EEG data to classify innocent and guilty groups and NIRS-SPM toolbox has used for data analysis and signal processing. The results of SPM mapping validated that the algorithm was successful to

separate innocent and guilty groups from each other. In 2019, Shuvra et al. [25], concluded that brain mapping using SPM method can positively discriminate pain perception from human brain regions. In order to show hemodynamic responses in three different view, 24 channels have used. In 2019, Urushidani et al. [26] have shown that brain mapping using fNIRS can provide assessment of regional hemodynamic responses associated with cortical brain activation and then neurotherapy is done by repetitive transcranial magnetic stimulation (rTMS) to improve motor recovery in subacute stroke patients. In Urushidani's work, a wavelet-based detrending algorithm is used in order to remove artifacts (mainly breathing, cardiac, spontaneous oscillation in tone of blood vessel walls or vaso-motion and other experimental errors). SPM made all these data and signal analysis methods available in one toolbox. This map is calculated using t-values to robust the cerebral cortex. Recently in 2019, Santosa et al. [27] concluded that the choice of the best set for GLM model contingent upon the duration of task. According to Santosa et al. work, estimation the parameters in GLM model which are important in duration of a specific task, for a task with a duration greater than 10 seconds is less important than a task which is shorter than 5 seconds. Besides, the sensitivity and SNR of the estimated model is highly correlated with the choice of basis set.

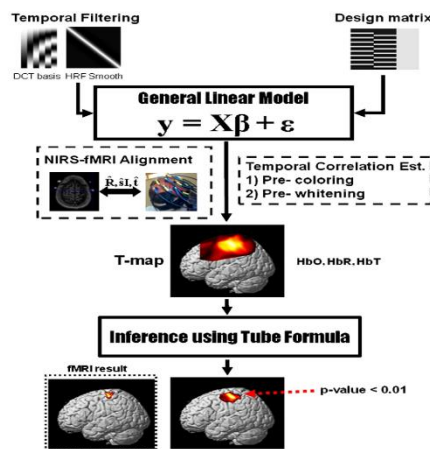


Figure 4. Schematics describing the NIRS-SPM framework in Ye's work [11].

HR type signals (i.e., fNIRS and fMRI) are naturally hard to interpret [10] so introducing a useful, comprehensive and user-friendly (user can manually control most of parameters) taking advantages of all previously done works seemed to be necessary [28].

2.2 Available fNIRS Toolbox and Software

Nowadays, many MATLAB-based software can be used for analyzing fNIRS data to obtain brain activity's mapping. In this section an overview of the mostly used fNIRS toolboxes have been provided.

HOMER: HOMER stands for Hemodynamic Optical Metabolic Evoked Response known as one of the well-established software used for fNIRS analyzing and it developed for NIRS data analysis by Huppert et al. in 2005 [29]. In 2009, Huppert et al. [30] further developed the previous toolbox known as HOMER with MATLAB scripts for analyzing fNIRS data and enable estimation and mapping of brain activation. While its purpose, functionality, and graphical user interface (GUI) are like the one developed in 2005, it added several important advancements and features:

- HOMER2 has some group and subject-level analysis support although it is limited to fixed functions and built into core code.
- HOMER2 used the MATLAB file format to store NIRS data.
- Much of the graphics based on HOMER2 are cleaner and simpler. In addition, there are fewer controls and the controls that are there are grouped into panels by function.

Despite above features, HOMER2 had some major problems. The most important one was the user was not able to change the code inside the core code. So other flexible and configurable toolboxes were needed. Continuing work of HOMER2, in 2019 HOMER3 has updated. The ability to perform group analysis has preferred HOMER3 over Homer2. It also provides more data forms in

its input. All functions and code is accessible by running the GUI, adding additional flexibility [31]. Other benefits of HOMER3 in comparison with HOMER2 are listed below:

- Ability to read/write more data file format than HOMER2.
- The modular/object-oriented design of Homer3 allows reader/writers of other formats to be easily added and exported to. snirf format.
- Ability to sub-divide data from one acquisition file by channels into independent data blocks and then independently process them. The HRF averages from different data blocks can then be viewed by clicking on the corresponding probe channels.
- HOMER3 does not change the original files that it uses for its analysis and clearly separates data into acquired (from original data files) and derived (any processed data).

NIRS-SPM: NIRS-SPM is a brain mapping based on statistic analyzing and a MATLAB-based open source software for analysis NIRS signals, developed at the Bio Imaging Signal Processing (BISP) lab at KAIST in Korea. It works based on the GLM model, NIRS-SPM not only provides activation maps of HbO, HbR, and total- hemoglobin, but also allows for super-resolution activation localization. More details are described in Ye et al. (2009) [11]. To remove the unknown global trends due to breathing, cardiac, vaso-motion, or other experimental errors, NIRS-SPM provides a wavelet-minimum description length (MDL) detrending algorithm (Ye et al. (2009) [11]). Figure 5 shows NIRS-SPM GUI with some of its features.

NIRS-SPM file format: NIRS-SPM was initially developed for the analysis of optical data from the continuous wave 24-channel NIRS system (OXYMON MKIII, Artinis). NIRS-SPM has been recently updated for analyzing the optical density data from the other systems including the ETG 4000 (Hitachi Medical Systems), the ImagentTM (ISS, Champaign, Illinois), the NIRO 200

(Hamamatsu Photonics), DYNOT-232 (NIRx Medical Technologies, LLC.), spectratech OEG-16, FOIRE-3000 (Shimadzu OMM), fNIR (BIOPAC Systems, Inc.), and CW6 (Techen Inc.).

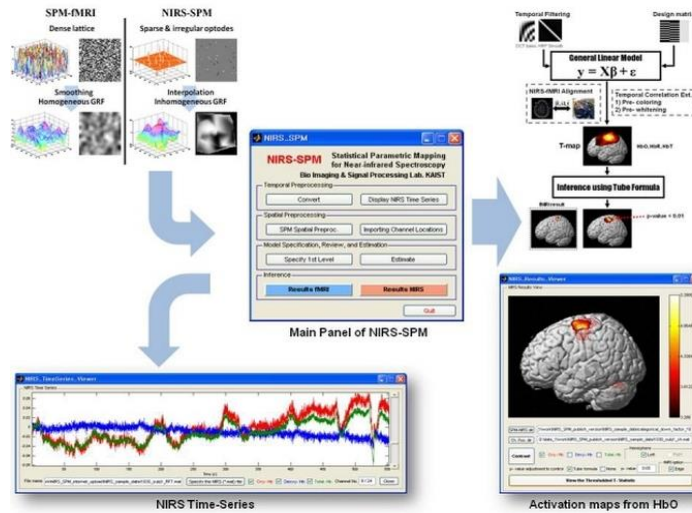


Figure 5. NIRS-SPM software developed by Bio Imaging Signal Processing (BISP).

Although NIRS-SPM provides many precious features for both signal processing and data analysis of fNIRS but its complexity and time consuming in data processing seemed the big issue with it. In other side, NIRS-SPM cannot show signal quality before going through MBLL to calculate concentration changes so SNR of processed signal it is not obtained.

nirsLAB: nirsLAB known as one of the completed analyzing package by NIRx Medical Technologies, LLC. It developed and introduced in 2016 by Xu et al. [32] for fNIRS signal processing and noise removal. Figure 6 shows the main window in nirsLAB. nirsLAB not only provided signal processing, noise and artifact removal on fNIRS signal but it also made it possible to visualize the time series response of measurement data and computed hemodynamic states within a viewing formats (e.g., stacked, 2D, scalp and cortical). However, filtering and artifact removal technique was two limitations of nirsLAB [10], based on the manual, the data preprocessing makes it possible to: remove irrelevant time intervals from data; eliminate step and

spike's artifacts from data; and apply band-, low- or high-pass frequency filters to exclude experimentally irrelevant frequency bands [32].



Figure 6. nirsLAB main window for signal processing and visualizing [32].

NIRSTORM: NIRSTORM is another useful tool for fNIRS data analysis. NIRSTORM firstly developed in 2011 by Tadel et al. [33] for EEG/MEG processing, featuring advanced databasing, visualization, signal processing, source localization and statistical analysis methods. The main window of NIRSTORM software has shown in Figure 7. Some features provided by NIRSTORM listed below:

- Classical within-subject analysis comprising motion-correction, MBLL and window-averaging.
- Optimal montages that optimize the sensitivity to a given cortical region of interest
- Ability for source reconstruction

In 2018, Machado et al. [34] modified NIRSTORM to optimize montage design targeting a predefined brain region.

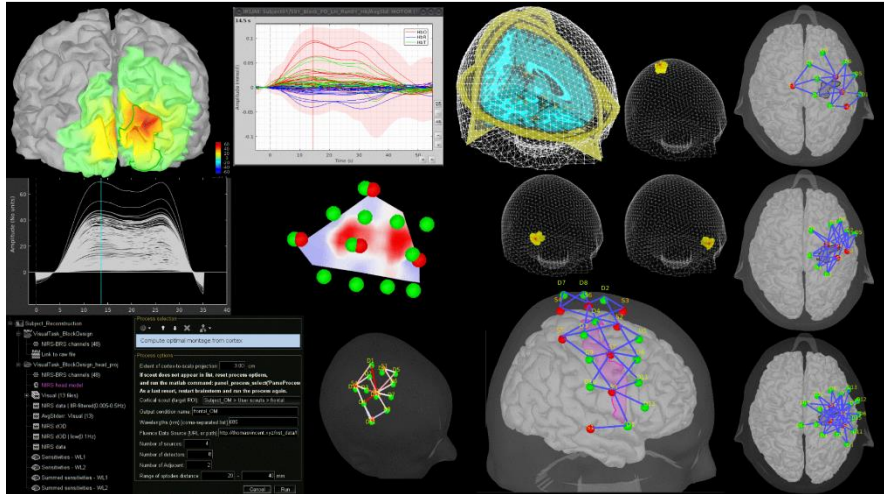


Figure 7. NIRSTORM window fNIRS data analysis [35].

One of main problems seen with NIRSTORM was high cost since it is not fully open source and license is required. Another problem was high computational time because of too many meshes used in modelling the brain.

Other toolboxes used in fNIRS studies:

- fNIRSOFT, a software for visualizing fNIRS signals (License required), from Biopac Systems, Inc., USA.
- fOSA-SPM, a software for functional optical signal analysis (License required) from the Biomedical Optics Research Laboratory (BORL) at University College London, UK.
- Imperial College Near Infrared Spectroscopy Neuroimaging Analysis (ICNNA), from the Imperial College London, UK.
- NAP (NIRS Analysis Package- open source code), from the Laboratory of Computational Neurodiagnostic at Stony Brook University, USA.
- NIRS Toolbox, an open source MATLAB-based toolbox for fNIRS analysis, from the Huppert Lab at the University of Pittsburgh, USA.

- NIRx NIRSlab, a software for fNIRS analysis based on NIRx systems (License required), NIRx Medical Technologies, LLC.

Based on the literature and referring to all mentioned software and toolboxes, there is no complete open source and easily available toolbox to analyze fNIRS signals. Most of companies provide more extensions for their own software only by purchasing the license. Table 1 represents a summary of available toolboxes and GUI for fNIRS analysis in the literature.

TABLE 1
fNIRS TOOLBOXES AND APP DEVELOPMENTS IN THE LITERATURE.

Researcher (Published year)	Toolbox or Analyzing app	Signal and Data Analysis Method	Advantage	Disadvantage
Huppert et al. 2005 & 2009, [29&30]	HOMER1 & 2	4th order Butterworth BPF (cutoff=0.01 to 0.2 Hz), GLM task analyzer and t-test	<ul style="list-style-type: none"> • The modular/object-oriented design • independently process data 	<ul style="list-style-type: none"> • Limited to fixed functions and built into core code • Limited file format
Ye et al. 2009, [11]	NIRS-SPM	MDL detrending algorithm+ BPF filter + GLM analyzer	<ul style="list-style-type: none"> • Task by task analyzer • More user defined functions • More readable file format 	<ul style="list-style-type: none"> • Complexity and time consuming • Unable to show signal quality
Tadel et al. & Machado (Modified) 2011, 2018 [33&34]	NIRSTORM	BPF (cutoff=0.005 to 0.08 Hz), Moving Average for detrending and smoothing	<ul style="list-style-type: none"> • optimal montage design • source reconstruction ability • Ability to remove bad channel (More noise) 	<ul style="list-style-type: none"> • Not open source • Read only. nirs format • high computational time

TABLE 1 (continued)

<p>Xu et al. 2016, [32]</p>	<p>nirsLAB</p>	<p>Optional filtering: BPF/LPF/HPF (cutoff=0.01 to 0.2 Hz)</p>	<p>visualizing the time series response of measurement data and hemodynamic states</p>	<ul style="list-style-type: none"> • Under NIRx license (Need to be purchased) skillful user to remove artifacts manually
---------------------------------	----------------	--	--	--

2.3 fNIRS Instrumentation and Signal

In 1984, David Delpy (University College London, UK) started to develop several fNIRS instruments and reported, three years later, the first quantitative measurement of various oxygenation and hemodynamic parameters in sick newborn infants including changes in oxygenated (HbO), deoxygenated (HbR) and total hemoglobin (tHb=HbO+HbR) concentrations, cerebral blood volume, and cerebral blood flow [36]. A four-wavelength system was described by Cope and Delpy in 1988 [37] and used as the basis of the single-channel continuous wave (CW) NIRO-1000, the first commercial system built in 1989 by Hamamatsu Photonics K.K.(Hamamatsu City, Japan). This instrument represents the first fruit of a long-lasting collaboration between University College London and Hamamatsu Photonics [36].

From 1980 to 1995, 9 more manufacturers were involved in fNIRS developments: 1) American Edwards Laboratories in collaboration with Duke University (NC), 2) Critikon (UK) and Johnson& Johnson (Bridgewater, NJ) with Zurich University (Switzerland), 3) Hitachi Ltd. Central Research Laboratories (Tokyo, Japan), 4) Near Infrared Imaging Inc. with the University of Pennsylvania (both in Philadelphia, PA), 5) NIR Systems, Inc. (Laurel, MD) and Edwards Lifesciences Corp. (Irvine, CA) with Johns Hopkins University (Baltimore, MD), 6) Radiometer (Copenhagen, Denmark) with Copenhagen University (Denmark), 7) Sclavo (Siena, Italy) with

the “Istituto Superiore di Sanità”(Rome, Italy), 8) Shimadzu (Kyoto, Japan) with Hokkaido University (Sapporo, Japan), 9) Somanetics Corporation (Troy, MI), and 10) NIRx Medical Technologies, LLC with university of Minnesota, Minneapolis. Later on, in 2002, Artinis Medical Systems located in Netherland in collaboration with g.tec Medical Engineering (1999, Austria) developed fNIRS systems.

Almost all fNIRS instrumentations work based on two main characteristics [36, 38]:

1. Emitting NIR light at the range of 650 to 1000 nm.
2. Stretchable fiber optics cap to hold transmitter and receiver optodes.

There are three type of systems based on NIRS technique. These systems are categorized to continuous wave (CW), frequency domain (FD) and time resolved (TR) [39]. Table 2 listed the main characteristics and other measurable parameters for three different types of fNIRS systems. The NIR light can penetrate within the brain to maximum one half of the distance between source (transmitter) and detector (receiver) so that it is controlled by the configuration that has used to define source-detector distance [36]. During data collection, sources are fixed into an optode holder and they located on the predefined positions on the scalp in order to allow NIR light to go through the skull and to collect information from cortical layers of the brain. A fraction propagates through the tissue on a banana-shaped path back to the surface where it is then detected by a NIR-sensitive photodetector (Figure 8). In human tissue, water is mostly transparent to the NIR light (650-1000 nm) and the emitted light can penetrate the cranium and reach sufficient depth [41]. This characteristic of optical light in which tissue is relatively transparent to light is often referred to as optical window in literature (Figure 9). Although absorption and scattering of the tissue's parts (e.g. collagen, proteins, fat etc.) remain constant, some chromophores such as HbO, HbR and

cytochrome oxidase are strong absorbers for NIR light with their concentrations changing with metabolism and blood flow.

TABLE 2

MAIN SPECIFICATIONS AND PARAMETERS MEASURED BY DIFFERENT TYPES OF fNIRS SYSTEMS.

Researcher (Published year)	Main Specifications						
	Type of system	Sampling Frequency (Hz)	Spatial Resolution (cm)	Penetration Depth	DPF measurements capability	Device Cost	Equipment/ Company
Venclove et all. (2015) [43]	CW	≤ 5	≤ 2.5	Low	No	Low	Biopac
Davies et all. (2016) [44]	CW and FD	≤ 2	≤ 2.5	CW=Low FD=Deep	Yes	CW=Low FD=High	NIRO 200NX (Hamamatsu), ISS OxiplexTS
Abdalmalak et all. (2017) [45]	TR	≤ 1.5	Deep	Deep	NA*	Very High	Proposed Design

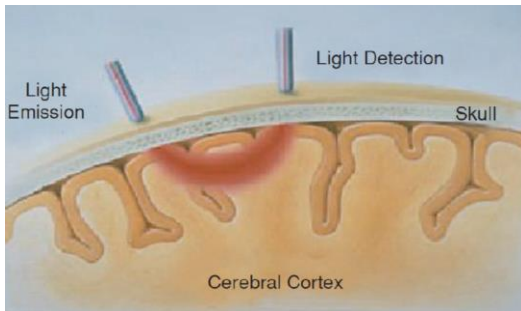


Figure 8. Principle of fNIRS signal acquisition [40].

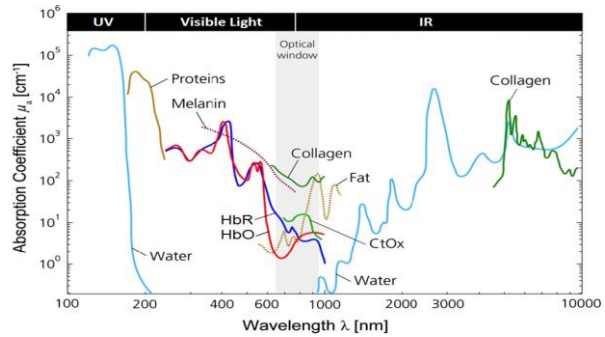


Figure 9. Optical window of NIR light for different tissue's part [42].

As it has shown in Figure 8, light intensity has emitted using a dual wavelength LED and these intensities can be quantified with the Modified Beer-Lambert Law (Discussed in Method) to obtain

concentration changes. After achieving concentration changes, hemodynamic response has defined to show the correlation between local blood oxygenation and neuronal activation. Wolf et al. [46] showed that local HbR and HbO concentrations in the brain affected by three main factors:

1. local cerebral metabolic rate of oxygenation (CMRO₂)
2. regional cerebral blood flow (rCBF)
3. cerebral blood volume (CBV)

These three factors known as neurovascular coupling and they usually occur during neuronal activation and at the same time. This hemodynamic signal can normally be seen with a delay 5-8 seconds after starting of stimulus/task [47]. Figure 10 shows typical fNIRS signals.

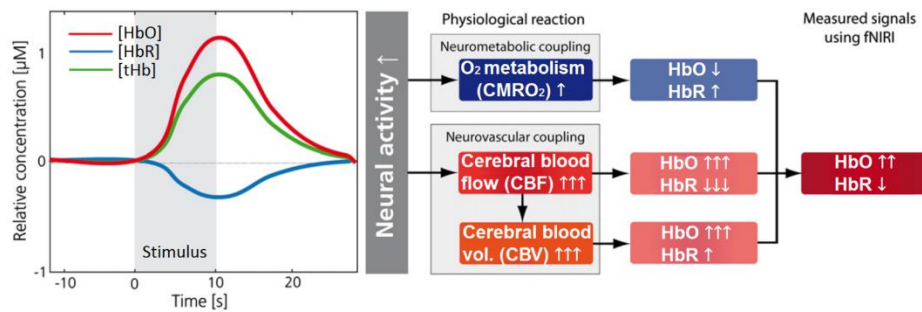


Figure 10. Typical fNIRS signals. HbO: oxy-hemoglobin, HbR: deoxy-hemoglobin, tHB: total hemoglobin [42].

2.4 Experiments and Paradigms

To start data collection and create the dataset in fNIRS systems, we need to design the experiment. There are many experimental paradigms in fNIRS studies. Selecting each paradigm contingent upon subjects and study's questions. Based on age of subjects we may apply different coefficients in MBLL calculations (See method). Main study question and hypothesis is another factor in choosing the experimental paradigm. Some of these questions are listed below:

- How to consider changes in brain function in control or affected population?

- What kinds of tasks are needed to use to evoke the hemodynamic response?
- What regions is needed to study?

In 1997, Fallgatter & Strik [48] introduced continuous performance test to evaluate attentional performance along with EEG-P300 paradigm. In 2003, Herrmann et al. [49] developed the previous test by combining it with Verbal-fluency test (VFT) and they concluded that NIRS is suitable for the measurement of blood oxygenation changes in frontal brain areas that are related to the cognition. In 2004, Kuboyama et al. [50] studied the effect of finger tapping at different rates on the left primary motor cortex. In Kuboyama's work one trial included 20-seconds tapping at a specific frequency and 40-seconds rest period. Nine right-handed and healthy subjects, mean age 27.2 (Std=4.8), 2 females, were asked to press a button with their right index finger at three different frequencies which were determined based on individual's maximum effort (ME), 50% ME and 25% ME. The 25% and 50% ME conditions were randomized and regulated by the sound. Each trial corresponding to one tapping frequency was repeated 3 times. In total each subject performed 9 trials. The measurements were conducted with 24-channel 2-wavelength Hitachi ETG-100, but the authors selected only one data channel close to the EEG position C3 for the analysis. The sampling rate was 10 Hz. Figure 11 has shown the experimental paradigm in Kuboyama's study.



Figure 11. A trial for the Finger tapping experiment in Kuboyama's study [50].

The achievements of finger tapping task done by Kuboyama are summarized below:

- Only in the ME condition the increases of Hb, HbO and tHb changes from their baseline are significantly different.

- The increases of Hb, HbO and tHb changes from their baseline in the ME condition were significantly higher than that in the 50% ME and the 25% ME condition.
- The increases of Hb, HbO and tHb changes from their baseline in the 50% ME condition were not significantly different from that in the 25% ME condition.

Some researchers have also used finger tapping and whole hand grasping to assess hemodynamic concentration changes in the brain [51]. Figure 12 has shown the finger tapping and hand grasping experiment conducted by Kashou et al. (2016) [51].

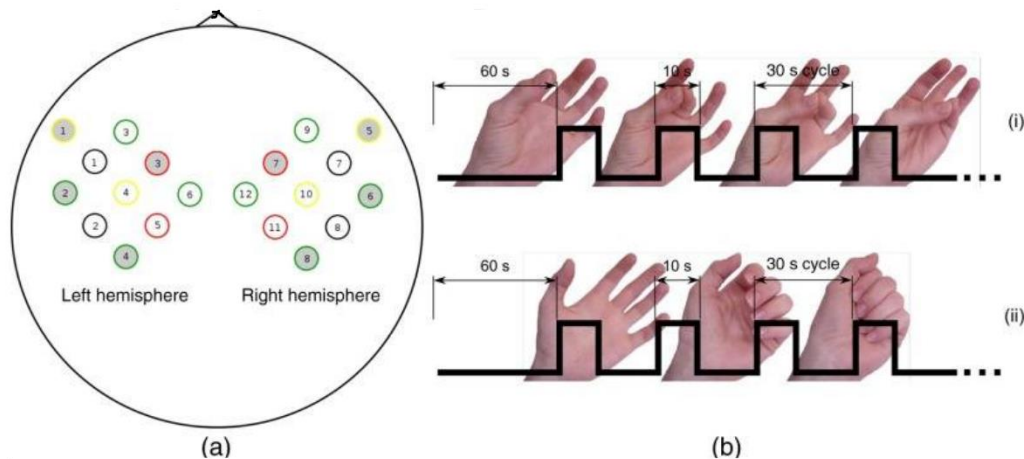


Figure 12. Finger tapping and hand grasping experiment. a) Optode configuration (Transmitters (gray) and receivers (white)) based on 10/20 system. b) The methodology for i) finger-opposition and ii) grasping tasks trials [51].

In 2010, Yanagisawa et al., [52] acquired fNIRS data during a color-word matching Stroop task. Stroop task has earlier used for fMRI data in 2000 by Leung et al. [53]. In Stroop task, the subject was instructed to determine whether the color of the top row letters corresponded to the color name written on the bottom row. Figure 13 shows an example of congruent and incongruent conditions of the color-word matching Stroop task used in Yanagisawa's study. In 2012, Wijekumar et al. [54] used Visual stimulation, related to the visual cortex. In 2017, Huppert et al. [55] modified

Stroop task in NIRS-SPM app to demonstrate the feasibility and initial results using a portable 8 transmitters and 4 sensors fNIRS system to measure brain activity from participants within residential care community centers.

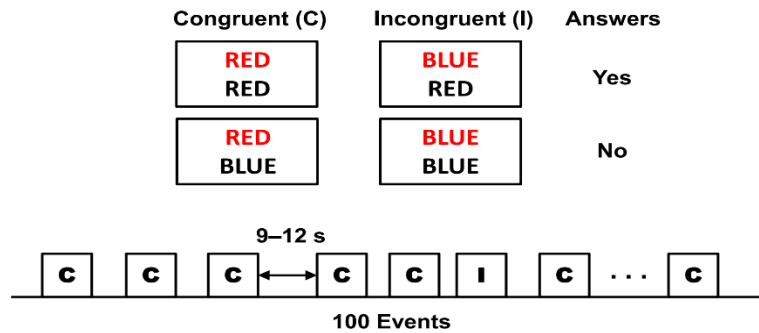


Figure 13. Example of congruent and incongruent conditions used in Yanagisaw’s study [52].

2.4.1 Test Design Strategies

Many researchers adapted 10/20 EEG standard system to decide optode locations on the scalp. Figure 14 shows 10/20 standard system with electrodes in the frontoparietal region. Based on 10/20 system, then researchers can perform further design strategies.

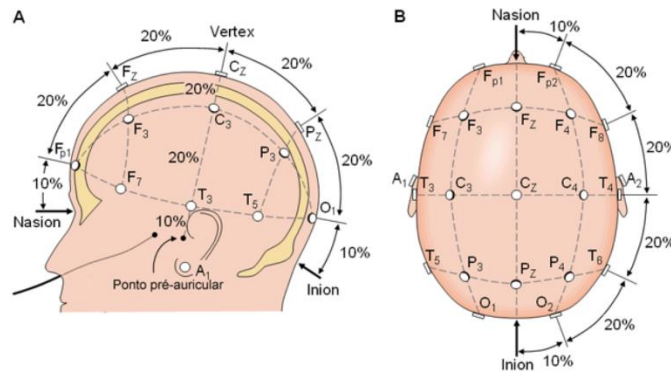


Figure 14. Mounting on the 10/20 electrode positioning system [56].

General Block Design: Since the type of signal for both fNIRS and fMRI is hemodynamic signal, to model the block in fNIRS, previous studies used fMRI approach [57]. The boxcar function is determined based on the task duration. Figure 15 shows a typical boxcar function with task and rest phases. To reconstruct a hemodynamic response, a canonical gamma function (HRF) has been

convoluted with boxcar function. Figure 16 shows convolution of canonical HRF with boxcar function to model fNIRS signal. Better efficiency will be achieved when the rest timing is equal to average stimulation time of the task-related conditions [58].

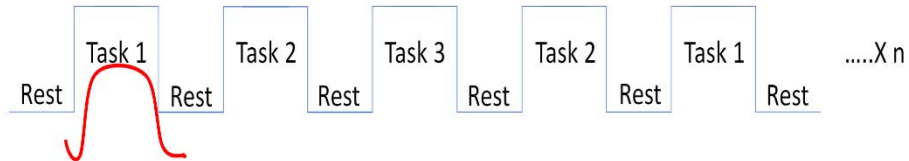


Figure 15. Boxcar function for a typical task. Rest period should be designed at the beginning of experiment to enhance SNR.

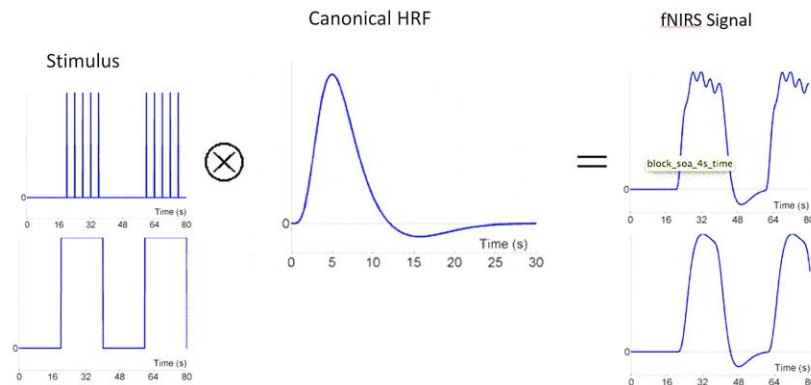


Figure 16. Modified general block design for fNIRS based on fMRI methodology.

Montage Design: Depending on the area of study/region of interest (ROI) and number of channels/probe the optode configuration will be mounted. Prior to montage design a tradeoff between some factors should be considered:

- Number of channels: Children vs Adult
- Temporal resolution for data acquisition
- Subject tolerance

Number of channels are directly related to the distance between source-detector in the montage. Table 3 shows the relationship between subject's age and source-detector distance in literature. As it has shown in Table 3, designing the montage depends on the ROI, subject's age and tolerance and the distance between S-D.

TABLE 3
IMPORTANT FACTORS IN DECIDING THE NUMBER OF CHANNELS.

Researcher (Published year)	ROI*	Subjects	Age	S-D* Distance
Nishiyori (2016) [59]	primary motor cortex	neonates and infants	Less than 2	2–2.7 cm
Chevalier et al. (2019) [60]	Left and right frontal lobe	60 children	5-6 and 8-9	3 cm
Gao et al. (2011) [61]	left temporal	8 adults	21~31	3 and 3.5 cm

*S-D=source to detector distance, ROI=region of interest.

Figure 17 shows a typical montage design for different studies.

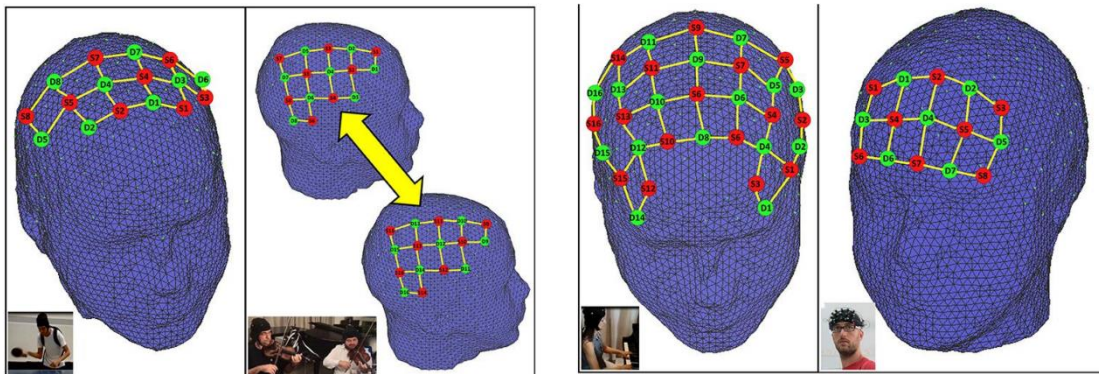


Figure 17. fNIRS probe setup used in each experiment. Top left: supplementary motor and primary motor cortex (23 channels). Top right: hyperscanning right hemisphere motor and temporo-parietal junction (22 channels/subject). Bottom left: dorsolateral prefrontal and primary motor cortex (51 channels). Bottom right: forehead headband covering prefrontal cortex (22 channels) [62].

Optode Positioning: Depending on how accurate the design should be, the location of each optode can demonstrate where the signal came from within the brain. Some researchers used anatomical scans (CT, MRI) to decide the position of optodes on the scalp. Chen et al. (2017) [63] determined fNIRS channel locations using MR scans. The methodology used in Chen's study for optode

localizing has shown in Figure 18-a. For spatial registration, Chen used “MRICron” which is a MATLAB- based software. They modified a 3D head model based on Montreal Neurological Institute (MNI) coordinate (in mm). Then, they used a fixed distance between each source–detector pair to linearly calculate the unmarked detectors (Figure 18-b). This methodology also has used in NIRS-SPM app.

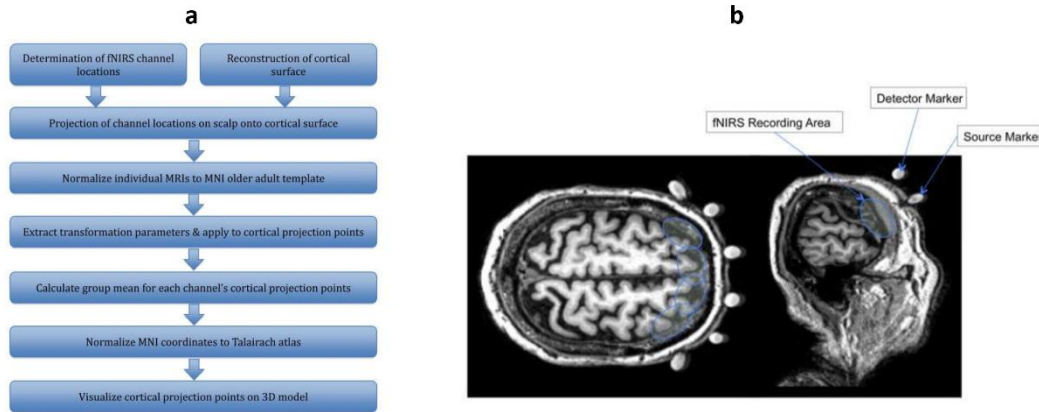


Figure 18. Using fMRI to find optode locations. a) Summarizes the steps involved in data processing and analysis. b) Anatomical MRIs of fiducial markers [63].

To locate channels, Chuang et al. (2018) used 3D digitizer by Polhemus to find the precise optode location [64]. Figure 19 has shown 3D digitizer in the Chuang’s study on brain electrodynamic and hemodynamic signatures against fatigue during driving.

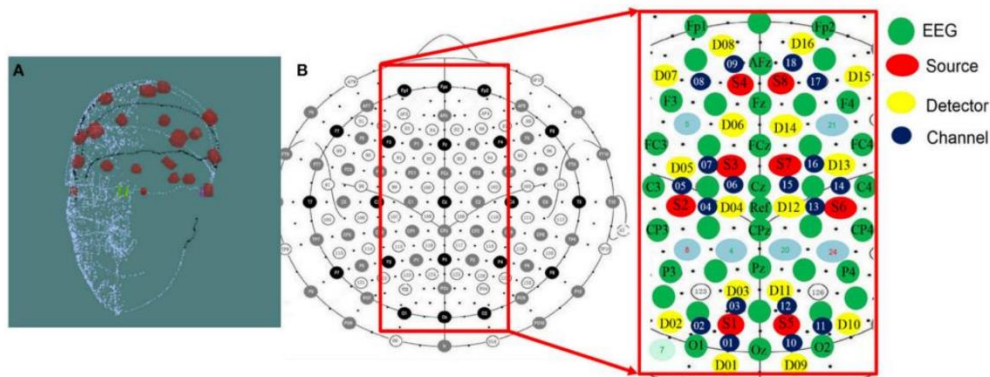


Figure 19. Optode locations using 3D digitizer. (A) 3D Digitizer and (B) EEG-NIRS channel location. The 3D Digitizing electrode positions are used to input the three-dimensional head shape [64].

Although 3D digitizer can be used in studies which need accurate channel positioning, it is costly (more than 4000 US dollars) and most of researchers are looking for alternative options. There are some open source toolboxes which are using atlas viewer of the brain to register the optode. NIRS toolbox, HOMER2, fNIRSOptodes' Location Decider (fOLD) are some of them. Figure 20 shows these commonly used toolboxes and software for channel registration in fNIRS.

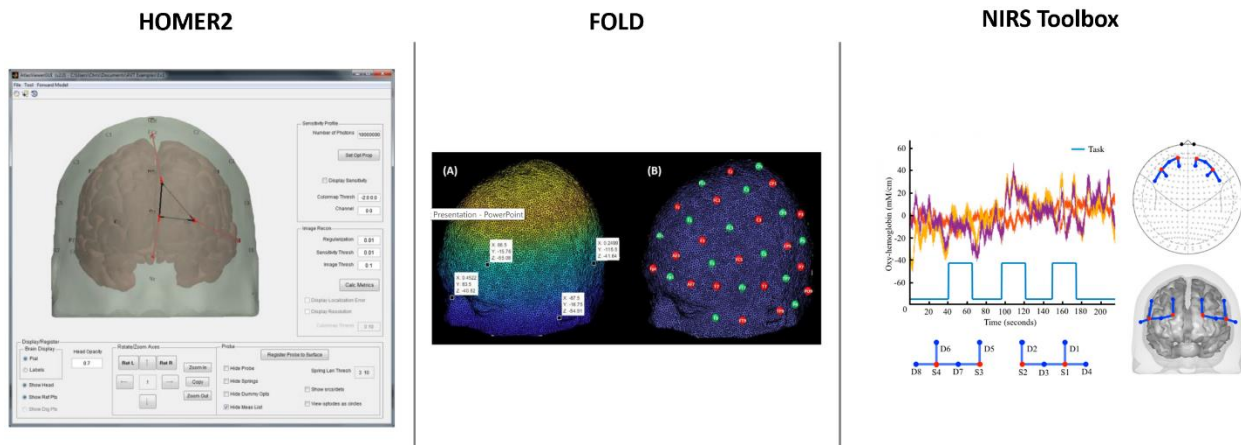


Figure 20. Commonly used open source toolboxes for channel registration.

2.5 Noise Removal

fNIRS signal contains much noise due to its sensitivity to environmental light, electronic design, subject's movement, physiological characteristic of the subject etc. Very-low-frequency noises caused by optodes shifts or slow cardiac/vascular artifacts known as the most occurrence noises in fNIRS systems [13]. So that these noises and artifacts can distort the output signal of the device and then decrease SNR of the signal [28], the sources of them should be recognized and a proper technique (e.g. block averaging, smoothing and low-pass filter [65]) should be design and manipulated to remove or eliminate them. This section tends to review noise sources and techniques to remove them based on literature.

2.5.1 Instrumental Noise

There are three main types of noise in fNIRS instruments that should be considered in software design:

- Shot Noise
- Dark Current
- Thermal Noise

Shot Noise: In Photomultiplier Tube (PMT) - based systems, shot noise is based on the quantum nature of the photons detected by photodetector and cannot be avoided completely by technical tools [66]. Having linearity and uniformity, the photons arrive independently of each other, resulting in random fluctuations in photon-to-electron conversion in the detector over time. Without internal amplification, the shot noise power is proportional to the square root of the average intensity (the number of incident photons) [42]. This results in the fact that the accuracy of the measurements increases with the intensity of the detected light in a constant time window. Shot noise can be minimized by shielding the detector from background radiation, e.g. with opaque covers [67], or Butterworth band pass filters [42].

Dark Current: Current owing in the detector in completely dark conditions (no incident photons) and is highly influenced by the temperature of the material. To minimize dark current due to thermal generation, the device can be cooled [68].

Thermal noise: Thermal noise is a phenomenon, also known as thermal agitation, which is due to the random motion of free electrons in a conducting material caused by heat [69]. It resulted from Brownian motion of charge carriers in resistors internal and external to the detector and is proportional to the resistor value. Equation (7) illustrates effective factors in thermal noise [69].

$$\bar{u}^2 = 4k_B TR\Delta f \quad (7)$$

Where \bar{u}^2 is the mean square voltage variance, k_B is Boltzmann's constant, T is the absolute temperature of the resistor in Kelvin, R is resistor value in Ω and Δf is the spectral bandwidth in Hz.

2.5.2 Motion Artifact

Motion artifact refers to spikes and usually couples with baseline shift in the measured intensities caused by insecure optode placement on the subject's head [12, 70, and 71]. While spikes could be easily spotted, baseline shift is difficult recognized and often confused as hemodynamic response (Figure 21). In many cases, there often exists global drifts in the NIRS measurements due to variety reasons, including subject movement during the experiment, blood pressure variation, long-term physiological changes, or instrumental instability. Moreover, the general drift signal's amplitude is related to the signal resulted from brain activation.

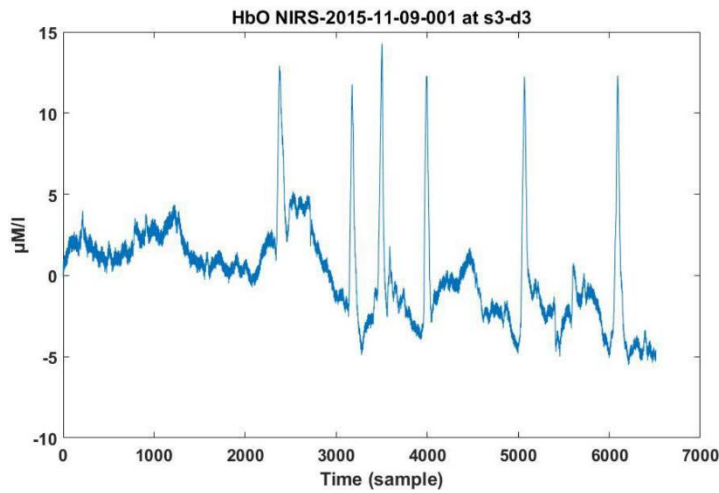


Figure 21. Spikes and baseline shift [72].

There are several methods in literature to remove motion artifact on fNIRS data:

Principle Component Analysis (PCA): This method tries to find an orthogonal transformation to the original data set composed of N measurements to produce N uncorrelated components [73, 74]. PCA is based on the observation when motion artifact occurs, similar peaks appear at the same time points in different channels with different levels of amplitude. This method requires a highly correlated peaks and a good estimation of the number of components to extract the systematic variance [72].

Correlation-based signal improvement (CBSI): Cui et al. [75] used observation of simulation and empirical data. Based on Cui's work, when motion artifact occurs, the HbO and HbR changes were positively correlated. Although Cui's proposal was simple, fast, and can be fully automated, however the assumptions were not realistic which may lead to unreliable result.

Spline interpolation: This method proposed in 2010 by Scholkmann et al. [76] applies only on the detected motion artifacts and leaving the remaining part of the signal unmodified. One of known drawback of the spline approach is that it needs to be preceded by a reliable technique that identifies the motion artifacts. If the artifacts are difficult to detect, spline interpolation will not be applied appropriately and thus the technique will not improve the signal. However, an advantage of the spline approach is the ability to remove baseline shifts.

Discrete Kalman filter: Discrete Kalman filtering proposed by Izzetoglu et al. (2010) is a channel-by-channel approach [77]. The Kalman filter is a two-step filter: 1) at time= t_k , a prediction of the state x at time= t_{k+1} and of its uncertainty is computed, using knowledge on prior states. 2) When the measured signal at time= t_{k+1} comes, it is used to update and correct the predicted state x_{k+1} , which is then used again in the prediction of the next state [71]. HOMER2 open source MATLAB toolbox provides Discrete Kalman filter option to remove motion artifacts. In order to

model the signal over the frequency range using Kalman filter, it is necessary to convert the data points to the sampling frequency of the fNIRS system (less than 10 Hz). So down sampling the data as part of the Kalman filter correction procedure should be performed [71].

Discrete Wavelet Transform: In 2012 Molavi et al. [78] proposed a channel-by-channel approach called Discrete Wavelet Transform (DWT). They used Daubechies 5 (db5) wavelet and it applied to every channel data series for a few levels of decomposition. The motion artifact removal on fNIRS signal in Molavi’s work has shown in Figure 22. In wavelet method it assumed that the measured signal is a linear combination of the physiological signal of interest and the artifacts. So that the detail wavelet coefficients have a Gaussian probability distribution and that the hemodynamic response is smoother and slower than motion artifacts [71].

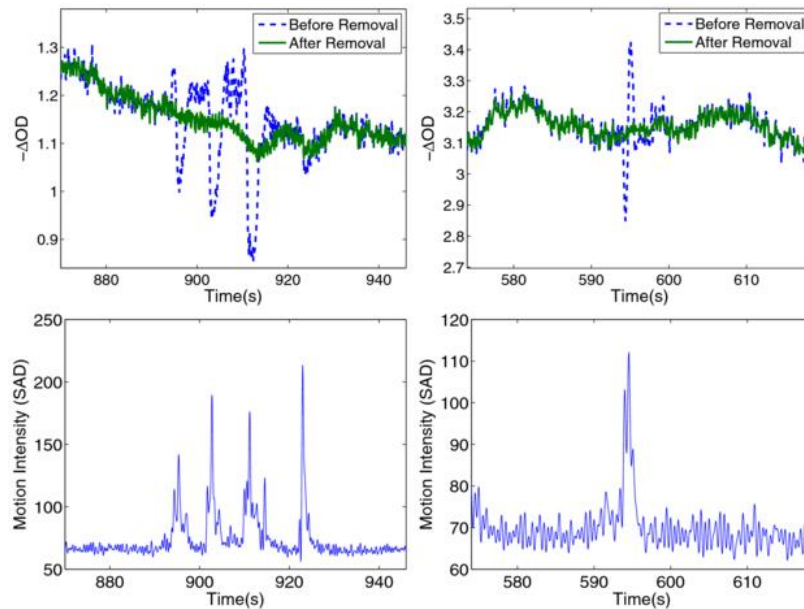


Figure 22. Performance of wavelet transform on removing motion artifact: in the Molavi’s method (top) with the motion reference signal extracted from videotape (bottom) [78].

Some researchers also used DCT to remove discontinuity and artifact in EEG systems [79]. Up to now, there is no DCT method to remove motion artifact on fNIRS signal.

2.5.3 Physiological Noise

fNIRS signal is a mixture of multiple components caused by neuronal or systemic activities where neuronal activities may be evoked by the stimulus (functional brain activities) or not (spontaneous brain activities) [72]. Any components caused by non-functional brain activity are considered as physiological noise [42]. An effective noise cancellation method should be able to remove noises originated from physiology such as heartbeat (1–1.5 Hz), respiration (0.2–0.5 Hz) and low frequency content resulting from blood pressure fluctuations (Mayer waves; 0.1 Hz) [8]. High and low frequency components can be removed on fNIRS signal using low pass filter (LPF) and high pass filter (HPF) respectively. Referring to the literature, several cutoff frequencies have been reported. Baker et al. [20], Wijekumar et al., [21], Cui et al. [75], Keles et al., [80] and Yücel et al. [81] used an LPF and HPF with cutoff frequencies of 0.5 Hz and 0.01 Hz, respectively.

Figure 23 shows physiological noises and artifact along with their impact on fNIRS recording.

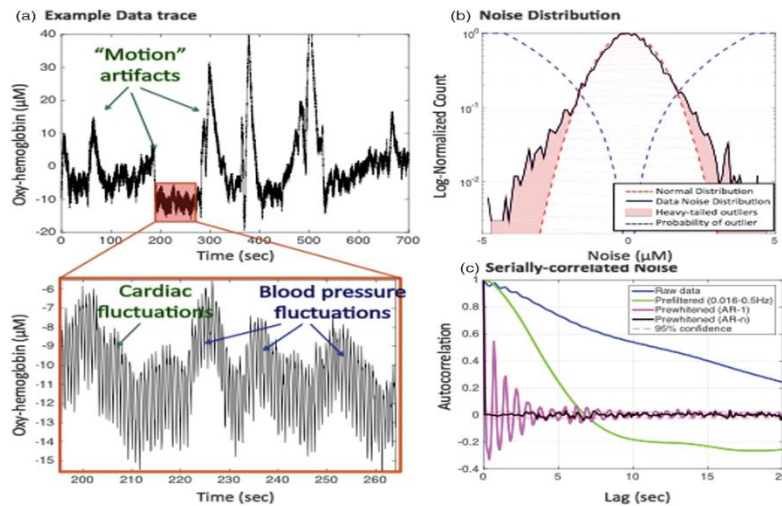


Figure 23. Typical Noises and artifacts in fNIRS signal. a) Motion artifact, b) A histogram noise distribution of the data and the best-fit ideal distribution (dotted red line) and c) The temporal autocorrelation of the recorded raw data along with the autocorrelation after filtering and AR pre-whitening [82].

Reference channels (also called short separation channels) [83, 84] known as an outstanding method for physiological noise removal. In short separation channel, the distance between optode are less than 1 cm and the superficial signals on the brain can be achieved. Note that, the optimum distance between source-detector in fNIRS is around 3 cm for adults (Table 2).

Savitzky-Golay: In 2018 Jahani et al [85] used Savitzky-Golay (S-G) filter for fNIRS data smoothing as well as motion artifact removal. S-G also known as a digital polynomial filter or least square smoothing filter, is a digital smoothing filter that substitutes each value of the signal series with a new value, which is obtained from a polynomial fitting to the successive subset of adjacent data points. The fitting is performed by the linear least squares fitting to $2n+1$ neighboring point, while n can be equal or greater than the order of the polynomial. The more neighbors used in the averaging process, the smoother the signal becomes. Least squares smoothing suppresses noise while keeping signal information. Figure 24 is shown the performance of S-G filter on fNIRS signal.

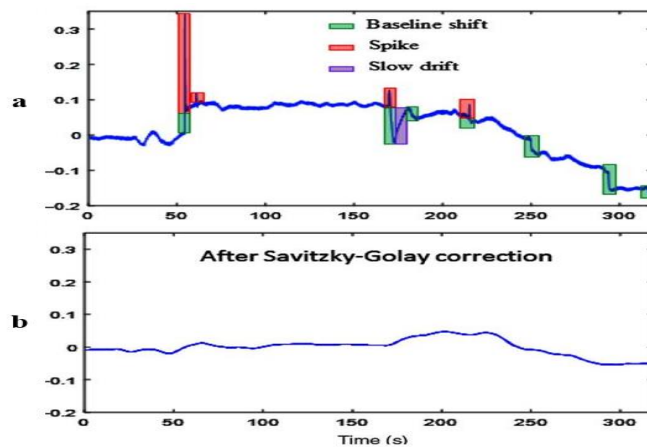


Figure 24. Performance of S-G filter on fNIRS signal. (a) An example of an OD change time course at 690 nm contaminated by three types of motions: baseline shifts (green), high-frequency spikes (pink), and slow drifts (violet). (b) The baseline shifts and slow drift motions are corrected by S-G filter with $n=300$ ($2n+1=601$ neighboring points) [85].

Moving Average: As its name suggests, the moving average filter operates by averaging a number of points from the input signal to generate each point in the output signal. This procedure is repeated so that a moving window of M points is used to calculate the average of the data set. The algorithm takes the mathematical expression:

$$f(x) = \begin{cases} \frac{\sum_{k=0}^{N-1} S(i+k)}{N} & , i > 0 \text{ and } i < m - (N - 1) \\ 0 & , \text{ Otherwise} \end{cases} \quad (9)$$

Where $S(i+k)$ is the input signal, $y(i)$ is the output signal, N is the number of points in the average and m the total number of data points.

CHAPTER 3

MATERIAL AND METHODS

3.1 System Requirement

Software: To develop a GUI, it is necessary to specify under which environment the program needs to be coded. In this work, the code has been developed under MATLAB R2019b. MATLAB versions starting with R2017a are also compatible. The following toolboxes are necessary to use all features in the designed GUI:

- Image Processing Toolbox (To process 2D, 3D, and arbitrarily large images)
- Signal Processing Toolbox (To design filter and analysis, resampling, smoothing, detrending, power spectrum estimation etc.)
- Statistics and Machine Learning Toolbox (To describe, analyze, and model data)

Hardware: The GUI has been developed and tested on Intel® core™ i7 CPU 4.20 GHz, 16.00 GB RAM. However, the designed GUI works on any computer with MATLAB 2017 and newer with approximately 2.0 GB RAM. Note that the process for estimating temporal correlations requires large amount of memory. Depending on total recording time, more than 2.0 GB RAM will be required.

3.2 GUI Architecture

The flowchart of the proposed GUI has shown in Figure 25. These steps have been followed for programming in MATLAB R2019b. The general block diagram for the designed GUI has shown in Figure 26. The app has divided into two main stages: 1) Signal Processing and 2) Data Analysis.

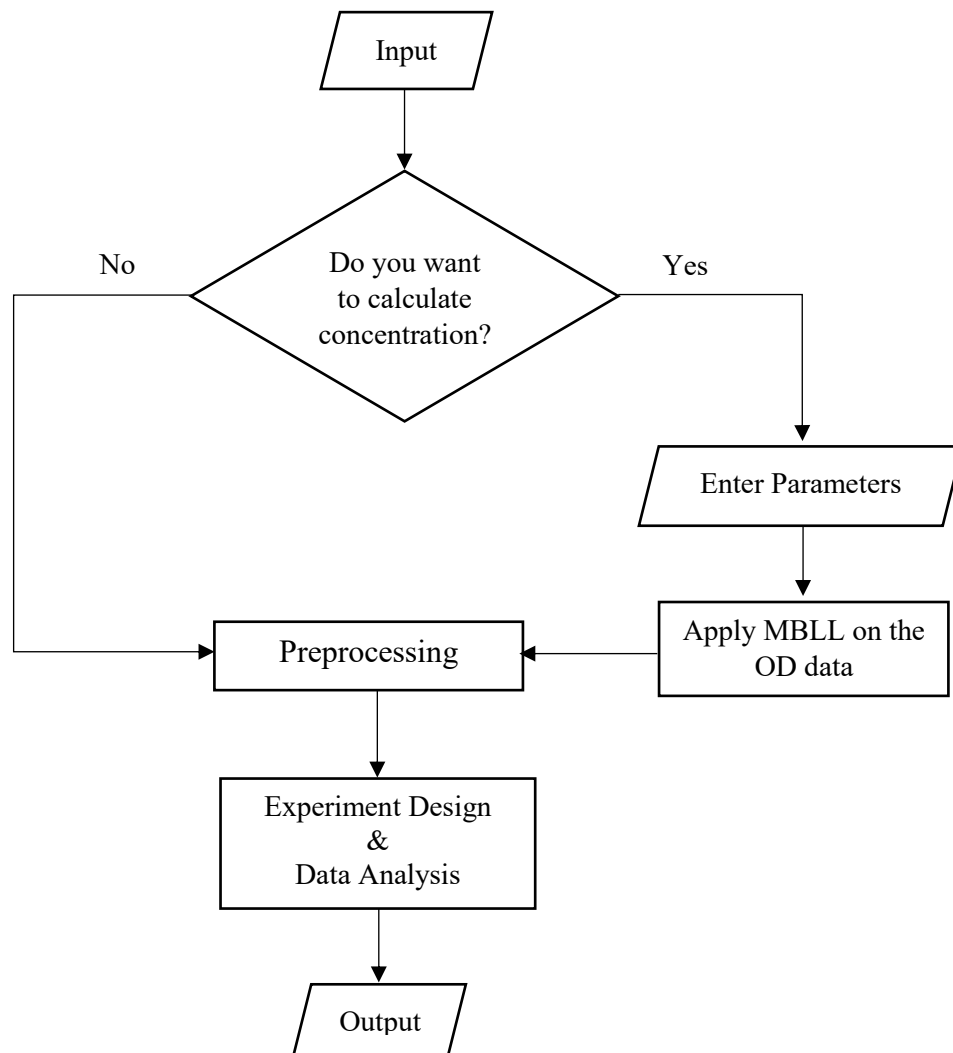


Figure 25. The flowchart for the proposed GUI.

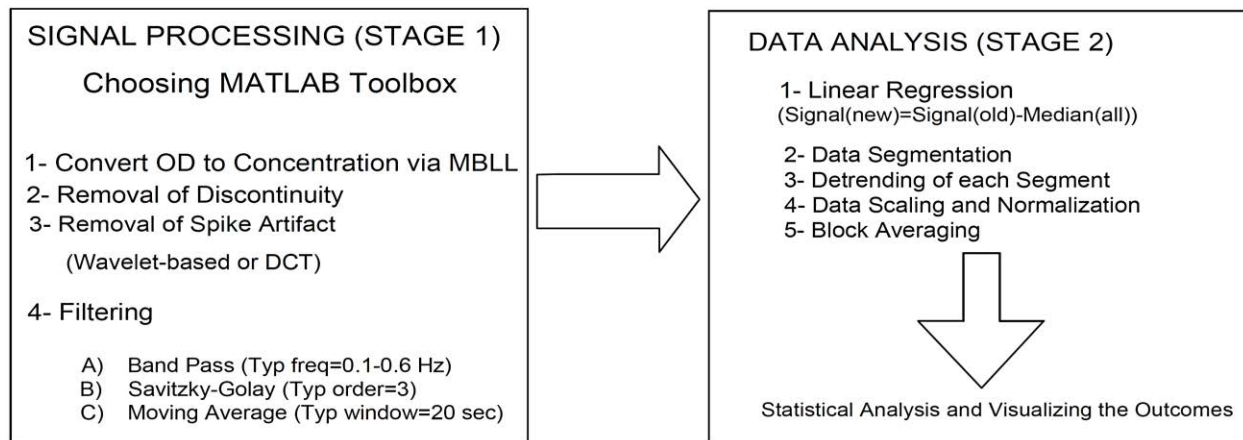


Figure 26. The steps used for signal processing and data analysis in the proposed GUI.

3.3 Data Acquisition

In this thesis, a hybrid EEG/fNIRS system (g.tec/ARTINIS) with 8 high-power transmitters for central/motor cortex area has been used. In order to verify the GUI performance, a 4-channels fNIRS system with same optode configuration as ARTINIS device has developed and constructed in the laboratory scale. The transmitters are LED based and emit light at nominal standard wavelengths of 760 and 850 nm. The 8 transmitters and 2 receivers result in 2 by 4 fNIRS channels and are based on the fNIRS technology of Octamon+ from ARTINIS (<https://www.artinis.com>). The optodes were placed on the left and right motor cortex at 8 different emitter-detector-pair locations. The source-detector separation was approximately 3 and 3.2 cm for high-power (motor cortex) and low-power transmitters (forehead), respectively. The optode configuration for ARTINIS and the developed prototype system has shown in Figure 27. The fNIRS data is sampled at 10 Hz but is up-sampled to 250 Hz.

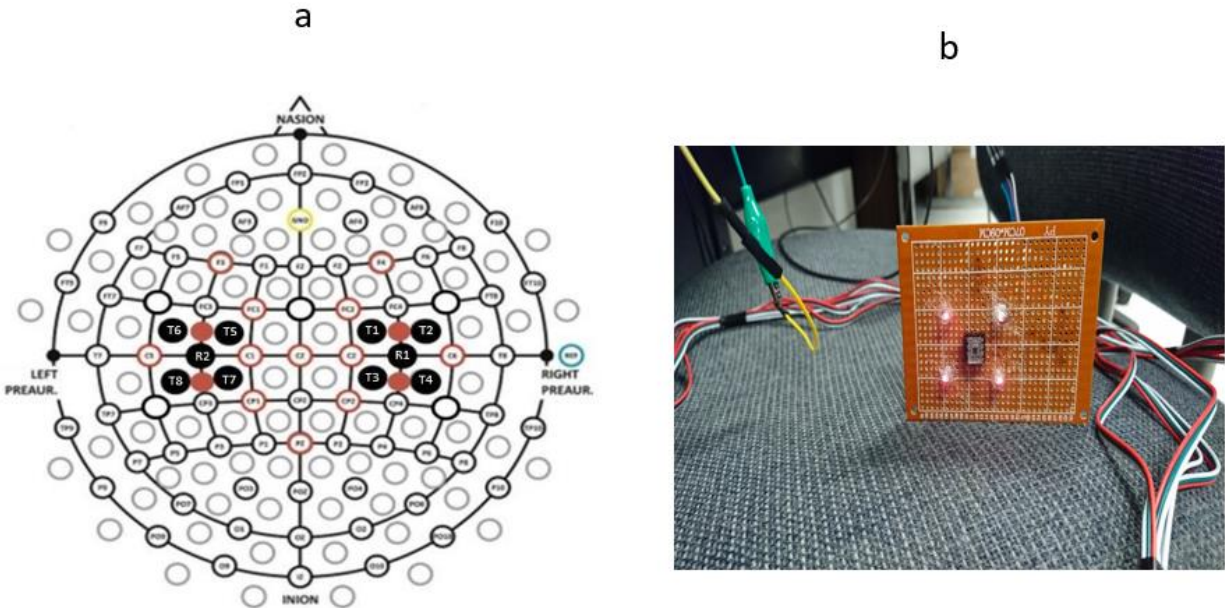


Figure 27. Optode configuration based on 10/20 system: a) In ARTINIS system, b) 4-channels optode configuration in the designed prototype system. Optode distance in both devices set to 3 cm for motor cortex area.

The SIMULINK model provided by g.Nautilus can save raw data either as OD or concentration changes. The SIMULINK model for fNIRS data acquisition has shown in Figure 28.

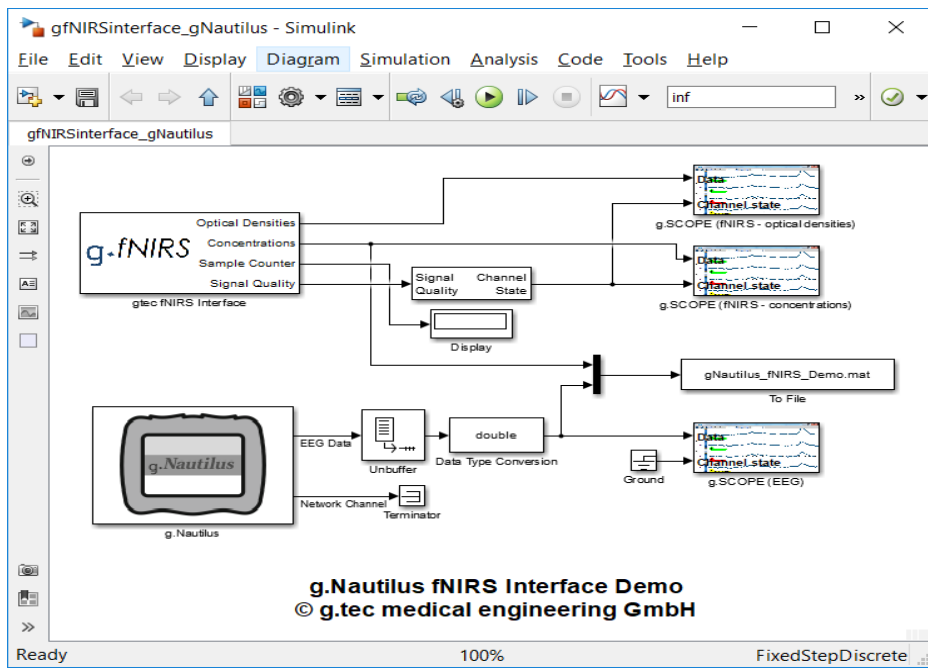


Figure 28. SIMULINK model by g.Nautilus for hybrid data acquisition from fNIRS and EEG.

Based on purpose of this project, that is fNIRS signal processing and data analysis, fNIRS data has been discriminated from EEG for further analysis in the proposed GUI.

3.4 Data Conversion

Before starting fNIRS signal processing, the data type should be identified. The input dataset can be either Optical Density (OD) or concentration changes (See section 3.3). If the data type is OD, then the user should enter the required parameters (Figure 29-b) for MBLL to calculate concentration changes based on equations 1-6. Figure 29-a, has shown the main window for the designed GUI.

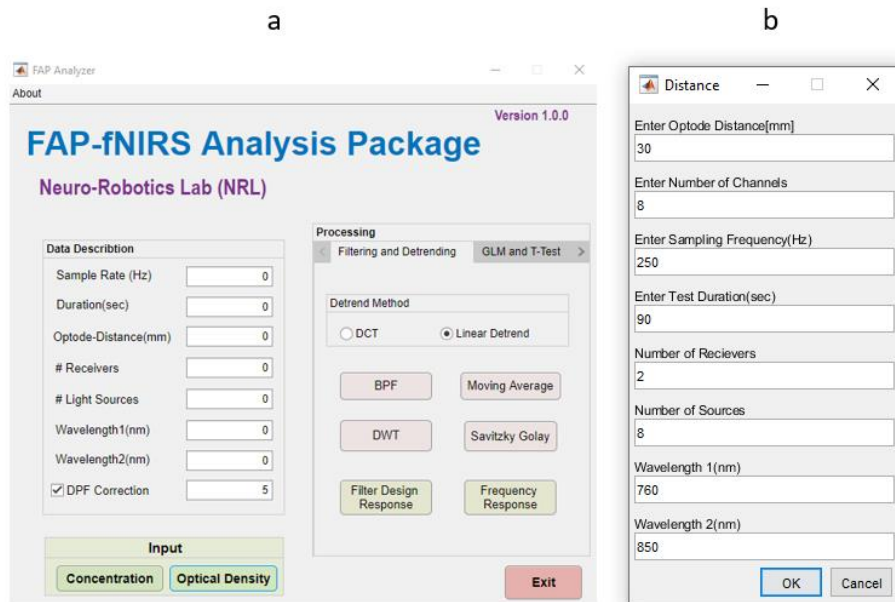


Figure 29. Data conversion interface. The main window showing data input and conversion (a), the required parameters for DPF (b). DPF correction needs to be checked before entering parameters.

DPF Correction: In data conversion, the DPF correction should be checked. This box is used for MBLL to calculate HbO and HbR changes from OD. The proposed GUI accepts subjects from range 20 to 60 to calculate DPF correction. In g.tec/ARTINIS system, the first wavelength (760 nm) used for HbO and the second (850 nm) has used for HbR conversion. The reason for this choice can be explained from optical NIR window shown in Figure 8 (Section 2.3). Using equation

3, the acceptable range of DPF values for HbO and HbR conversion in the proposed GUI can be achieved as:

$$DPF(A = 20: 60, \lambda = 760,850 \text{ nm}) = 223.3 + 0.05624A^{0.8493} - 5.723 \times 10^{-7} \lambda^3 + 0.001245 \lambda^2 - 0.9025 \lambda \quad (10)$$

By solving the above equation in boundary conditions, the DPF range will be chosen in the range of 5 to 6.

3.5 Signal Processing

Signal processing is the first stage in fNIRS analysis. The designed GUI has provided the most common signal and data analysis used for fNIRS and it helps to explore how applying multiple signal processing algorithms lead to better results. The algorithms for motion artifact removal have been recognized as: linear detrend, DCT and DWT. Physiological and instrumentation noise has been reduced using Savitzky-Golay, BPF and Moving Average filters. Each of these de-trending and filtering methods use a different signal processing algorithm that they will be discussed in the following.

3.5.1 Detrending

Detrending is a useful technique to normalize data before filtering. In this project, linear detrend, DCT and DWT have been used to detrend motion artifact from the data. To eliminate DC offset or trend from the data signal, detrending algorithms have been used in the proposed GUI. Generally, to eliminate artifacts from fNIRS data the below procedure is used:

1. import the raw data in form of Concentration changes [HbO, HbR]
2. Apply appropriate detrending algorithm on the data

3. Apply Common Average Reference (CAR) (to eliminate motion factors)

The important point while detrending is that the sampling frequency should be the actual frequency as the system since motion artifacts occur in those frequencies. Sampling rate in g.tec/ARTINIS devices is 10 Hz.

3.5.1.1 Linear Detrend

Linear Detrending (LD) known as the easiest and fastest way to detrend fNIRS signal. According to math work, it tends to compute the least-squares fit of a straight-line from vector x and returns it in y (Equation 11). If x is a matrix, detrend removes the trend from each column. In LD method the algorithm shown in Figure 30 has been applied.

$$y = \text{detrend}(x) \tag{11} [86]$$

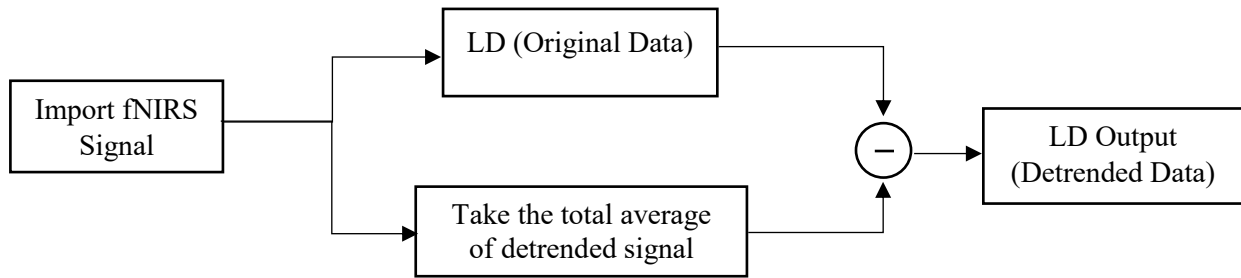


Figure 30. Block diagram for LD detrending method.

3.5.1.2 DCT Detrend

The discrete cosine transforms (DCT) represents a signal as a sum of sinusoids of varying magnitudes and frequencies. The DCT has the property that, for a typical fNIRS signal, most of the significant information about the signal is concentrated in just a few coefficients of the DCT. For this reason, the DCT is often known to compress the signal. To measure energy of signal DCT shows a better response. The Equation 12 represents DCT-1D algorithm.

$$y(k) = \sqrt{\frac{2}{N-1} \sum_{n=1}^N x(n) \frac{1}{\sqrt{1 + \delta_{n1} + \delta_{nN}}} \frac{1}{\sqrt{1 + \delta_{k1} + \delta_{kN}}} \cos\left(\frac{\pi}{N-1} (n-1)(k-1)\right)} \quad (12) [86]$$

Where x refers to the original signal, N is the length of signal vector, and $\delta_{k\ell}$ is the Kronecker delta in length of the signal. DCT is available in MATLAB as a function.

3.5.1.2 DWT Detrend

Wavelet-based analysis tends to decompose signal into its original components. In other words, this transform decomposes the signal into mutually orthogonal set of wavelets. The most known family of orthonormal wavelets is the family of Daubechies. Other wavelet families are shown in Table 4. The wavelet can be constructed from a scaling function which describes its scaling properties. The restriction that the scaling functions must be orthogonal to its discrete translations implies some mathematical conditions on them which are mentioned in the dilation equation:

$$\varphi(x) = \sum_{k=-\infty}^{+\infty} a_k(\varphi)(Sx - k) \quad (13) [87]$$

Where a_k the number of nonzero coefficients and S is a scaling factor (usually chosen as 2).

TABLE 4

WAVELET-BASED FUNCTIONS IN MATLAB

Wavelet Family Short Name in MATLAB	Wavelet Family Name
'db'	Daubechies wavelets
'sym'	Symlets
'coif'	Coiflets
'haar'	Haar wavelet

TABLE 4 (continued)

'mori'	Morlet wavelet
'meyr'	Meyer wavelet
'gaus'	Gaussian wavelets

As it has shown in Figure 31, the original fNIRS signal (Top Left) contained lots of motion artifact which made some degree of distortion in baseline and DC offset. All detrending algorithms can successfully shift the baseline and correct the DC offset on the signal. DCT-based detrending compress signal (decreasing period). In wavelet-based detrending, we used Symlets which is shown as 'sym' in MATLAB (Table 3). The number of vanishing moments (N) set to 10 levels in this example.

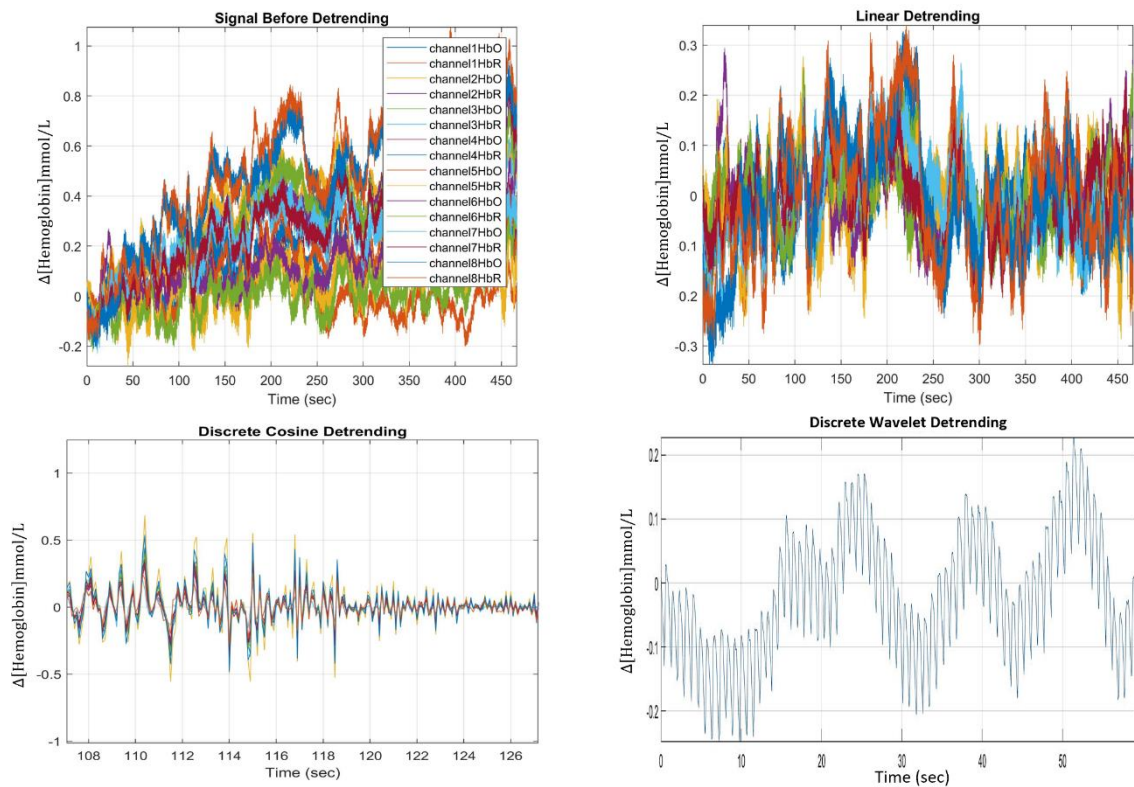


Figure 31. Detrending methods on the typical fNIRS data. Baseline and DC offset have corrected in all cases.

3.5.2 Filtering

After motion correction, the designed GUI filtered the data individually with three different filters to test performance of each. Physiological noises can be mitigated by choosing among three possible options: 1) BPF, 2) Moving Average, and 3) S-G filter. The performance of each of these filters depend on the experiment design and the region of interest to remove noise. In this section the method to design these filters and the governing equations used in the GUI have been discussed.

3.5.2.1 BPF

In the proposed GUI, band pass filtering (BPF) has applied to attenuate both low and high frequencies. BPF is a kind of FIR (Finite Impulse Response) filters. The filter passes through frequencies inside the bandwidth but attenuates (reduces the amplitude of) frequencies outside the bandwidth. The low cut-off frequency (Lo. Freq.) and the high cut-off frequency (Hi. Freq) specify the bandwidth. The high cut-off frequency must be larger than the low cut-off frequency. The frequencies between these cut-off frequencies pass through. Actually, band pass filtering is a combination of low and high pass filtering. BPF filter designs need a certain number of samples for good characteristics, and this may result in "lack of data points" in the beginning and end of the trace result. Figure 32-a displays atypical BPF filter response. The attenuation is 30 dB, the band-pass ripples are 1 dB and the transition bands are $\text{Lo Freq}/4 \text{ Hz}$ and $\text{Hi Freq}/4 \text{ Hz}$. Notice that the cutoff frequency is limited to $1/100$ of the sample rate. Figure 32-b is shown the BPF characteristic in the designed GUI. Low and High cutoff frequencies have set to 0.01 and 0.6 respectively as a default.

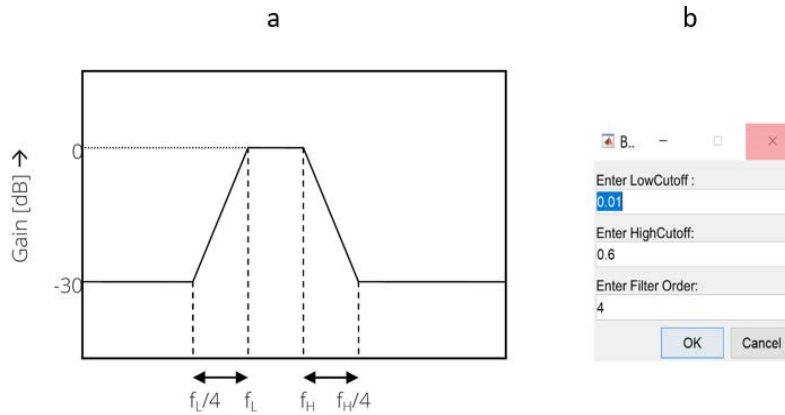


Figure 32. BPF characteristic. A typical BPF response the attenuation is 30dB, the band-pass ripple is 1 dB, the low transition band is $f_L/4$ Hz and the high transition band is $f_H/4$ Hz (Left), BPF characteristic in the proposed GUI (Right).

By increasing filter order, the signal will be smoother since the filter performs like an ideal box car function. In real world, too much increasing filter order ends up overfitting in the result.

3.5.2.2 Moving Average

A moving average filter is a generic smoothing filter to reduce high frequency noise. The filter width n must be specified in seconds. The moving average filter calculates the unweighted mean of the measured data over the filter width from sample $i-n/2$ to sample $i+n/2$ (Figure 33-a). As a result, the first $n/2$ and last $n/2$ seconds of data are lacking. If the interest is the behavior of the HbO over time, to reduce the pulse and the high frequency noise at once, the moving average filter with a filter width of 20 seconds has been used (Figure 33-b).

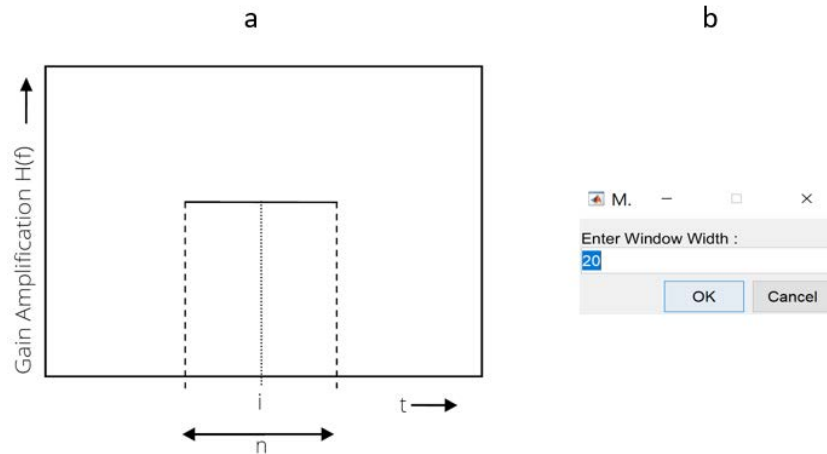


Figure 33. Moving average filter design: Left) with filter width (n) over time (t), Right) the default value for window width in the proposed GUI.

3.5.2.3 Savitzky-Golay (S-G)

As discussed in section 2.5.3, S-G is a finite impulse response (FIR) smoothing filter aims at reducing noise from fNIRS signal by preserving its high frequency components. S-G can reduce spikes from HbO and HbR responses. We used $n=31$ ($2n+1=63$ neighboring points for averaging) and frame length 101 sec (Figure 34) for S-G default parameters (note that our data were sampled at a rate of 10 samples/s). The parameter $2n+1$ should be less than the length of HRF; otherwise, it can smooth out the HRF itself. Finding the best parameters for S-G filter needs visualizing signal and change update a polynomial degree (n) and frame length which fit better on the signal.

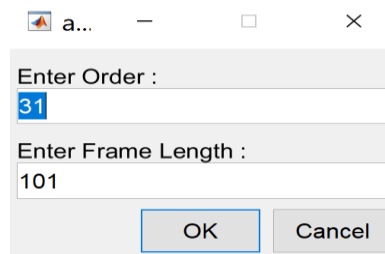


Figure 34. Default parameters for S-G filtering based on the literature in the designed GUI.

3.5.3 Signal Quality

When the signal quality of the data is poor, motion detection algorithms fail to find the motion artifacts and thus results in new baseline shifts. To avoid this problem, the proposed GUI first calculated the SNR of the motion-free part of the signal and then applied a predefined threshold (SNR=3) on the SNR. We have chosen this threshold as we were able to extract the heartbeat variation in the signal when the SNR of the signal was higher than 3. While the signals with high SNR (SNR>3) are detected the user can decide whether to continue processing or improve signal strength. The below equation has used to calculate SNR:

$$SNR(dB) = 10 \log_{10} \frac{power(signal)}{var(noise)} \quad (14)$$

The designed GUI can show SNR for each filtered signal and the user can compare all methods in term of signal quality and re-design the data collection or system setup if the SNR is low.

3.6 Data Analysis

The data processed from the previous steps will be used in analysis step to purify fNIRS signal from possible useless data or noise values. In the proposed GUI, the data were analyzed in a user defined MATLAB script. The GUI is capable to analyze HbO, HbR and total hemoglobin signal separately and apply GLM model to find the best parameters fit on each signal. In this section the detail information of data analysis stage used in the GUI will be discussed.

3.6.1 Experiment Procedure and Paradigm

In this thesis, the finger tapping task and motor imagery site of the brain were chosen to design the experiment and paradigm. Four healthy subjects participated in the experiments. Their average age was 23.5 years with a standard deviation of 7 years. Each subject was asked about

his/her medical history, and it was determined that none had had any neuronal disorder. A written consent attesting to his/her willingness to participate in the experiment was signed by each subject. The experiment was conducted in accordance with IRB # 4513, Wichita State University. As it is standard good practice, all the subjects were informed of the experimental details for the best possible results. They were advised to remain calm while sitting on a comfortable seat, to avoid artifacts and noise. In the collected dataset we used 10 trials, each lasted for 9 sec in multiple finger tapping periods (Figure 35-a). Task design has performed in the GUI as shown in Figure 35-b.

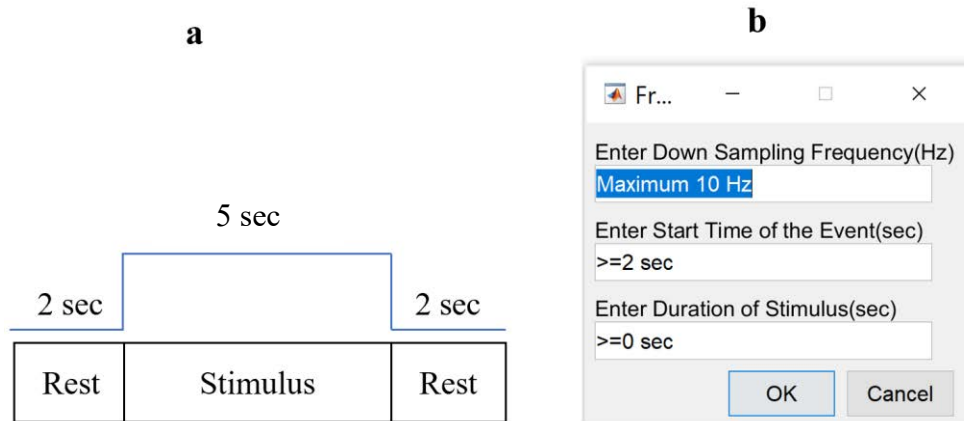


Figure 35. Experiment procedure and paradigm. a) One trial of finger tapping used in the proposed GUI for data analysis, b) task design window in the design GUI.

3.6.2 General Linear Model

In data analysis step, the General Linear Model (GLM) model has been adapted to fNIRS data. The GLM describes data as a linear combination of an explanatory variable and an error term as it is shown in Equation 15.

$$Y(k) = X * \beta(k) + \varepsilon(k) \quad (15) [88]$$

Where Y is the vector of observed fNIRS signal during recording period k , X indicates the design/contrast matrix, β is the corresponding response signal strength for either HbO or HbR parameters (regression coefficient) and ε denotes the error between the observed and the designed responses. The parameters defined in Equation 15 based on 9 sec task duration for each trial are:

$$Y(k) = \begin{pmatrix} y(k)_1 \\ \cdot \\ \cdot \\ \cdot \\ y(k)_9 \end{pmatrix}, \quad X = \begin{pmatrix} 1 & \text{rest}_1 & \text{task}_1 \\ \cdot & \cdot & \cdot \\ \cdot & \cdot & \cdot \\ \cdot & \cdot & \cdot \\ 1 & \text{rest}_9 & \text{task}_9 \end{pmatrix}, \quad \beta(k) = \begin{pmatrix} \beta(k)_0 \\ \beta(k)_{\text{rest}} \\ \beta(k)_{\text{task}} \end{pmatrix}, \quad \varepsilon(k) = \begin{pmatrix} \varepsilon(k)_1 \\ \cdot \\ \cdot \\ \cdot \\ \varepsilon(k)_9 \end{pmatrix} \quad (16) [88]$$

A block diagram of contrast/design matrix h is shown in Figure 36. By simplifying the equation 15, the least square estimation of β is calculated as the following linear regression model:

$$\beta = X^* \cdot Y \quad (17)[88]$$

Where X^* is the pseudo-inverse matrix of h and given by $X^* = (X^T X)^{-1} X^T$. The regression coefficient β and the residual error ε are tested with the one-sample t-test.

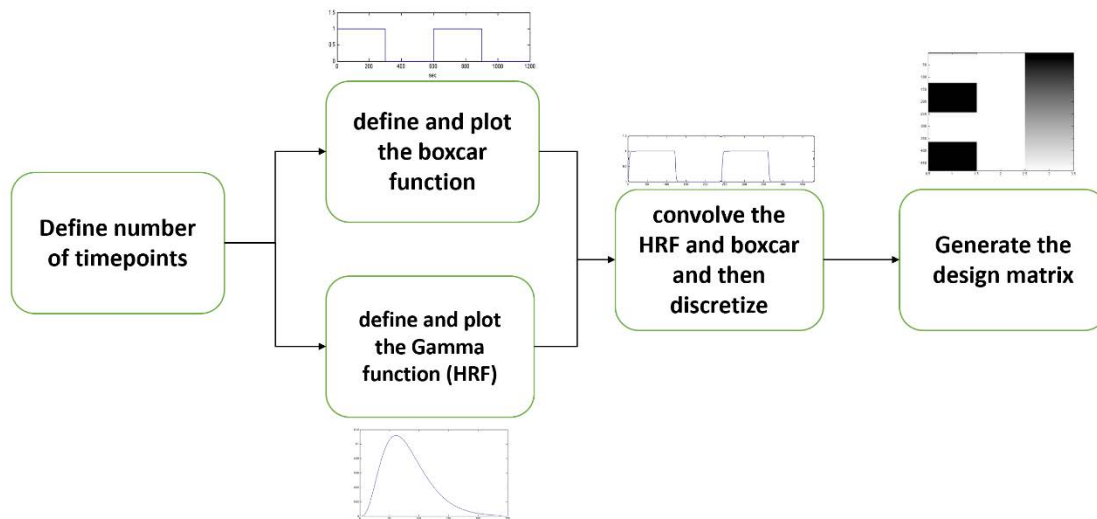


Figure 36. Reconstructing X matrix in GLM model for hemodynamic response.

Figure 37 has shown the predicted the blood oxygen level dependent (BOLD) response for a typical signal using GLM model.

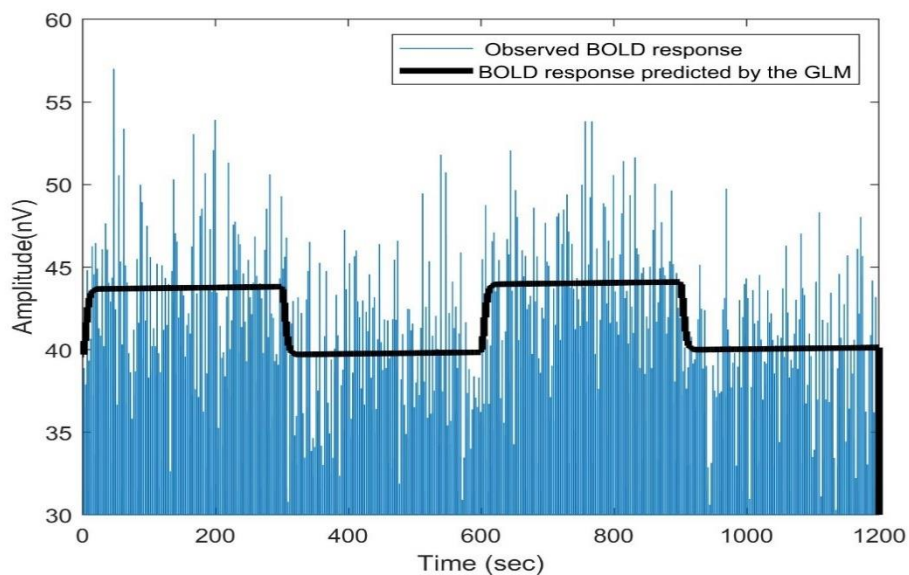


Figure 37. Applying GLM model on a typical data.

3.6.3 Statistical Test

T-Test: From the last section, the outcome of GLM regressor model is parameters of a line which fits on data the best. After this step, the first level (individual subject) or second level (group channels) analysis was performed using t-values calculations to decide whether to reject or accept stochastic data peripheral to the regressor. The t-values are calculated by:

$$t - value = \frac{c^T \beta}{\sqrt{\varepsilon^2 c^T (X^T X)^{-1} c}} \text{ or } \frac{Mean1 - Mean2}{\sqrt{\frac{st1^2}{N1} + \frac{st2^2}{N2}}} \quad (18) [88]$$

Where c is the contrast vector ($[1;0;0]$ in this study), which determines the array elements of the regression coefficient β for contrast matrix X . ε^2 refers to error variance which indicates how much random fluctuation is expected within the estimated response. In all collected dataset, instead of using all the 90 sec for a single linear regression model, we divided the time series of each channel in 10 sub-intervals (i.e. repetitions or trials) lasting 9 sec (made of 2 sec rest, 5 sec task, and 2 sec rest). A linear regression model has individually applied to each repetition and the GUI released t statistical results for each data. To test the hypothesis, the P-value set to 0.05 in every dataset. Alternatively, t-values can be calculated using mean and standard deviation for pair of group/channel (second- level analysis) and knowing the number of trials (N) during the experiment.

P-Value: Student's t cumulative distribution function (cdf) has used in the GUI to calculate p-values. To compute Student's t cdf for each dataset for total number of samples n , the below Equation has used:

$$tcdf(t_stat, n-1) = F(t\text{-value}|n-1) = \int_{-\infty}^{t\text{-value}} \frac{\Gamma(\frac{n}{2})}{\Gamma(\frac{n-1}{2})} \frac{1}{\sqrt{(n-1)\pi}} \frac{1}{(1+\frac{t^2}{n-1})^{\frac{n}{2}}} dt \quad (19) [88]$$

Where F is the probability that a single observation from the t distribution with n-1 degrees of freedom will fall in the interval $(-\infty, t\text{-value}]$.

$$p_value = 1 - tcdf(t_stat, n-1) \quad (20)$$

By calculating p-value, null hypothesis can be checked to see whether each dataset is statistically significant or not. Indeed, if the calculated p-value is lower than the expected p-value, the null hypothesis will be rejected, and the individual data is meaningful for further processing.

3.7 MATLAB SIMULINK

All signal processing and data analysis steps discussed in the previous sections can be modeled in SIMULINK environment. The designed GUI has provided this option to perform signal and data analysis in real time by linking from offline to online mode (Figure 38). The SIMULINK model has created based on the specified experiment for finger tapping (Section 3.6.1). To build contrast matrix X, the method discussed in section 3.6.2 has followed and multiple user defined functions are used to link them in the SIMULINK. The sampling time has set to 0.1 sec as the actual frequency of data collection device was 10 Hz. Figure 39 shows the entire SIMULINK model for online mode in the proposed GUI.

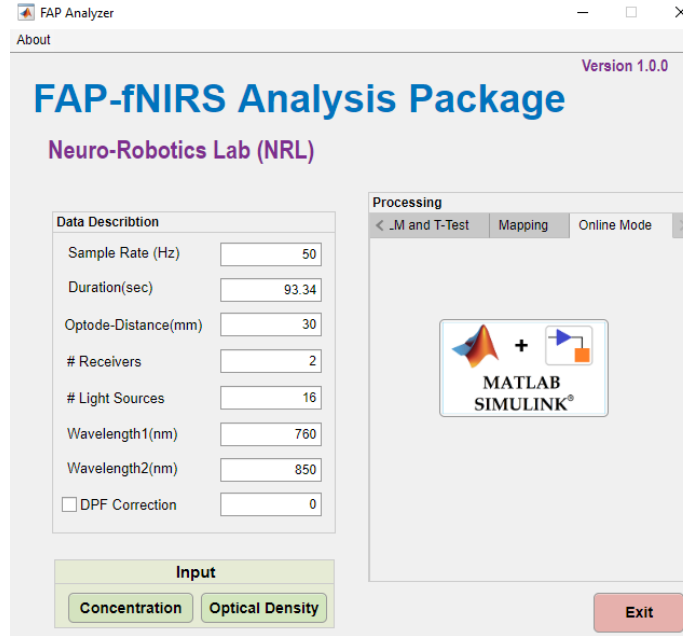


Figure 38. Online mode processing in the proposed GUI.

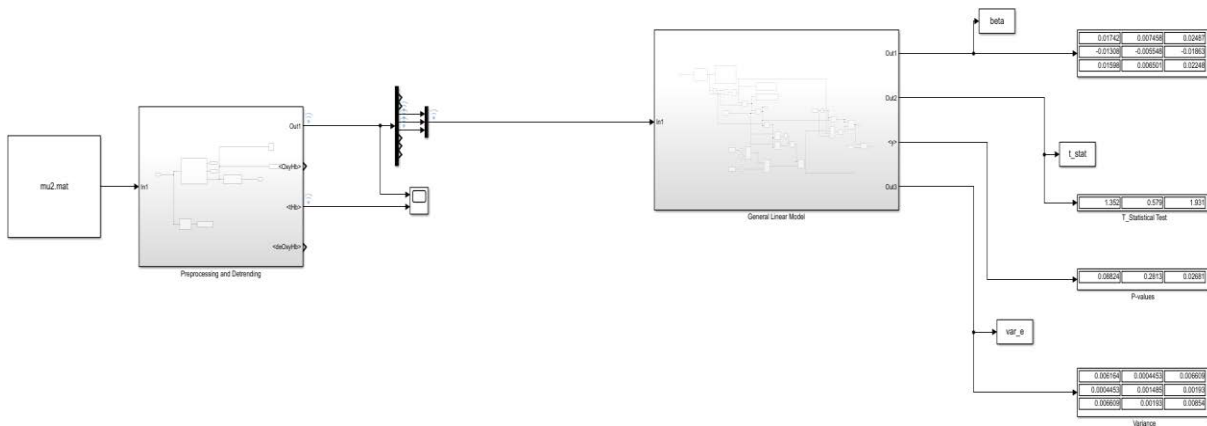


Figure 39. SIMULINK model for the signal processing and data analysis based on the experiment design in this thesis. The Simulink model has shown in figure 39 can perform signal processing and data analysis in real-time. For some application such as online data collection using ARTINIS system, the user might need to link the processing part to the data acquisition device. The signal processing subsystem is included detrending, filtering and SNR blocks and data analysis subsystem is included GLM and t-test blocks.

CHAPTER 4

RESULTS

4.1 Signal Processing and Detrending

4.1.1 Time-Domain

The results of signal processing and detrending on four participants [three males, age of 22, 24, 28 and, one female, age of 19] collected from two different fNIRS systems (ARTINIS and the developed prototype). The data collection has done under IRB # 4513, Wichita State University. All subjects were right-handed, and they were asked to do finger tapping experiment. The detrending method has done using linear detrending and DCT. For each method, the filtered signal has plotted, and the corresponded SNR value has calculated. Figure 40 shows all these steps. Firstly, the linear detrending method has applied on data collected from the first subject (28 years old right-handed male, 4-channel fNIRS developed in the lab) to correct base line and remove motion artifact. As it has shown in Figure 40, BPF order 4, with 0.01 and 0.6 cutoff frequency has a better SNR value (0.11 dB) but it is still lower than our threshold which is 3 dB. Figure 41 has also shown the detrending and filtering results with DCT detrending for subject #1. The results have shown that for subject #1, BPF has a better SNR (6.99 dB) when signal has detrended using DCT method.

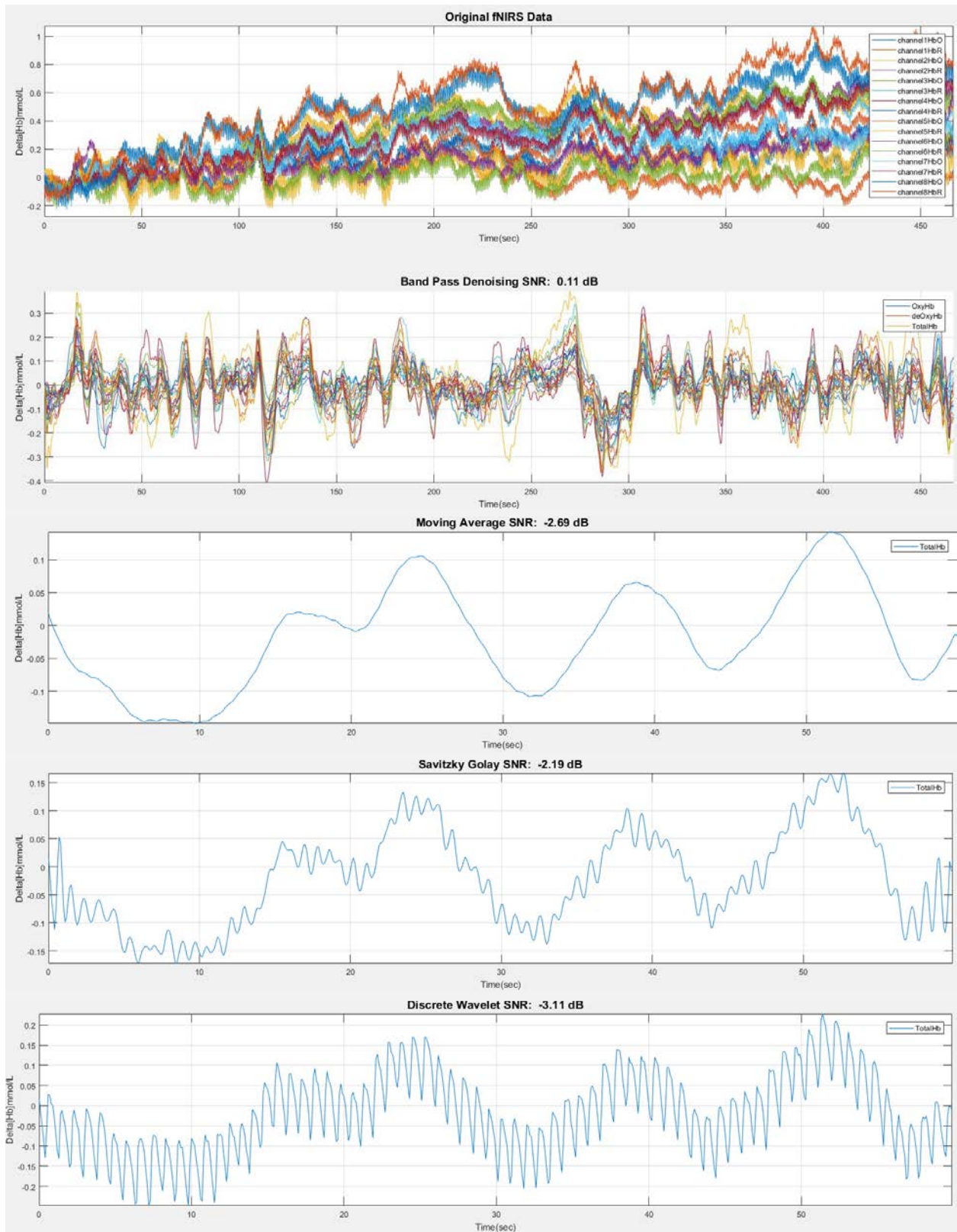


Figure 40. Linear detrending results for subject #1. Data has motion corrected and the SNR value for each filtered signal has extracted.

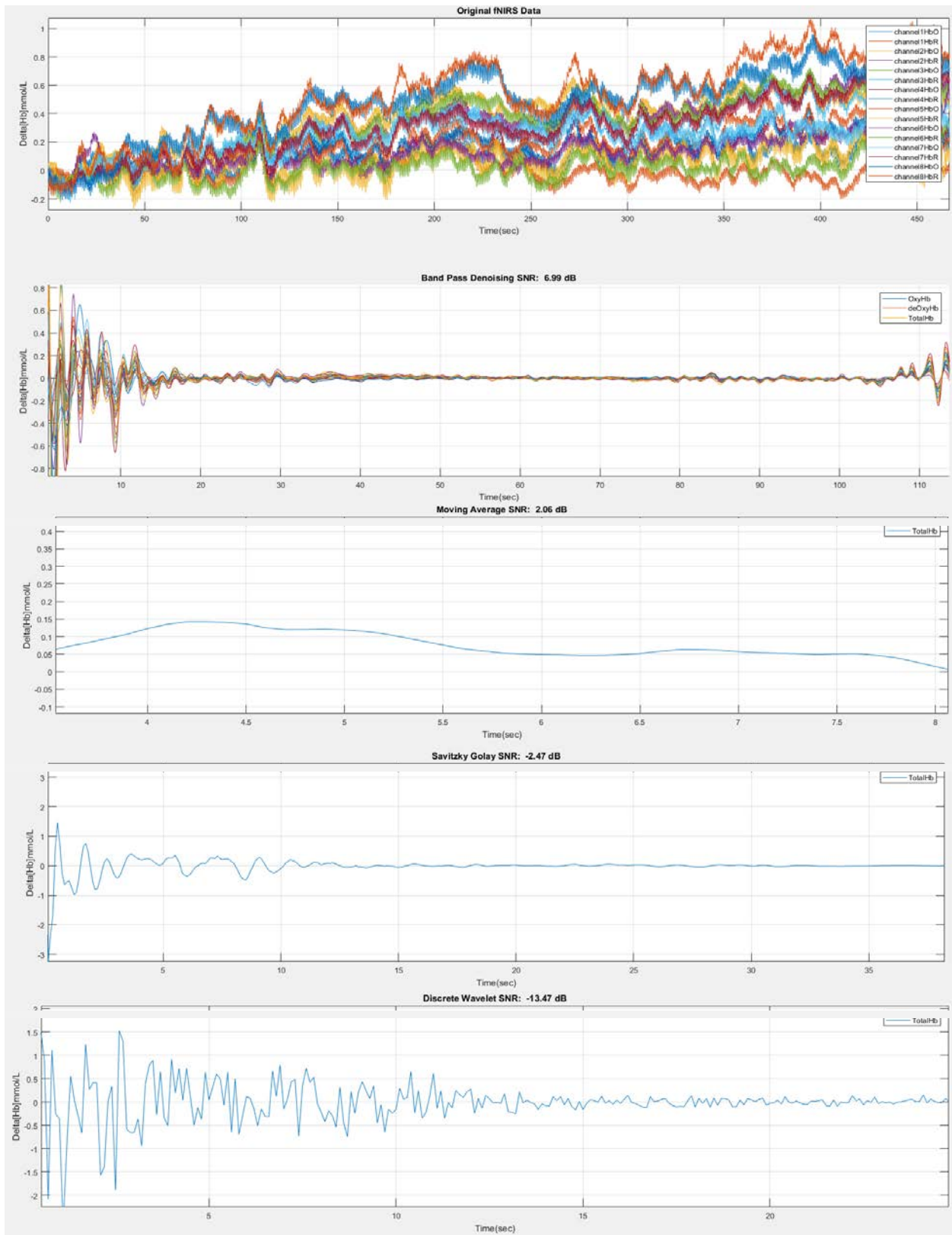


Figure 41. DCT detrending results for subject #1. Data has motion corrected and the SNR value for each filtered signal has extracted.

The SNR value for all subjects with linear and DCT detrending has shown in Table 5. As it has shown in Table 5, for subject #2 (22 years old, right-handed male), DCT detrending along with BPF filtering end up with SNR = 4.8 dB which is better than the predefined threshold (3 dB). Conversely, the worst SNR (-10.79 dB) has calculated when the signal has detrended using DCT and Savitzky-Golay filtering has applied on the data. Subject #3 (24 years old, right-handed male) and subject #4 (19 years old, right-handed female) have not produced an acceptable SNR more than 3 dB. Furthermore, subject 1 and 2 with DCT detrending will be fed into the data analysis step.

TABLE 5.

Results of detrending and signal processing for all subjects in this study.

Filtering Method	Calculated SNR Value (dB)							
	Subject #1		Subject #2		Subject #3		Subject #4	
	Linear Detrend	DCT	Linear Detrend	DCT	Linear Detrend	DCT	Linear Detrend	DCT
BPF (0.01-0.6 Hz cutoff freq.)	0.11	6.99	0.08	4.8	-1.58	-0.5	-1.72	0.04
Moving Average (20sec)	-2.69	2.06	-3.76	2.72	-5.55	-4.36	-5.73	-2.77
Savitzky-Golay (order 31, 101 sec window length)	-2.19	-2.47	-3.85	-10.79	-28.45	-17.92	-27.69	-9.68
DWT (sym8*)	-3.11	-13.47	-0.78	-6.75	-4.7	-3.33	-5.37	-4.03

*sym8= Symlets Wavelet with 8 levels vanishing moments

4.1.2 Frequency Response

In this thesis, the designed GUI has been able to show the frequency response as well as the Time-domain responses as shown in section 4.1.1. Frequency responses have included filter design and Fast Fourier Transform (FFT) on the desired signal for each subject. FFT of each channel can be used either to decide if signal quality for each channel (8-channels in ARTINIS) is acceptable or if activity of the desired channel in frequency domain is sufficient. Figures 42-45 have shown FFT graphs for all four-subjects in the study. Furthermore, FFT graphs tend to indicate signal quality by focusing on each individual channel. So, the user might change data collection methodology if any of the channels do not transmit/receive a proper signal. Figure 42 shows that for subject #1, almost all channels have a good activity. SNR value in Table 5 has already approved this fact.

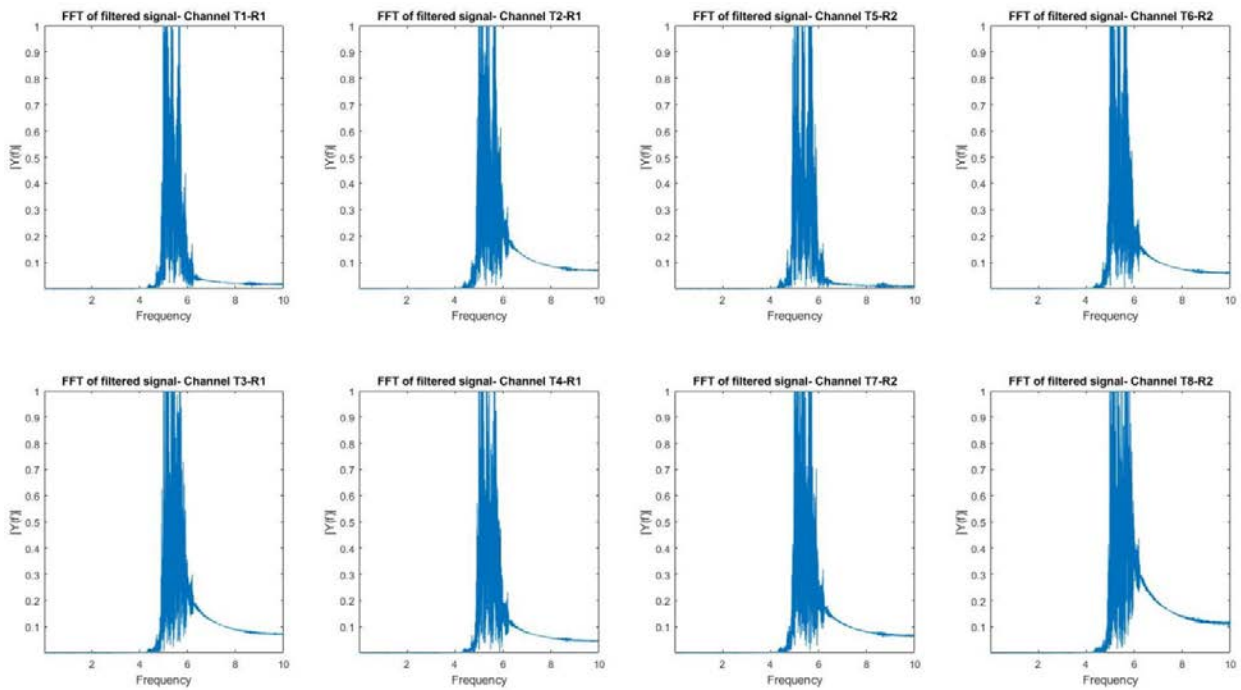


Figure 42. FFT results for subject #1. Transmitters labeled as T1-T8 and R1- R2 refers to receivers.

Figure 43 has shown the frequency responses for subject #2. The FFT plots are pretty similar to the first subject. This can be explained in Table 5 as SNR value for subject #1&2, when DCT detrending has used, reported higher than the 3 dB threshold. In other side, SNR values for both

subject #3&4 were not reported higher than threshold (3 dB) so we expect not to get a good FFT result for these two subjects. Figures 44 and 45 have proven this fact. Referring to the Table 5, none of the utilized filtering methods (BPF, moving average, S-G and DWT) ended up with an acceptable SNR for two last subjects neither with linear nor DCT detrending.

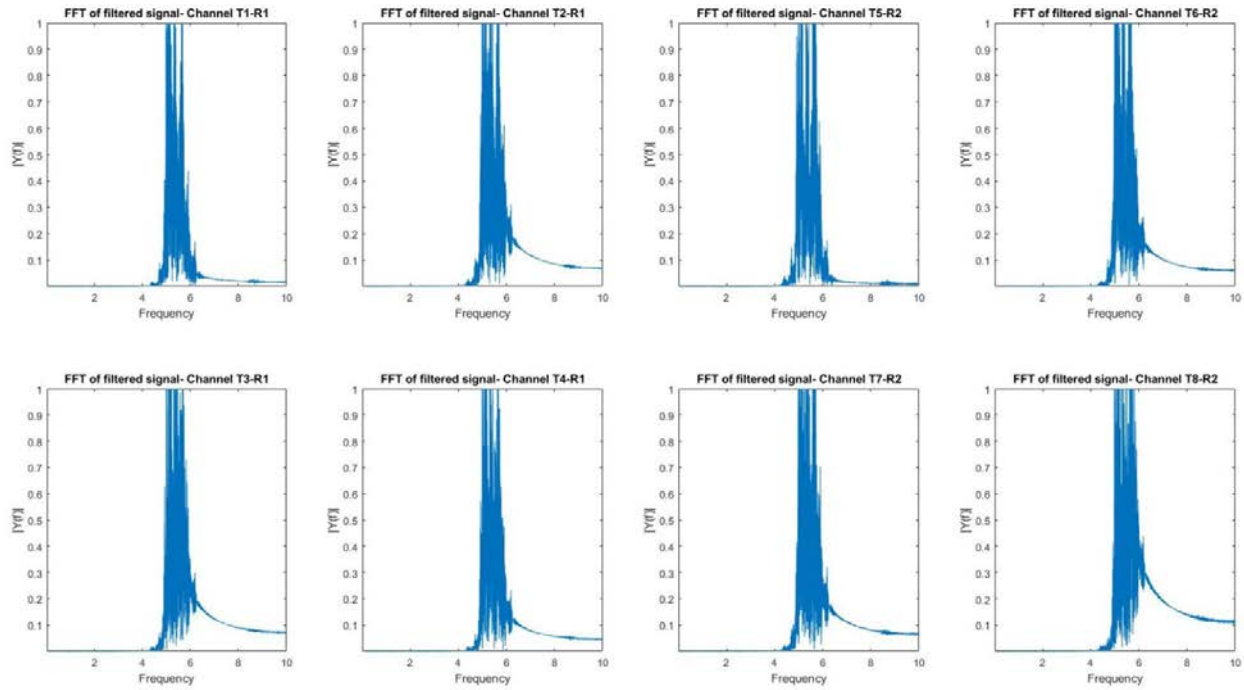


Figure 43. FFT results for subject #2.

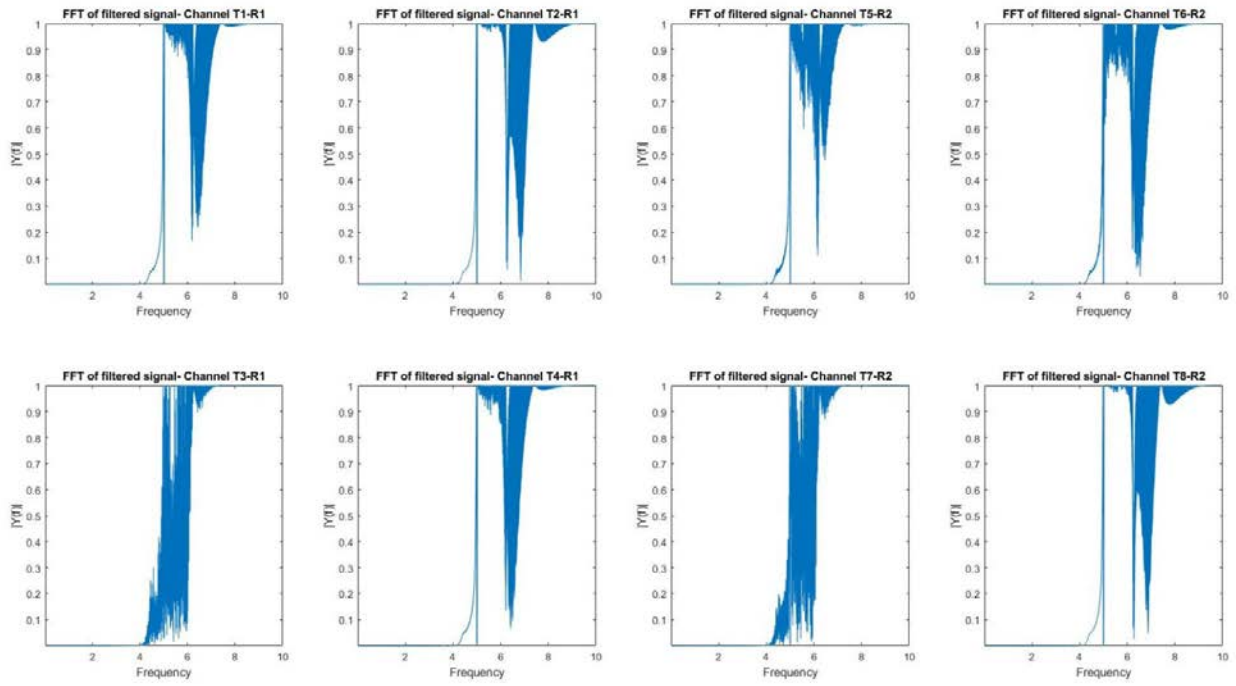


Figure 44. FFT results for subject #3.

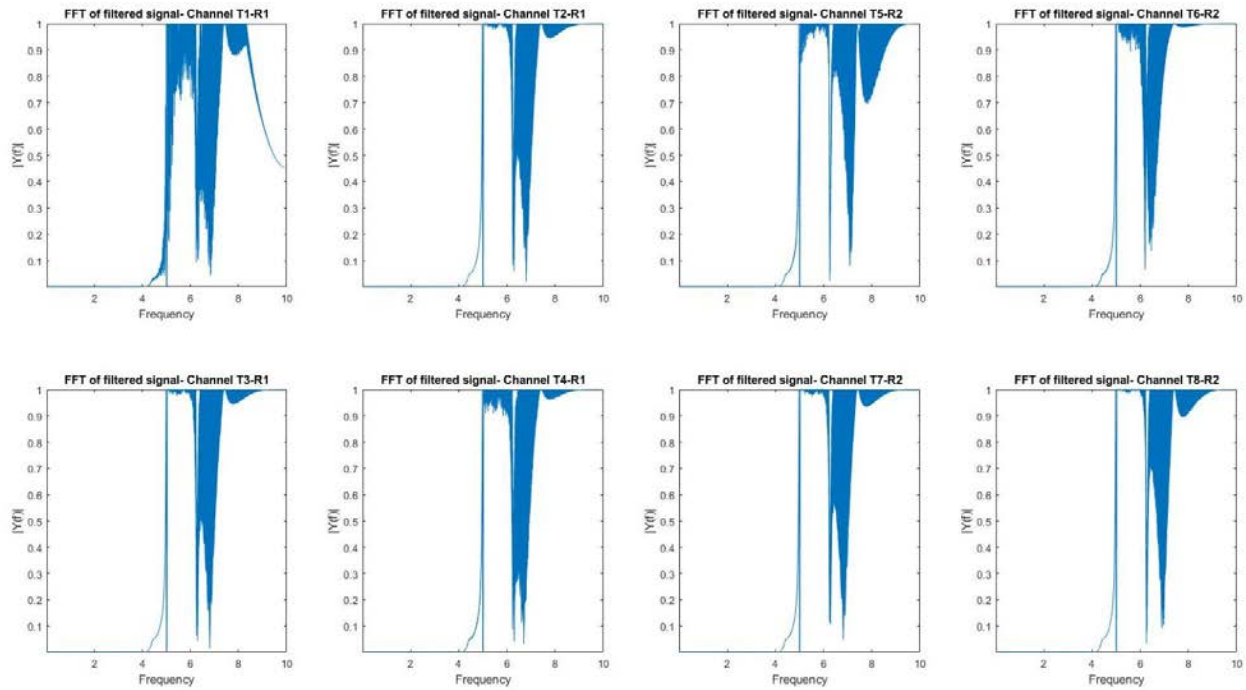


Figure 45. FFT results for subject #4.

The filter design's result has shown in Figure 46. As showed before in detail (Section 3.5.2), fNIRS signal can be filtered using a BPF filter with cutoff frequencies of 0.01 and 0.6 Hz. In this graph, the normalized frequency calculated as cutoff frequency divided by Nyquist frequency. Filter has order 4 with passband ripple and stopband attenuation of 0.5 and 50 dB, respectively.

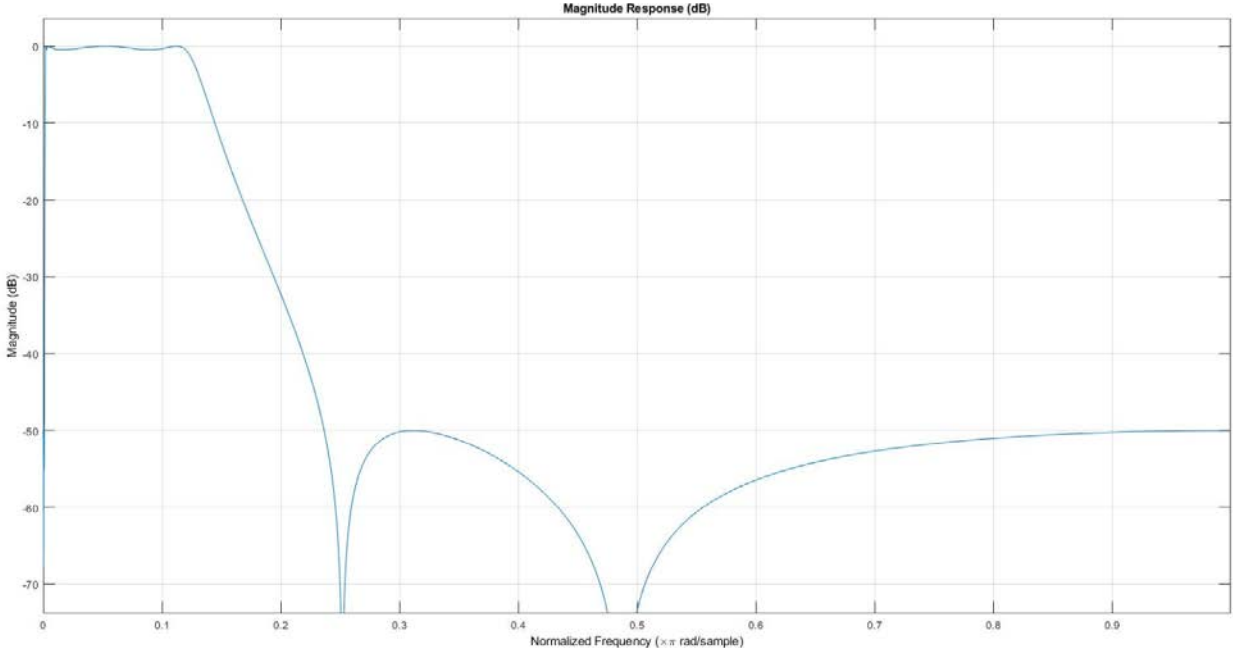


Figure 46. Filter design response. 4th order elliptic filter has used.

4.2 Data Analysis and Estimation

Data analysis's steps has discussed in section 3.6. The results of GLM model estimation, the regression coefficients (Beta) and t-statistical test values have shown in this section. Based on the experiment design for each trial (2 sec rest, 5 sec finger tapping imagination, 2 sec rest), the required parameters have set in the GUI and the results of hemodynamic response modeling

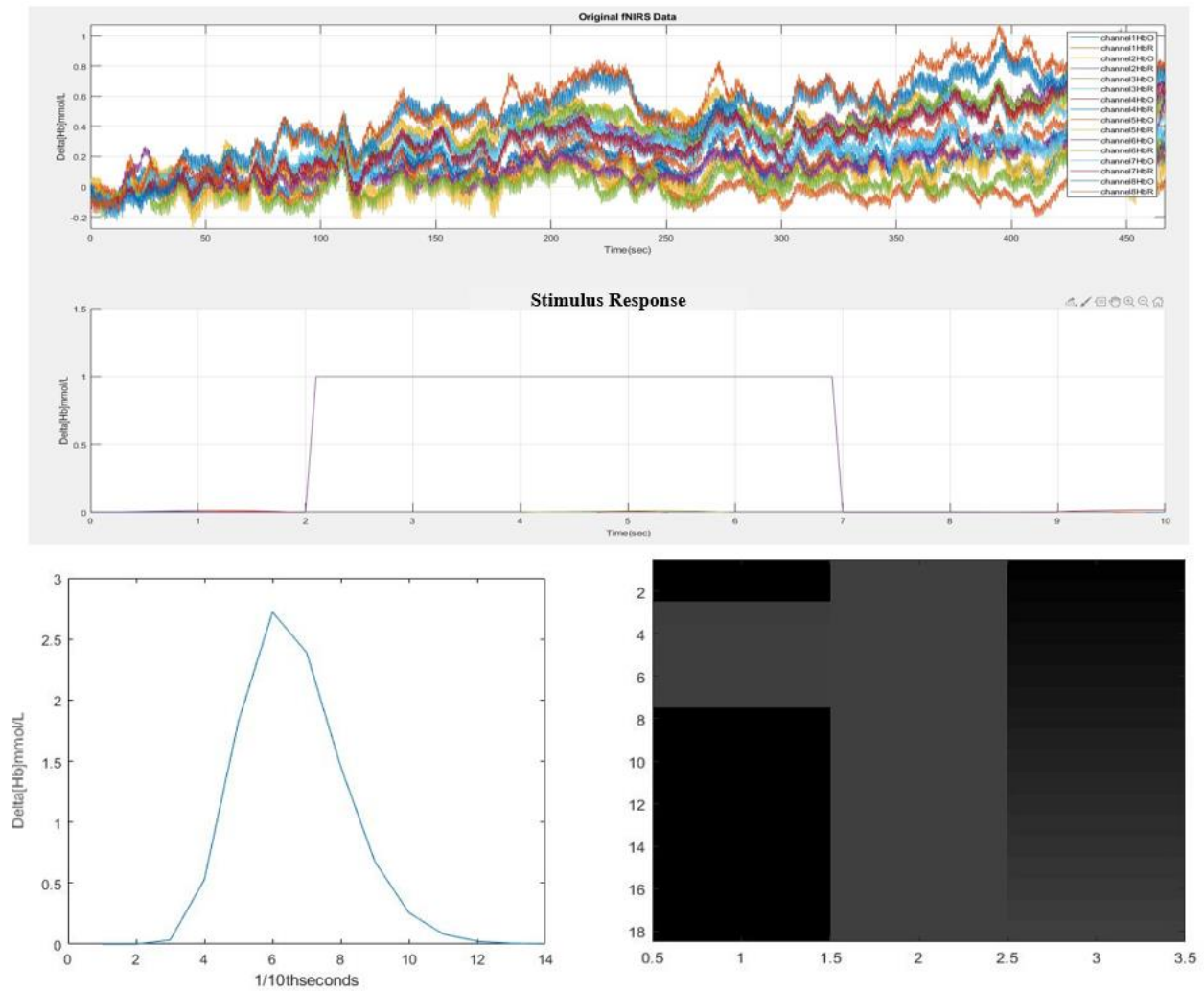


Figure 47. Data Analysis and Estimation of subject #1. The stimulus response design (Top), hemodynamic response estimation (Bottom Left) and contrast matrix (Bottom Right).

β -values were estimated through the least square estimation for left and right finger tapping. For each dataset, the Analysis of Variance (ANOVA) test has applied to see if the contrast matrix values are designed correctly. Table 6 has shown the ANOVA test on all subjects. Based on the general linear hypothesis H_0 :

$$H_0 : L \beta = m; [1 \ 1 \ -1] = \begin{bmatrix} \beta_1 \\ \beta_2 \\ \beta_3 \end{bmatrix} = 0 \quad (21) [88]$$

$$H_0 : (\beta_1 + \beta_2) - \beta_3 = 0 \quad (22) [88]$$

Where L is the matrix of weights, β is the vector of regression coefficients and m is the vector of proposed values. Equation 21 and 22 have fulfilled ANOVA test for all subjects as it has shown in Table 6- 13. In this Table, β_1 corresponds for HbO, β_2 for HbR and β_3 for total Hb.

TABLE 6.

ANOVA test results for channel T1-R1 of all subjects.

Subject #1			Subject #2			Subject #3			Subject #4		
β_1	β_2	β_3	β_1	β_2	β_3	β_1	β_2	β_3	β_1	β_2	β_3
0.0614	0.0253	0.0867	- 1.1e+0 3	- 838.47	- 1.9e+0 3	407.41	- 1.2e+0 3	- 837.34	529.44	-843.6	-314.1
- 0.0290	- 0.0161	- 0.0451	658.59	482.03	1.14e+ 03	-527.4	1.6e+0 3	1.1e+0 3	- 681.55	1.35e+ 03	670.12
0.0109	0.0180	0.0289	- 508.95	- 383.35	- 892.30	1.01e+ 03	- 3.16e+ 03	- 2.14e+ 03	1.3e+0 3	- 2.88e+ 03	- 1.57e+ 03

TABLE 7.

ANOVA test results for channel T2-R1 of all subjects.

Subject #1			Subject #2			Subject #3			Subject #4		
β_1	β_2	β_3									
0.1287	0.0212	0.1499	- 1.1e+3	- 1.4e+3	- 2.6e+3	- 1.5e+3	- 1.2e+3	- 2.7e+3	1.1e+3	1.5e+3	2.6e+3
- 0.0978	- 0.0133	- 0.1111	557.77	597.96	1.2e+3	1.9e+3	1.5e+3	3.4e+3	- 1.4e+3	- 1.9e+3	- 3.3e+3
0.1281	0.0189	0.1470	- 443.14	- 462.70	- 905.84	- 3.7e+3	- 2.9e+3	- 6.6e+3	2.6e+3	3.8e+3	6.4e+3

TABLE 8.

ANOVA test results for channel T3-R1 of all subjects.

Subject #1			Subject #2			Subject #3			Subject #4		
β_1	β_2	β_3	β_1	β_2	β_3	β_1	β_2	β_3	β_1	β_2	β_3
0.0793	0.0898	0.1783	- 843.36	- 1.2e+3	- 2.4e+3	-496.1	491.8	-4.3	344.95	1.9e+3	2.2e+3
- 0.0484	- 0.0723	- 0.1207	477.59	684.93	1.1e+3	643.45	-637.8	5.6	-444.4	- 2.4e+3	- 2.8e+3
0.0447	0.0888	0.1335	-358.9	- 526.27	- 885.18	- 1.2e+3	1.2e+3	0	852.7	4.6e+3	5.5e+3

TABLE 9.

ANOVA test results for channel T4-R1 of all subjects.

Subject #1			Subject #2			Subject #3			Subject #4		
β_1	β_2	β_3	β_1	β_2	β_3	β_1	β_2	β_3	β_1	β_2	β_3
0.0516	0.0557	0.1073	- 992.86	- 1.3e+3	- 2.3e+3	323.5	- 1.1e+3	-786.6	541.9	150.5	692.4

TABLE 8 (continued)

-	-	-	565.37	763.14	1.33e+3	-	1.4e+3	1.1e+3	-696	-	-891.2
0.0316	0.0515	0.0831				420.1				195.2	
0.0321	0.0861	0.1183	-440.8	-578.6	-1.2e+3	808.7	-	-	1.3e+3	376	1.7e+3
							2.75e+3	1.94e+3			

TABLE 10.

ANOVA test results for channel T5-R2 of all subjects.

Subject #1			Subject #2			Subject #3			Subject #4		
β_1	β_2	β_3									
0.088	0.0791	0.1671	-	-	-	-278.9	485.4	206.4	3.5e+3	1.6e+3	5.2e+3
			1.1e+3	1.1e+3	2.2e+3						
-	-	-	650.7	624.3	1.3e+3	358.7	-628.9	-270.2	-	-	-
0.0876	0.0651	0.1527							4.2e+3	2.1e+3	6.3e+3
0.1417	0.0857	0.2274	-495.9	-478.8	-974.7	-678.2	1.2e+3	522.02	7.8e+3	4.1e+3	1.9e+4

TABLE 11.

ANOVA test results for channel T6-R2 of all subjects.

Subject #1			Subject #2			Subject #3			Subject #4		
β_1	β_2	β_3									
0.1143	-	0.1079	-	-	-	649.98	271.56	921.54	367.12	851.72	1.2e+3
	0.0065		1.2e+3	1.1e+3	2.3e+3						
-	0.0126	-	674.5	646.7	1.3e+3	-	-	-	-471	-	-
0.0711		0.0585				816.76	351.77	1.2e+3		1.1e+3	1.6e+3
0.0596	-0.025	0.0346	-519.6	-496.9	-	1.5e+3	676.4	2.2e+3	901.4	2.1e+3	3e+3
					1.1e+3						

TABLE 12.

ANOVA test results for channel T7-R2 of all subjects.

Subject #1			Subject #2			Subject #3			Subject #4		
β_1	β_2	β_3	β_1	β_2	β_3	β_1	β_2	β_3	β_1	β_2	β_3
0.1308	0.0444	0.1752	- 1.2e+3	- 959.54	- 2.1e+3	185.03	-169.5	15.49	2.1e+3	143.5	2.3e+3
- 0.0765	-0.028	- 0.1045	674.4	546.3	1.2e+3	- 239.98	218.17	-21.81	- 2.8e+3	-183.8	- 2.9e+3
0.0686	0.0305	0.0991	-523.7	-421.6	-945.4	461.56	- 418.25	43.32	5.3e+3	351.7	5.6e+3

TABLE 13.

ANOVA test results for channel T8-R2 of all subjects.

Subject #1			Subject #2			Subject #3			Subject #4		
β_1	β_2	β_3	β_1	β_2	β_3	β_1	β_2	β_3	β_1	β_2	β_3
0.059	0.1558	0.2148	- 1.2e+3	-981.8	- 2.2e+3	2.1e+3	948.3	3.1e+3	1.6e+3	1.7e+3	3.3e+3
- 0.0136	-0.089	- 0.1026	678.1	559.2	1.2e+3	- 2.7e+3	- 1.2e+3	- 3.9e+3	- 2.1e+3	- 2.2e+3	- 4.2e+3
- 0.0124	0.0694	0.057	-517.4	-432.4	-949.9	5.3e+3	2.3e+3	7.6e+3	3.9e+3	4.1e+3	8.1e+3

Statistical Test: To statistically validate each individual channel (first-level analysis) or to compare between two groups of channels (second-level analysis), statistical test has performed. Data similarities between channels are compared using p-value (0.05 default). Based on null hypothesis, for calculated means and standard deviation of two compared channels, calculated p-value should be smaller than expected p-value (0.05) so that the results of GLM estimation for those two channels be statistically significant. Figure 48 has shown the calculated beta, t-test and p-values for channel T6-R2 of subject #1 by the GUI.

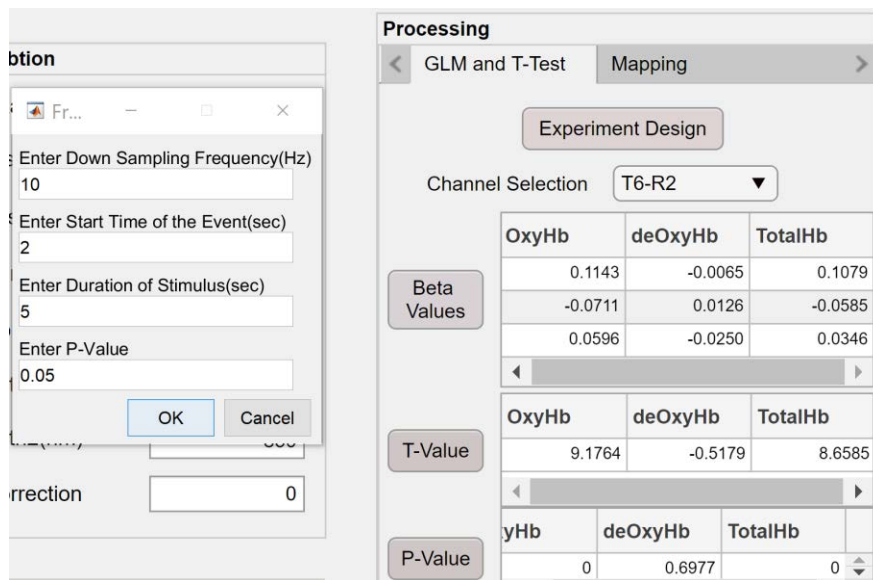


Figure 48. Calculated values after GLM estimation on data collected from subject #1.

As it is shown in the Figure 48, p-values are calculated (Equation 17 & 18) and for each channel (except for HbR in channel T6-R2) null hypothesis has been rejected for HbR, HbR and tHb (Calculated p-value < Expected p-value). Table 7& 8 has also shown the calculated t and p-values based on Equation 16& 17 for 600 samples of each individual channels for all subjects.

TABLE 7.

Statistical results of 8 channels for subjects # 1 &2.

Channel	Statistical Parameter	Subject #1			Subject #2		
		HbO	HbR	tHb	HbO	HbR	tHb
T1-R1	T-value	8.9796	3.6940	12.6736	-3.344	-2.406	-5.705
	P-value	0	1.1e-04	0	0.99	0.99	1
T2-R1	T-value	13.4467	2.2174	15.6641	-3.3114	-3.5336	-6.845
	P-value	0	0.0134	0	0.9995	0.9998	1
T3-R1	T-value	12.0363	15.0087	27.045	-3.275	-4.675	-7.948
	P-value	0	0	0	0.9995	1	1
T4-R1	T-value	7.034	7.5895	14.6235	-3.2818	-4.5024	-7.784
	P-value	1.4e-12	2.5e-14	0	0.9995	1	1
T5-R2	T-value	9.9496	8.9368	18.8864	-3.3237	-3.2636	-6.587
	P-value	0	0	0	0.9995	0.9994	1
T6-R2	T-value	9.1764	-0.5179	8.6585	-3.3263	-3.0929	-6.4192
	P-value	0	0.6977	0	0.9996	0.999	1
T7-R2	T-value	12.9486	4.3909	17.3395	-3.339	-2.583	-5.923
	P-value	0	5.9e-06	0	0.9996	0.9951	1
T8-R2	T-value	4.2254	11.1628	15.3882	-3.3395	-2.727	-6.066
	P-value	1.2e-05	0	0	0.9996	0.9968	1

TABLE 8.

Statistical results of 8 channels for the subjects # 3&4.

Channel	Statistical Parameter	Subject #3			Subject #4		
		HbO	HbR	tHb	HbO	HbR	tHb
T1-R1	T-value	2.1579	-6.7517	-4.5938	5.7371	-13.919	-8.182
	P-value	0.015	1	1	0.0169	0.9996	0.8961
T2-R1	T-value	-1.9159	-1.5534	-3.4693	5.1196	7.3951	12.5147
	P-value	0.9722	0.9398	0.9997	0.0296	0.0032	0
T3-R1	T-value	-1.99	1.9727	-0.0172	4.6353	25.142	29.778
	P-value	0.9766	0.0243	0.5069	0.0432	0	0
T4-R1	T-value	2.1788	-7.4776	-5.2988	5.2698	1.4789	6.7487
	P-value	0.0147	1	1	0.0255	0.2938	0.0063
T5-R2	T-value	-2.078	3.6156	1.5376	5.2763	2.906	8.1823
	P-value	0.9811	0.0002	0.0622	0.0011	0.1422	0.0004
T6-R2	T-value	2.2175	0.9265	3.144	5.0116	11.6679	16.6795
	P-value	0.0134	0.1772	0.0008	0.318	0	0
T7-R2	T-value	2.0038	-1.836	0.1678	5.3257	0.3504	5.6761
	P-value	0.0226	0.9667	0.4334	0.0252	0.4476	0.0184
T8-R2	T-value	1.9324	0.8596	2.792	5.1755	5.4973	10.6728
	P-value	0.0267	0.1951	0.0026	0.0285	0.0218	0

As it has shown in Table 7& 8, for subject #1 only channel T6-R2 (HbR) (Transmitter 6-Receiver 2) the data is not statistically significant and null hypothesis is accepted ($P_{cal} > 0.05$). For subject #2, all calculated p-values are greater than 0.05 so null hypothesis has failed to reject, and similarities among the dataset is high for HbO, HbR and tHb. Conversely, null hypothesis for subjects #3, null hypothesis is rejected for channels: T1-R1 (HbO), T3-R1 (HbR), T4-R1 (HbO), T5-R2 (HbR), T6-R2 (HbO and tHb), T7-R2 (HbO) and T8-R2 (HbO and tHb) and it has resulted in meaningful dataset only for these channels. For subject #4, null hypothesis is accepted for channels: T1-R1 (HbR and tHb), T4-R1 (HbR), T5-R2 (HbR), T6-R2 (HbO) and T7-R2 (HbR). As it has been indicated in Table 7& 8, among 14 channels of all four-subjects that null hypothesis is accepted (meaningless dataset), in 7 cases the dataset is belonged to HbR changes. This interpretation can be also shown using histogram fitting response in Figure 49. Figure 49 demonstrated that calculated p-values for subject #1 are distributed normally rather than other subjects. As previously shown, except channel T6-R2 (HbR), for rest of channels in subject #1, the calculated p-values are smaller than the threshold (0.05). All data points in subject #2 are close together (lower STD).

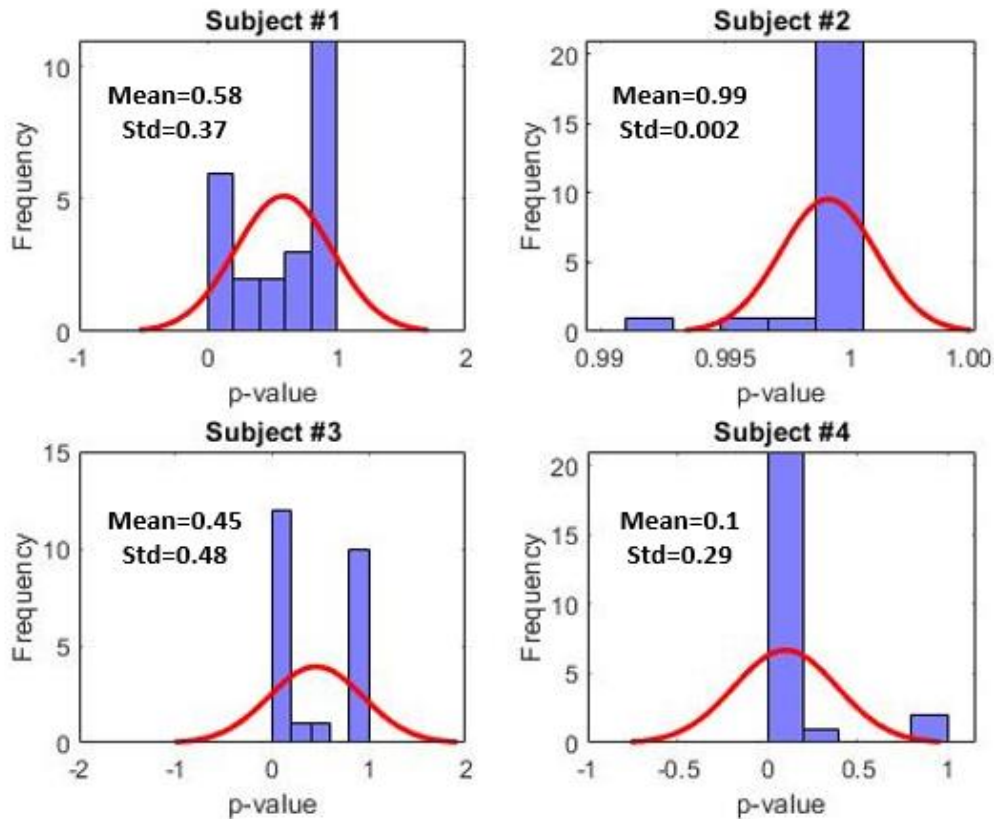


Figure 49. Histogram of p-values for all subjects.

4.3 Evoked Related Potential (ERP)

ERP graph shows how optical density data have distributed in the brain over time. This graph can also show how brain responses to each stimulus. All ERP responses have generated using processing steps discussed in sections 3.5.1 and 3.5.2 (DCT detrending and BPF-4th order with 0.01 and 0.6 Hz cutoff frequencies). Figures 50-53 are shown ERP graphs of all subjects for one trial.

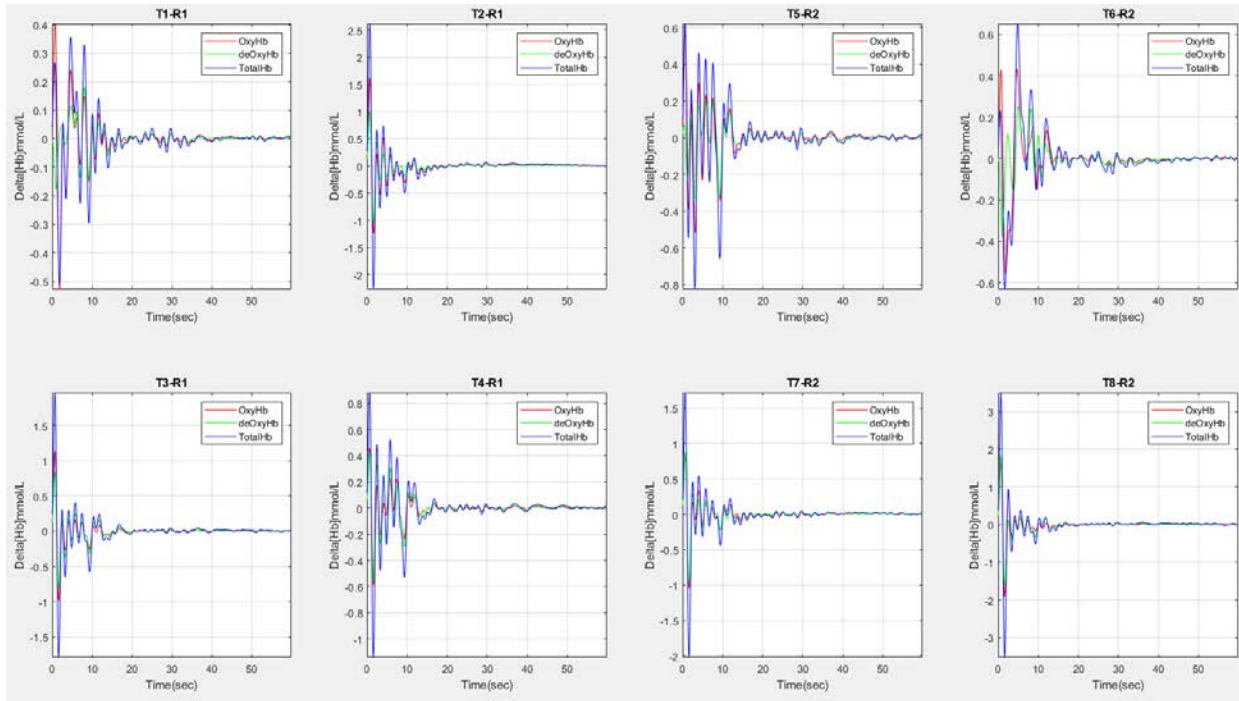


Figure 50. ERP responses of each channel for subject #1.

As it has shown in Figure 50, for subject #1, the transient hemodynamic responses (HbO, HbR and tHb concentration changes) have distributed in the motor cortex area during finger tapping task. The subject's brain has responded actively to motor imaginary task in the area under channels T1-R1, T4-R1 and T5-R2. Other channels have almost shown same concentration changes.

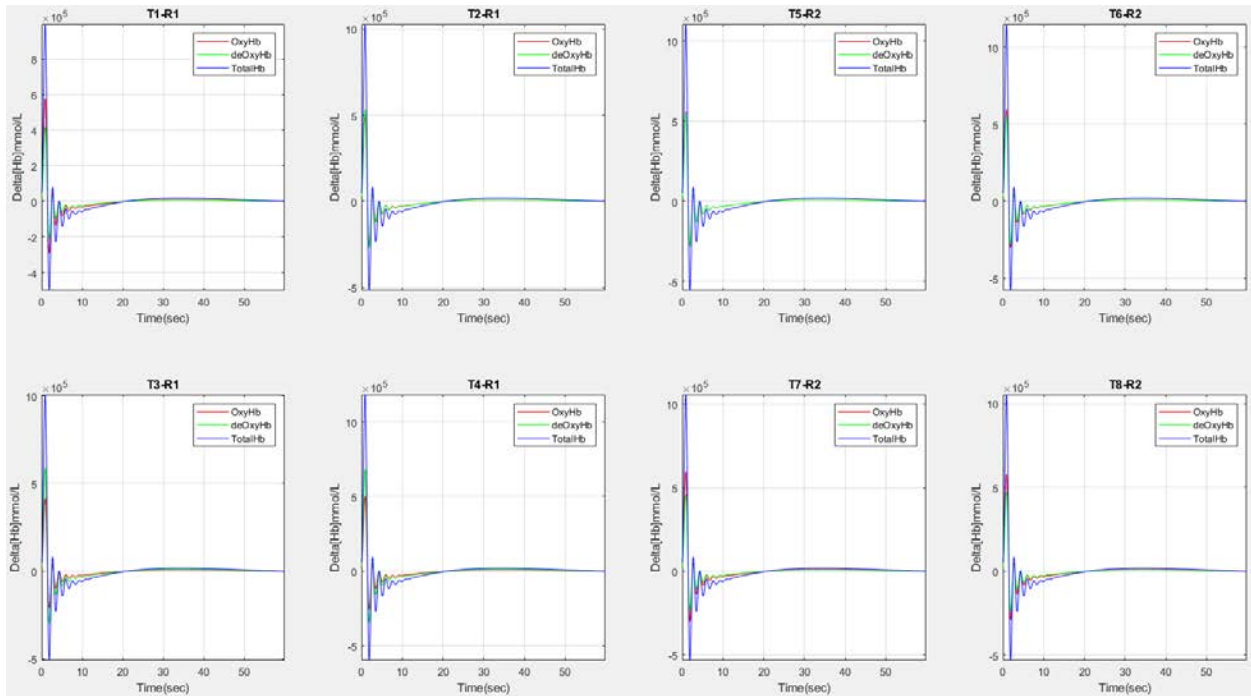


Figure 51. ERP responses of each channel for subject #2.

Figure 51 has shown ERP graph for subject #2. All 8 channels are responding to the stimulus and motor cortex area is less active than subject #1. In this subject, HbO, HbR and tHb indicated the same amplitude and identical ERP graphs have obtained. Figure 52 and 53 have shown ERP responses for subject #3 &4. As it has shown in Figure 52, the concentration changes for none of the channels are in acceptable range and even changes for HbO, HbR and tHb are not synchronous. These results have obtained for subject #4 as well in Figure 53. The SNR values and statistical analysis have already proven that subjects #3 &4 did not provide a good dataset.

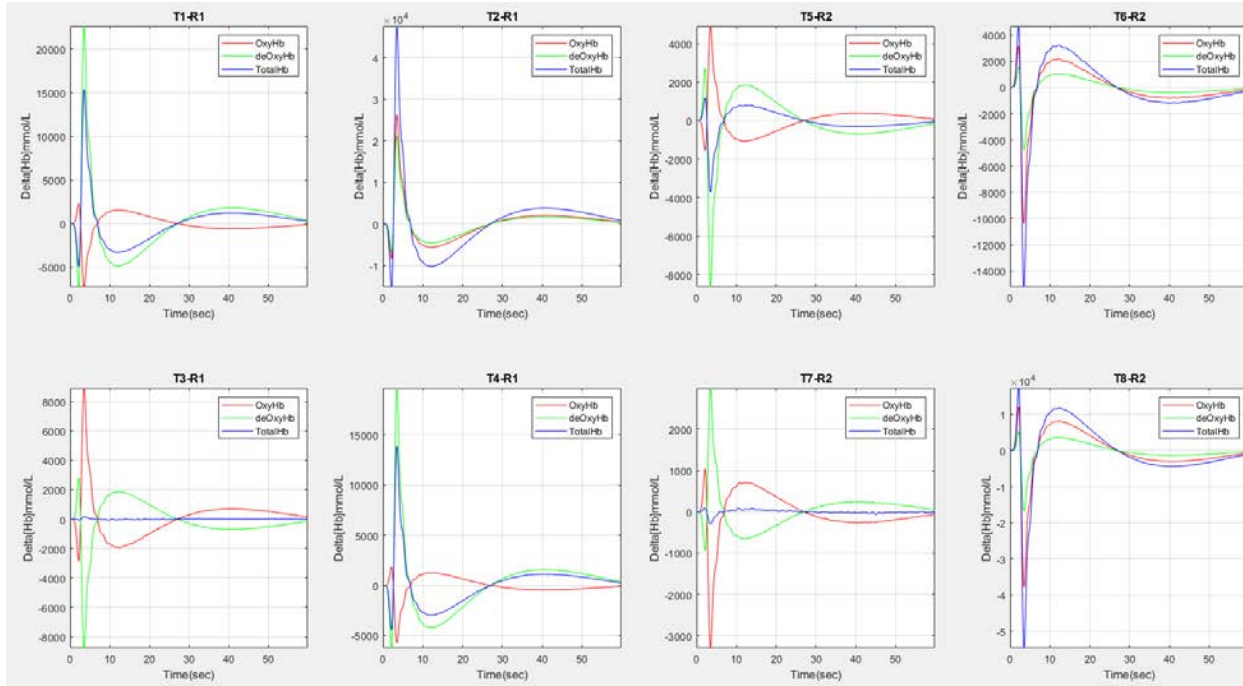


Figure 52. ERP responses of each channel for subject #3.

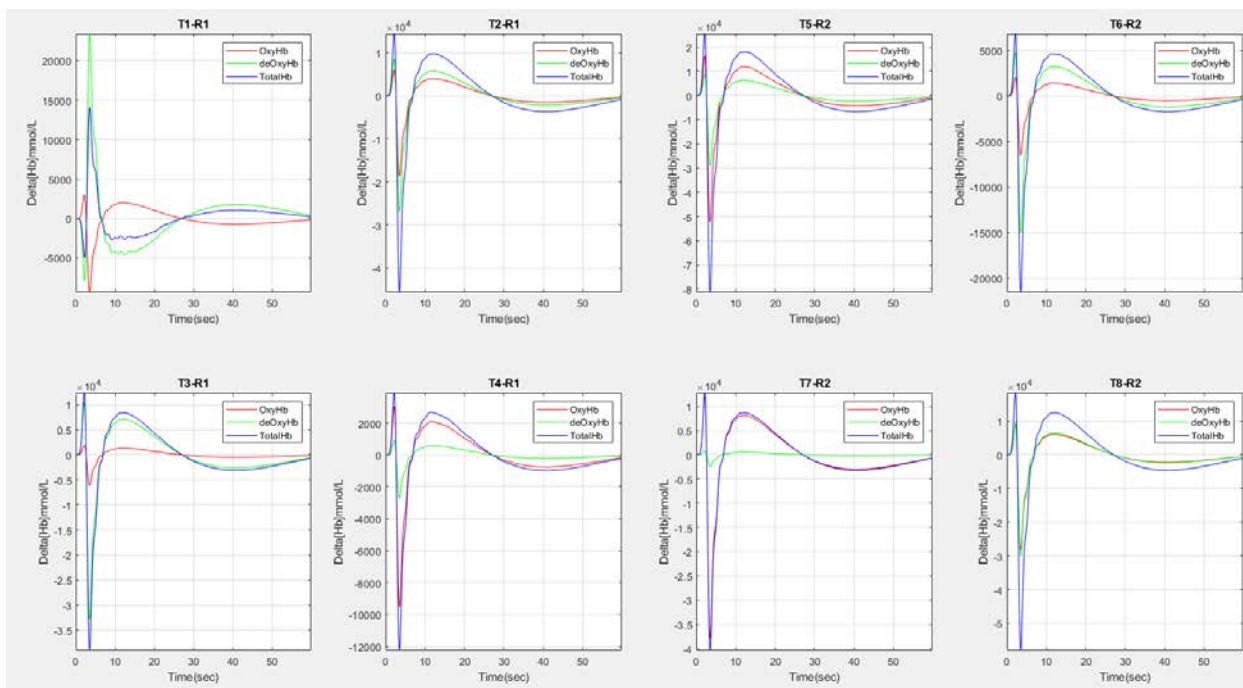


Figure 53. ERP responses of each channel for subject #4.

4.4 Brain Mapping Results

This section provides 2D and 3D brain mapping results for all subjects during 5 sec of motor imaginary task using the GUI for both right and left MI finger tapping. In the previous sections, the data has processed and the channels with meaningless values have been determined. As it has been shown in data analysis section, HbR mapping for half of the cases that we had data similarities has failed to reject null hypothesis so for brain mapping tHb has used. Visualizing can help to better understand how the data of each subject looks like per channels. Figures 54-57 have shown 2D brain mapping results for each subject.

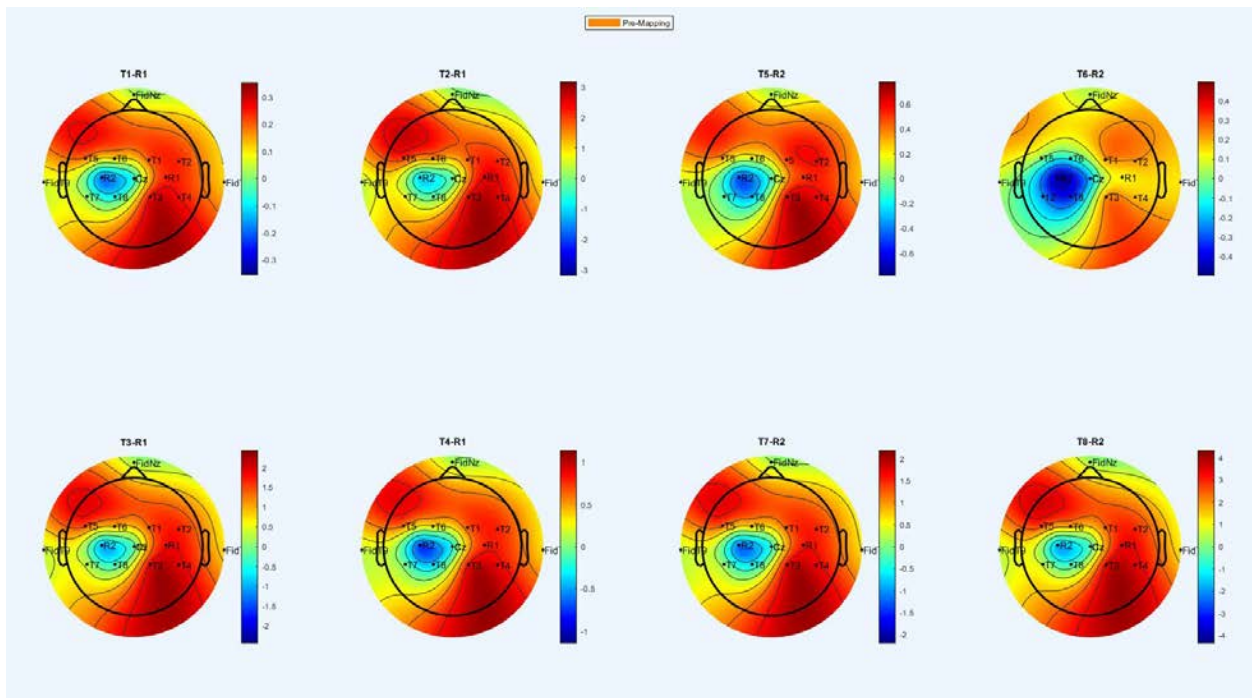


Figure 54. 2D brain mapping results per channel for subject #1.

tHb levels can be seen for each channel in Figure 54. Channel T6-R2, left hand finger tapping, has shown less activity rather than other 7 channels due to lack of meaningful data in this channel for HbR as it has already shown in the data analysis section.

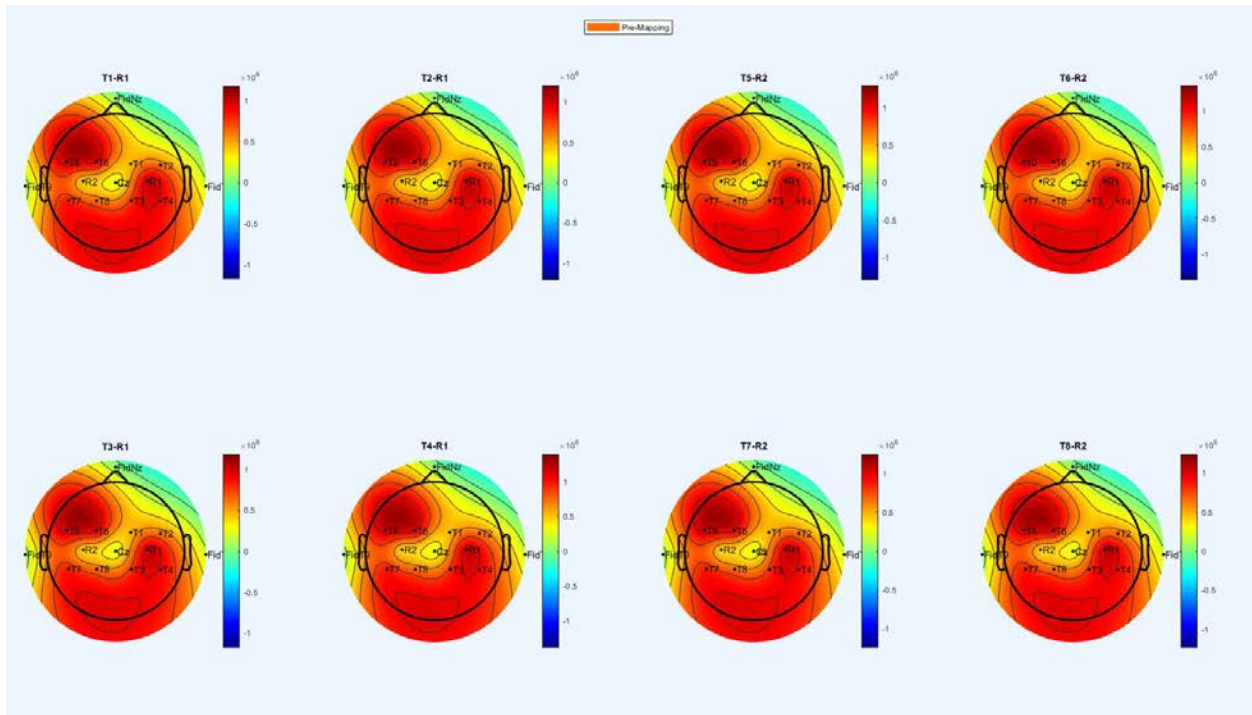


Figure 55. 2D brain mapping results per channel for subject #2.

2D Mapping results for subject #2 (Figure 55) has shown that tHb levels in each channel is similar and the brain has responded to the stimulus actively in all channels. On the other hand, subjects #3 &4, have not shown a good brain mapping as most of their data were contained noise (Section 4.1) and therefore their values were statistically meaningless (Section 4.2). For these two subjects, only channels located on the left side of MC for subject #3 (right hand finger tapping), and channel T1-R1 for subject# 4 (right hand finger tapping) have shown activity changes within the brain.

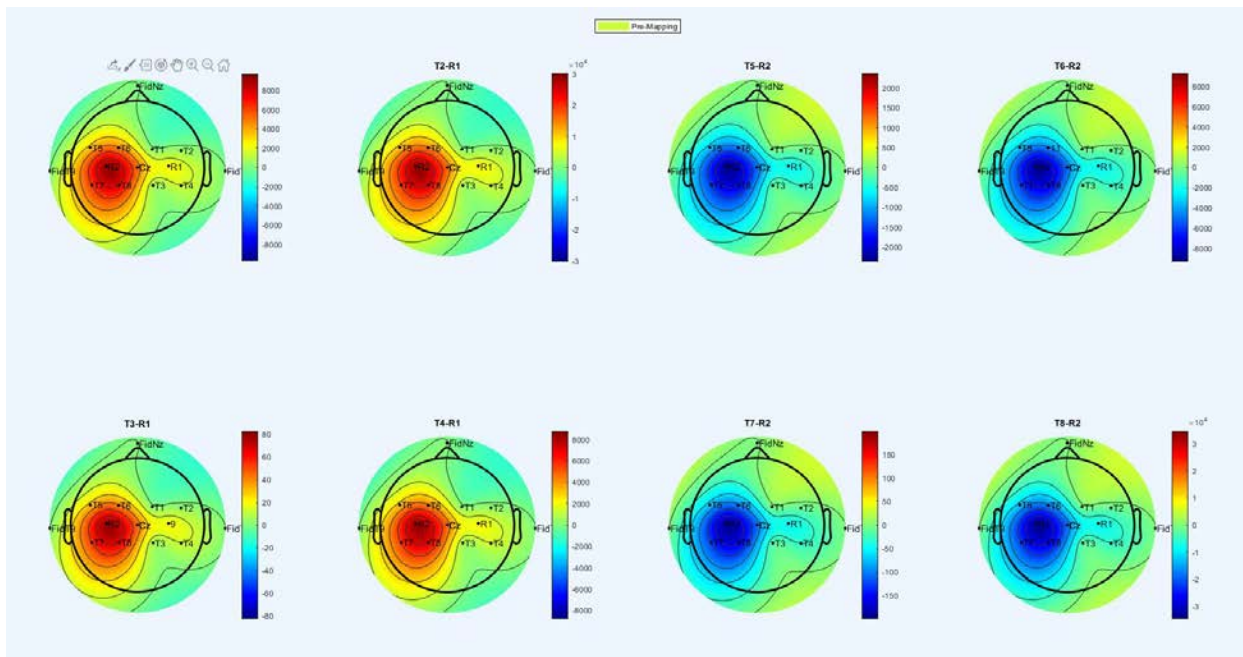


Figure 56. 2D brain mapping results per channel for subject #3.

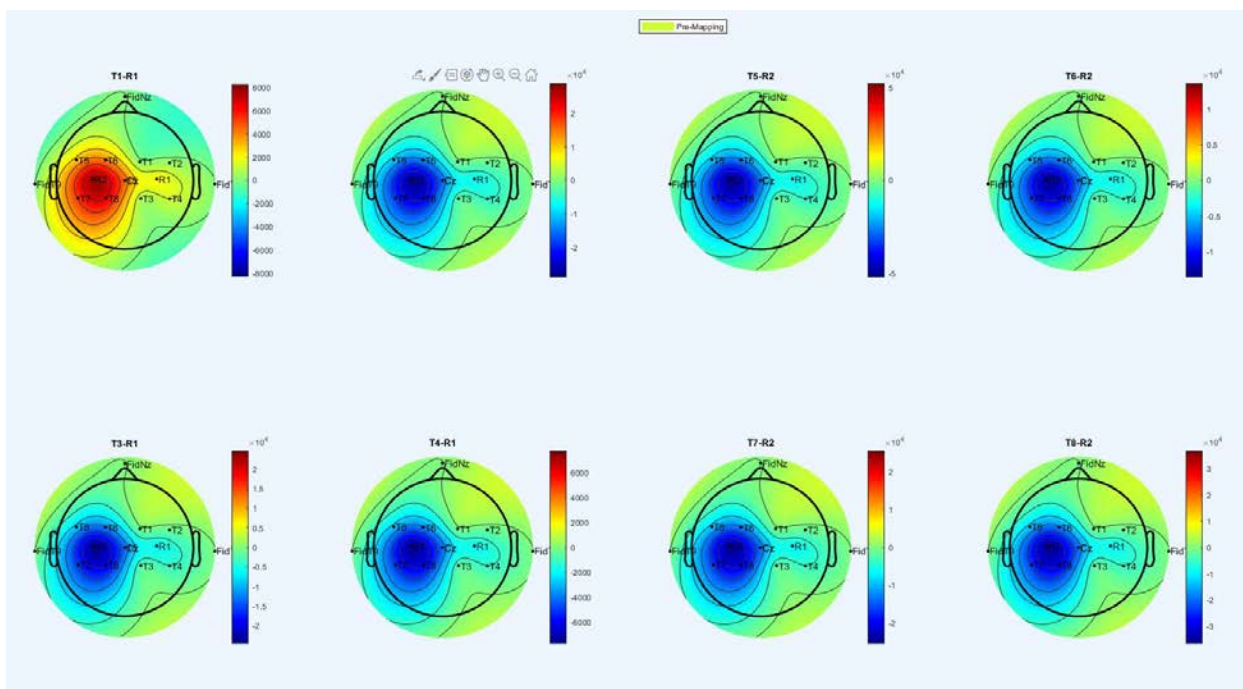


Figure 57. 2D brain mapping results per channel for subject #4.

Figure 58 and 59 have shown the results of 3D brain mapping for subject's #1- 4. Subject #1 (Figure 58-a) has shown a less tHb changes in the region associated to channel T6-R2 (Primary motor cortex). Similarly, subject #2 showed a better activation map in his motor cortex area (Figure 58-b). As it has been expected from 2D mapping, subjects #3& 4 are not shown a good 3D brain mapping as well (Figures 60 &61). These results can be explained as the data quality for both subjects #3& 4 are not appropriate and most of the data contained noise and meaningless values (Table 8).

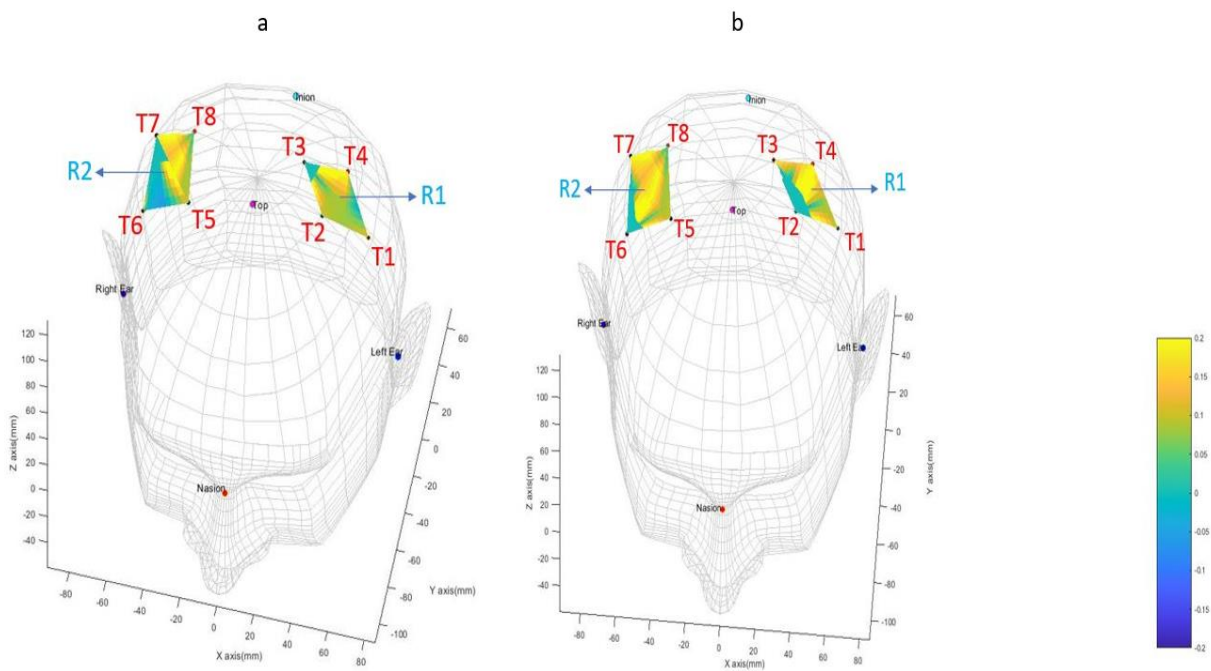


Figure 58. 3D brain mapping for Subject #1 (a) and Subject #2 (b).

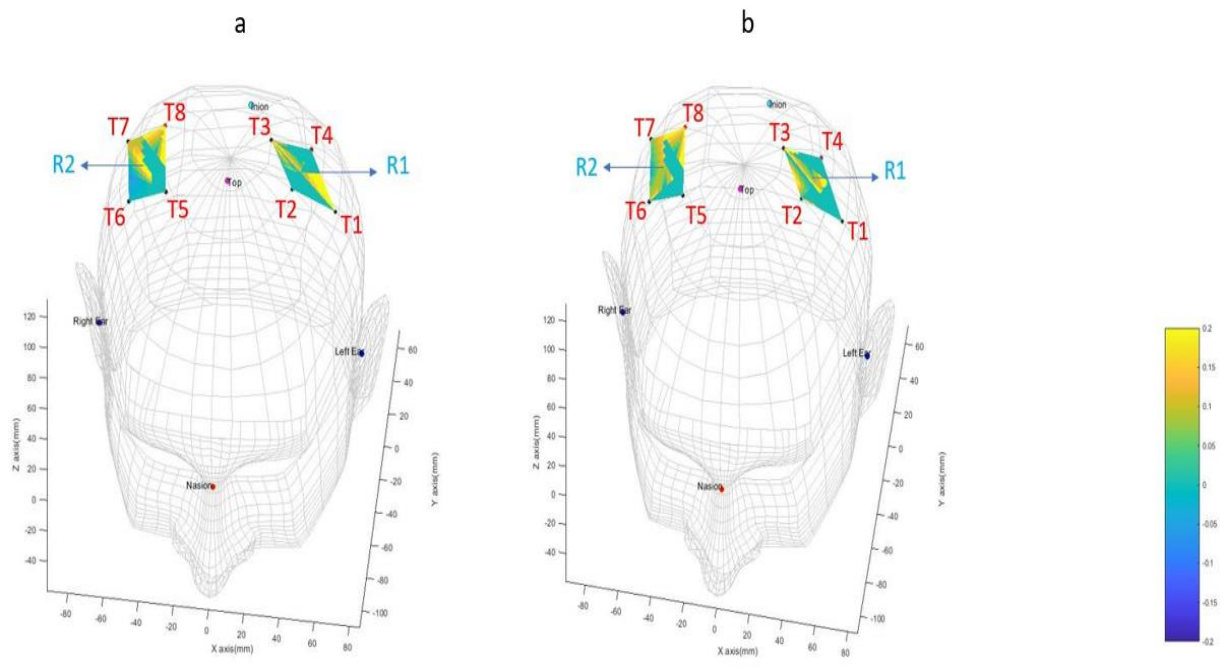


Figure 59. 3D brain mapping for Subject #3 (a) and Subject #4 (b).

CHAPTER 5

DISCUSSION AND FUTURE WORK

Inspired by the previous works done by researchers in creating automatic analysis and processing toolbox for fNIRS studies (Section 2.2), this project aimed at introducing an open-source, offline/online MATLAB-based signal processing and data analysis package by taking advantages of available toolboxes and focusing on enhancing signal quality with DCT detrending. The goal was to design an fNIRS analysis package for 8-channels g.tec/ARTINIS systems such that the user has more freedom for signal detrending (Linear, DCT and DWT detrend) and signal processing (BPF with 0.01- 0.6 Hz cutoff frequency, Moving Average with 10- 20 sec frame size and S-G with 101 sec frame size and order 4). However, this project has designed a first prototype fNIRS system based on square optode configuration regarding to the ARTINIS system as a gold standard reference design. For this application, to augment the performance of the designed GUI, the dataset from three different subjects (Subjects #2,3 and 4) have been collected using ARTINIS system and the dataset from one of the subjects (Subject #1) obtained from the designed prototype. As it has been shown in section 4.1, the signal quality obtained from subjects #1 &2 as 6.99 and 4.8 dB, respectively, were greater than the predefined threshold of 3 dB. For motor imaginary task (5 sec of finger tapping) and each trial (9 sec) the GLM estimator has been designed for each subject's dataset. Data analysis results have shown that subjects #3 &4 did not provide a meaningful dataset in 13 channels since the calculated p-value for those subjects were greater than the expected p-value(=0.05) and null hypothesis has failed to be rejected. Also, for subject #2, values of each channel's dataset are similar together and null hypothesis is then accepted. Brain mapping and ERP graphs have further proven this fact. The data analysis results have also shown that HbR changes is not a good representative tool for mapping purposes. Brain mapping results

have shown that between subjects #1&2, only channel T6-R2 on the right side of subject's one primary motor cortex area, has not indicated an acceptable tHb concentration changes in the underneath brain tissues. As we have already expected from SNR values obtained in time and frequency domain analysis (Section 4.1.1& 4.1.2) and also data analysis and statistical results have depicted that (Section 4.2& Table 8), subjects #3& 4 have not produced a good brain mapping and activation graphs in the right side of the MC and left hand finger tapping.

Future work of this project should focus on collecting more data with more participants and testing the GUI with more paradigms like Stroop task. It is possible that poor GLM estimation and statistical results is due to the lack of data, so motor imaginary experiments should be performed on multiple days. Besides brain mapping studies, this project can be developed for decoding and classification purposes as it has been able to process individual channels furthermore user can identify which channels are more active for feature extraction. Moreover, for more complicated tasks, it will be interesting to train healthy participants and stroke patients either for brain mapping studies or classification, encoding or/and a robust controller designing using the GUI and look for behavioral improvements in the graphs provided by the fNIRS analysis package. In the future, participants could perform a reaction task, receive neurofeedback, and then in a post-test check if participants are faster at the reaction task. This will reveal more about behavioral performance and neuroplasticity. While the results from this project were overall unconvincing, neural therapy is the future of neurological rehabilitation and more research is needed to achieve this goal. For the future, the designed GUI can be equipped with baseline analyzer methods like PCA, ICA or first or second- derivative functions.

CHAPTER 6

CONCLUSION

In this thesis, an fNIRS analysis package for signal processing and data analysis of fNIRS data with four subject's datasets during motor imagery tasks have been introduced. The choice of the most dominant software/toolbox for offline/online analyzing of fNIRS data for brain mapping studies has been always challenging since it should be able not only to provide an user friendly and open-source signal and data analysis all in one package, but also it should successfully distinguish functional regions of the brain during a desired task/experiment. In this project, due to manually adjust optode positions based on 10-20 standards adapted from EEG cap, the results of 2D and 3D mapping may not represent the actual brain region underneath each channel. For more accurate applications when the goal is finding the exact location of the brain where the signal is originated, other digitizing methods such as 3D digitizer is recommended to use.

REFERENCES

REFERENCES

- [1] Jobsis, Frans F. "Noninvasive, infrared monitoring of cerebral and myocardial oxygen sufficiency and circulatory parameters." *Science* 198.4323 (1977): 1264-1267.
- [2] Villringer, Arno, and U. Dirnagl. "Coupling of brain activity and cerebral blood flow: basis of functional neuroimaging." *Cerebrovascular and brain metabolism reviews* 7.3 (1995): 240-276.
- [3] C. Van Hoof and R. Puers, "Biopotential readout circuits for portable acquisition systems", Springer, 2009.
- [4] Kamran, Muhammad Ahmad, et al. "Differential path-length factor's effect on the characterization of brain's hemodynamic response function: a functional near-infrared study." *Frontiers in neuro informatics* 12 (2018): 37.
- [5] P. Agnihotri, R. Fazel-Rezai, and N. Kaabouch, "Comparative analysis of various brain imaging techniques." in *Engineering in Medicine and Biology Society (EMBC), 2010 Annual International Conference of the IEEE*, 2010, pp. 3029-3032.
- [6] Irani, Farzin, et al. "Functional near infrared spectroscopy (FNIRS): an emerging neuroimaging technology with important applications for the study of brain disorders." *The Clinical Neuropsychologist* 21.1 (2007): 9-37.
- [7] Bunge, Silvia A., and Itamar Kahn. "Cognition: An overview of neuroimaging techniques." (2009): 1063-1067.
- [8] Khan, Rayyan Azam, et al. "Cortical Tasks-Based Optimal Filter Selection: An FNIRS Study." *Journal of Healthcare Engineering* 2020 (2020).
- [9] Yuan, Zhen. "Spatiotemporal and time-frequency analysis of functional near infrared spectroscopy brain signals using independent component analysis." *Journal of biomedical optics* 18.10 (2013): 106011.
- [10] Pfeifer, Mischa D., Felix Scholkmann, and Rob Labruyère. "Signal processing in functional near-infrared spectroscopy (FNIRS): methodological differences lead to different statistical results." *Frontiers in human neuroscience* 11 (2018): 641.
- [11] Ye, Jong Chul, et al. "NIRS-SPM: statistical parametric mapping for near-infrared spectroscopy." *Neuroimage* 44.2 (2009): 428-447.
- [12] Abdelnour, A. Farras, and Theodore Huppert. "Real-time imaging of human brain function by near-infrared spectroscopy using an adaptive general linear model." *Neuroimage* 46.1 (2009): 133-143.
- [13] Hu, Xiao-Su, et al. "Kalman estimator-and general linear model-based on-line brain activation mapping by near-infrared spectroscopy." *Biomedical engineering online* 9.1 (2010): 82.

- [14] Kamran, Muhammad Ahmad, et al. "Differential path-length factor's effect on the characterization of brain's hemodynamic response function: a functional near-infrared study." *Frontiers in neuroinformatics* 12 (2018): 37.
- [15] Maikala, Rammohan V. "Modified Beer's Law—historical perspectives and relevance in near-infrared monitoring of optical properties of human tissue." *International Journal of Industrial Ergonomics* 40.2 (2010): 125-134. [15]
- [16] Yin, Xuxian, et al. "A hybrid BCI based on EEG and FNIRS signals improves the performance of decoding motor imagery of both force and speed of hand clenching." *Journal of neural engineering* 12.3 (2015): 036004.
- [17] Glotzbach, Evelyn, et al. "Prefrontal brain activation during emotional processing: a functional near infrared spectroscopy study (FNIRS)." *The open neuroimaging journal* 5 (2011): 33.
- [18] Zhang, Y., J. Sun, and P. Rolfe. "Reduction of global interference in functional multidistance near-infrared spectroscopy using empirical mode decomposition and recursive least squares: A Monte Carlo study." *Journal of the European Optical Society-Rapid publications* 6 (2011).
- [19] Zhang, Y., J. W. Sun, and P. Rolfe. "RLS adaptive filtering for physiological interference reduction in NIRS brain activity measurement: A Monte Carlo study." *Physiological measurement* 33.6 (2012): 925.
- [20] Baker, Joseph M., et al. "Sex differences in neural and behavioral signatures of cooperation revealed by FNIRS hyperscanning." *Scientific reports* 6 (2016): 26492.
- [21] Wijekumar, Sobanawartiny, et al. "Validating an image-based FNIRS approach with fMRI and a working memory task." *NeuroImage* 147 (2017): 204-218.
- [22] Pinti, Paola, et al. "A novel GLM-based method for the Automatic IDentification of functional Events (AIDE) in FNIRS data recorded in naturalistic environments." *NeuroImage* 155 (2017): 291-304.
- [23] Morais, Guilherme Augusto Zimeo, Joana Bisol Balardin, and João Ricardo Sato. "FNIRS Optodes' Location Decider (fOLD): A toolbox for probe arrangement guided by brain regions-of-interest." *Scientific reports* 8.1 (2018): 3341.
- [24] Yuan, Zhen, and Xiaohong Lin. "Mapping of the brain activation associated with deception using fused EEG and FNIRS." *Neural Imaging and Sensing 2019*. Vol. 10865. International Society for Optics and Photonics, 2019.
- [25] Shuvra, Lubna Tabassum, et al. "Identification of Human Pain Perception using FNIRS." *2019 International Conference on Robotics, Electrical and Signal Processing Techniques (ICREST)*. IEEE, 2019.
- [26] Urushidani, Naoki, et al. "Low-frequency rTMS and intensive occupational therapy improve upper limb motor function and cortical reorganization assessed by functional near-infrared spectroscopy in a subacute stroke patient." *Case reports in neurology* 10.2 (2018): 223-231.

- [27] Santosa, Hendrik, et al. "Investigation of the sensitivity-specificity of canonical-and deconvolution-based linear models in evoked functional near-infrared spectroscopy." *Neurophotonics* 6.2 (2019): 025009.
- [28] Mousa Moradi, Adam Ruest, Jaydip Desai. "Design and development of a functional near infrared spectroscopy-based brain mapping graphical user interface". Accepted for *Biomedical Sciences Instrumentation Journal*, Apr 2020.
- [29] Theodore Huppert, David A. Boas, "HomER - Hemodynamic Evoked Response NIRS data analysis GUI", Photon Migration Imaging Lab Massachusetts General Hospital/CNY Charlestown, MA 02139, 2005.
- [30] Huppert, Theodore J., et al. "HomER: a review of time-series analysis methods for near-infrared spectroscopy of the brain." *Applied optics* 48.10 (2009): D280-D298.
- [31] <https://github.com/BUNPC/Homer3>.
- [32] Xu Y., Graber H., Barbour R. "nirsLAB user manual", 2016 Available online at: https://www.nitrc.org/frs/shownotes.php?release_id=2663.
- [33] Tadel, François, et al. "Brainstorm: a user-friendly application for MEG/EEG analysis." *Computational intelligence and neuroscience* 2011 (2011).
- [34] Machado, A., et al. "Optimal positioning of optodes on the scalp for personalized functional near-infrared spectroscopy investigations." *Journal of neuroscience methods* 309 (2018): 91-108.
- [35] <https://github.com/Nirstorm/nirstorm>.
- [36] Ferrari M, Quaresima V. "A brief review on the history of human functional near-infrared spectroscopy (FNIRS) development and fields of application." *NeuroImage* 63 (2012) 921–935.
- [37] Cope, Mark, and David T. Delpy. "System for long-term measurement of cerebral blood and tissue oxygenation on newborn infants by near infra-red transillumination." *Medical and Biological Engineering and Computing* 26.3 (1988): 289-294.
- [38] Quaresima, Valentina, and Marco Ferrari. "Functional near-infrared spectroscopy (FNIRS) for assessing cerebral cortex function during human behavior in natural/social situations: a concise review." *Organizational Research Methods* 22.1 (2019): 46-68.
- [39] Kamran, Muhammad A., Malik M. Naeem Mannan, and Myung Yung Jeong. "Cortical signal analysis and advances in functional near-infrared spectroscopy signal: a review." *Frontiers in human neuroscience* 10 (2016): 261.
- [40] Bunce, Scott C., et al. "Functional near-infrared spectroscopy." *IEEE engineering in medicine and biology magazine* 25.4 (2006): 54-62.

- [41] E. Okada, M. Firbank, M. Schweiger, S. Arridge, M. Cope, and D. Delpy, "Theoretical and experimental investigation of near-infrared light propagation in a model of the adult head," *Applie*, vol. 36, Issue 1, pp. 21–31, 1997.
- [42] F. Scholkmann, S. Kleiser, A. J. Metz, R. Zimmermann, J. M. Pavia, U. Wolf, and M. Wolf, "A review on continuous wave functional near-infrared spectroscopy and imaging instrumentation and methodology," *NeuroImage*, no. 0, pp. –, 2013.
- [43] Venclove, Sigita, Algis Daktariunas, and Osvaldas Ruksenas. "Functional near-infrared spectroscopy: a continuous wave type-based system for human frontal lobe studies." *EXCLI journal* 14 (2015): 1145.
- [44] Davies, David James, et al. "Frequency-Domain vs Continuous-Wave Near-Infrared Spectroscopy devices." (2016).
- [45] Abdalmalak, Androu, et al. "Can time-resolved NIRS provide the sensitivity to detect brain activity during motor imagery consistently?" *Biomedical optics express* 8.4 (2017): 2162-2172.
- [46] M. W. W. Wolf and V. Toronov, "Different time evolution of oxyhemoglobin and de-oxyhemoglobin concentration changes in visual and motor cortices during functional stimulation: a near-infrared spectroscopy study." *Neuroimage*, vol. 16, pp. 704–712, 2002.
- [47] S. Coyle, T. Ward, and C. Markham, "Physiological noise in near-infrared spectroscopy: implications for optical brain computer interfacing," in *Engineering in Medicine and Biology Society, 2004. IEMBS '04. 26th Annual International Conference of the IEEE*, vol. 2, pp. 4540-4543, 2004.
- [48] Fallgatter, A. J., D. Brandeis, and W. K. Strik. "A robust assessment of the NoGo-anteriorisation of P300 microstates in a cued Continuous Performance Test." *Brain topography* 9.4 (1997): 295-302.
- [49] Herrmann, M. J., A-C. Ehlis, and A. J. Fallgatter. "Frontal activation during a verbal-fluency task as measured by near-infrared spectroscopy." *Brain Research Bulletin* 61.1 (2003): 51-56.
- [50] Kuboyama, Naomi, et al. "The effect of maximal finger tapping on cerebral activation." *Journal of physiological anthropology and applied human science* 23.4 (2004): 105-110.
- [51] Kashou, Nasser H., et al. "Hand-grasping and finger tapping induced similar functional near-infrared spectroscopy cortical responses." *Neurophotonics* 3.2 (2016): 025006.
- [52] Yanagisawa, Hiroki, et al. "Acute moderate exercise elicits increased dorsolateral prefrontal activation and improves cognitive performance with Stroop test." *Neuroimage* 50.4 (2010): 1702-1710.
- [53] H.-C. Leung, P. Skudlarski, J. C. Gatenby, B. S. Peterson, and J. C. Gore. An event-related functional MRI study of the Stroop color word interference task. *Cerebral cortex*, 10(6):552–560, 2000.
- [54] Wijekumar, Sobanawartiny, et al. "Localization of hemodynamic responses to simple visual stimulation: an FNIRS study." *Investigative ophthalmology & visual science* 53.4 (2012): 2266-2273.

- [55] Huppert, Theodore J., et al. "Functional imaging of cognition in an old-old population: A case for portable functional near-infrared spectroscopy." *PloS one* 12.10 (2017).
- [56] Salehuddin, Muhammad, and Farida I. Muchtadi. "Prototype design of low cost four channels digital electroencephalograph for sleep monitoring." 2011 2nd International Conference on Instrumentation Control and Automation. IEEE, 2011.
- [57] Amaro Jr, Edson, and Gareth J. Barker. "Study design in fMRI: basic principles." *Brain and cognition* 60.3 (2006): 220-232.
- [58] Better efficiency will be achieved when the rest timing is equal to average stimulation time of the task-related conditions.
- [59] Nishiyori, Ryota. "FNIRS: An emergent method to document functional cortical activity during infant movements." *Frontiers in psychology* 7 (2016): 533.\
- [60] Chevalier, Nicolas, et al. "Differentiation in prefrontal cortex recruitment during childhood: Evidence from cognitive control demands and social contexts." *Developmental cognitive neuroscience* (2019): 100629.
- [61] Gao, Lei, et al. "Effects of assuming constant optical scattering on haemoglobin concentration measurements using NIRS during a Valsalva Manoeuvre." *Oxygen Transport to Tissue XXXII*. Springer, Boston, MA, 2011. 15-20.
- [62] Balardin, Joana B., et al. "Imaging brain function with functional near-infrared spectroscopy in unconstrained environments." *Frontiers in human neuroscience* 11 (2017): 258.
- [63] Chen, Michelle, et al. "Spatial Co-registration of Functional Near-Infrared Spectroscopy to Brain MRI." *Journal of Neuroimaging* 27.5 (2017): 453-460.
- [64] Chuang, Chun-Hsiang, et al. "Brain electrodynamic and hemodynamic signatures against fatigue during driving." *Frontiers in neuroscience* 12 (2018): 181.
- [65] Durantin, Gautier, et al. "Processing functional near infrared spectroscopy signal with a Kalman filter to assess working memory during simulated flight." *Frontiers in human neuroscience* 9 (2016): 707.
- [66] Rongqing Hui, "Introduction to Fiber-Optic Communications", Academic Press; 1 edition, September 15, 2019.
- [67] A. Siegel, J. Marota, and D. Boas, "Design and evaluation of a continuous-wave diffuse optical tomography system," *Optics Express*, vol. 4, pp. 287-298, 1999.
- [68] Donald L. Wise, "Bioinstrumentation and Biosensors ", CRC Press; 1 edition, Pages 522-524, January 31, 1991.
- [69] Tony J.Rouphael, "RF and Digital Signal Processing for Software-Defined Radio ", ScienceDirect, Pages 87-122, 2009.

- [70] Fekete, Tomer, et al. "The NIRS analysis package: noise reduction and statistical inference." *PloS one* 6.9 (2011).
- [71] Brigadoi, Sabrina, et al. "Motion artifacts in functional near-infrared spectroscopy: a comparison of motion correction techniques applied to real cognitive data." *Neuroimage* 85 (2014): 181-191.
- [72] Hue Dang, "Processing and analyzing functional near-infrared spectroscopy data", Master thesis, Radboud University, Page 9, September 2016.
- [73] Zhang, Yiheng, et al. "Eigenvector-based spatial filtering for reduction of physiological interference in diffuse optical imaging." *Journal of biomedical optics* 10.1 (2005): 011014.
- [74] Wilcox, Teresa, et al. "Using near-infrared spectroscopy to assess neural activation during object processing in infants." *Journal of biomedical optics* 10.1 (2005): 011010.
- [75] Cui, Xu, Signe Bray, and Allan L. Reiss. "Functional near infrared spectroscopy (NIRS) signal improvement based on negative correlation between oxygenated and deoxygenated hemoglobin dynamics." *Neuroimage* 49.4 (2010): 3039-3046.
- [76] Scholkmann, Felix, et al. "How to detect and reduce movement artifacts in near-infrared imaging using moving standard deviation and spline interpolation." *Physiological measurement* 31.5 (2010): 649.
- [77] Izzetoglu, Meltem, et al. "Motion artifact cancellation in NIR spectroscopy using discrete Kalman filtering." *Biomedical engineering online* 9.1 (2010): 16.
- [78] Molavi, Behnam, and Guy A. Dumont. "Wavelet-based motion artifact removal for functional near-infrared spectroscopy." *Physiological measurement* 33.2 (2012): 259.
- [79] Birvinskas, Darius, et al. "EEG dataset reduction and feature extraction using discrete cosine transform." 2012 Sixth UKSim/AMSS European Symposium on Computer Modeling and Simulation. IEEE, 2012.
- [80] Keles, Hasan Onur, Randall L. Barbour, and Ahmet Omurtag. "Hemodynamic correlates of spontaneous neural activity measured by human whole-head resting state EEG+ FNIRS." *Neuroimage* 138 (2016): 76-87.
- [81] Yücel, Meryem A., et al. "Reducing motion artifacts for long-term clinical NIRS monitoring using collodion-fixed prism-based optical fibers." *Neuroimage* 85 (2014): 192-201.
- [82] Huppert, Theodore J. "Commentary on the statistical properties of noise and its implication on general linear models in functional near-infrared spectroscopy." *Neurophotonics* 3.1 (2016): 010401.
- [83] Brigadoi, Sabrina, and Robert J. Cooper. "How short is short? Optimum source–detector distance for short-separation channels in functional near-infrared spectroscopy." *Neurophotonics* 2.2 (2015): 025005.

- [84] Scarpa, Fabio, et al. "A reference-channel based methodology to improve estimation of event-related hemodynamic response from FNIRS measurements." *Neuroimage* 72 (2013): 106-119.
- [85] Jahani, Sahar, et al. "Motion artifact detection and correction in functional near-infrared spectroscopy: a new hybrid method based on spline interpolation method and Savitzky–Golay filtering." *Neurophotonics* 5.1 (2018): 015003.
- [86] Rao, K. Ramamohan, and Ping Yip. *Discrete cosine transform: algorithms, advantages, applications*. Academic press, 2014.
- [87] Baleanu, Dumitru, ed. *Wavelet Transforms and Their Recent Applications in Biology and Geoscience*. BoD–Books on Demand, 2012.
- [88] Penny, W., S. Kiebel, and K. Friston. "Variational bayes." *Statistical parametric mapping: The analysis of functional brain images* (2006).

APPENDIX

OPEN SOURCE CODE FOR fNIRS SIGNAL PROCESSING

```
%Step1. Import the raw data

RawData=load ('sample_dataset.mat');

SampleData=RawData';    %Transpose the dataset to get channel as column

Fs = 10;    % SpectraTech sampling rate in ARTINIS device (OXYSOFT 2, 5, 10, 25, 50 Hz)

Ts = 1/Fs;

[m,n]= size(SampleData);

final = (m -1)*Ts;

%floor(final);    % if frequency is decimal to make it integer value

t= 0:Ts:final;    % lastTime

t= transpose(t);    % To match the time with nirs data, make it transposed

%Step2.Linear Detrend Detection to eliminate DC offset (Optional: %DCT)

a= detrend(SampleData);

%a= dct(SampleData);

%Step3. Do CAR (Common Average Reference)

%1) Take the total average of 'a'

m= mean(a(:));

% 2) Do subtraction (sample data(a) - total average(m))

new = zeros(size(a)); %Modified(05.19)

new(:) = m;

car= a-m;

%Step4. Do band-pass filtering (LPF 0.6Hz/ HPF 0.01Hz)
```

```

n= 4;      % Define the filter order (the bigger order, the better performance) Trade-off between
           % performance vs cost.

Wn = [0.01 0.6];    % 0.01~0.6 Hz (band-pass filter)

Fn = Fs/2;          % Nyquist frequency

ftype ='bandpass';

[b,a] = butter(n, Wn/Fn, ftype);

y= filter(b,a,car);

%Done Step1~4 :finished Preprocessing

subplot(2,1,1);      % rawdata? detrend+CAR+BPF

plot(t, SampleData);axis tight

xlabel('Time(sec)');

ylabel('delta[Hb]');

title('Original fNIRS Data');

legend('oxy','deoxy','total');

grid on;

subplot(2,1,2);

%HPF results(ROI=sensory motor cortex)

hbo_bp= y(:,1:2:16);

hbr_bp= y(:,2:2:16);

hbt_bp= hbo_bp+hbr_bp;

thb=hbt_bp;

plot(t,hbo_bp,'r');axis tight;

```

```
plot(t,hbr_bp,'b');axis tight;  
plot(t,hbt_bp,'g');axis tight;  
%legend('OxyHb','deOxyHb','TotalHb');  
title('The change of hemoglobin using BPF');  
xlabel('Time(sec)');  
ylabel('change of Hemoglobin(delta[Hb])');  
grid on
```